Monolayer Hexagonal Boron Nitride: an ultra-thin insulator

DISSERTATION
zur Erlangung des Grades eines Doktors der Naturwissenschaften

vorgelegt von
M. Sc. Jiaqi Cai

eingereicht bei der Naturwissenschaftlich-Technischen Fakultät
der Universität Siegen
Siegen 2021

Betreuer und erster Gutachter
Prof. Dr. Carsten Busse
Universität Siegen

Zweiter Gutachter
Prof. Dr. Moritz Sokolowski
Rheinische Friedrich-Wilhelms-Universität Bonn

Tag der mündlichen Prüfung
May 2021

To Ziwen
献给子文

Contents

Chapter 1

Introduction

Since the discovery of graphene [1], the family of 2d-materials (2DM) has prospered. In this study, I focus on monolayer hexagonal boron nitride (hBN), the lesser known cousin of graphene. Despite the similar structure, hBN and graphene have very distinctive electronic properties. Similar to the parent bulk compound, hBN is a large band gap insulator.

Before presenting the research results, Chap. 2 and Chap. 3 present some necessary background information. Chap. 2 introduces the important information from the reported studies of hBN. The characterization methods involved in this study, low energy electron diffraction (LEED), scanning tunneling microscope (STM), X-ray photo-emission spectroscopy (XPS), X-ray standing wave technique (XSW), and the experimental setups involved in the study are briefly introduced in Chap. 3. Starting from Chap. 4, I present my study on the epitaxial systems of hBN/Pt(111), hBN/Ir(111), and hBN/Ru(0001).

To start with, I study the epitaxial growth of hBN on Ru(0001) and Ir(111) (Sec. 4.1). Two different preparation procedures are tested: chemical vapor deposition (CVD), and temperature programmed growth (TPG). The LEED and STM study reveals easy alignment between hBN and Ir(111). But aligned hBN on Ru(0001) requires more demanding growth procedures. In Sec. 4.2, the measurement results from PE characterization methods on hBN/Pt(111) and hBN/Ir(111) are presented.

The epitaxy of hBN on the transition metal (TM) substrate leads to the interaction between hBN and the underlying substrate. Due to the lattice mismatch, the hBN-TM interaction periodically modulates the geometric and electronic structure of the hBN. This spatial periodicity constitutes a moiré pattern, which I observe on both hBN/Ru(0001) and hBN/Ir(111). In the regions where the interaction is strong/weak, the distance between hBN and the TM substrate is small/large (valleys/hills), rendering a corrugation geometry of the hBN layer. The corrugation geometries of hBN/Pt(111), hBN/Ir(111), and hBN/Ru(0001) are discussed based on the measurement results of STM and photo-emission (PE) characterization.

The difference of the geometric structure measured on hBN/Ru(0001) and hBN/Ir(111) suggests that the strength of the 2DM-TM interaction varies for different TM substrates. In addition, the easily emerged rotational domains in hBN/Ru(0001) and gr/Ir(111) indicate a weaker interaction to the TM substrates of graphene than hBN. In Sec. 4.3, I grow in-plane hetero-structures of hBN

and graphene on Ru(0001) and Ir(111). LEED measurements reveal enhanced alignment of the sequentially grown graphene. I attribute this enhanced alignment of graphene to the in-plane epitaxy to hBN.

The term "interaction strength" frequently used in the research of 2DM/TM is only a qualitative and macroscopic description, which integrate two crucial factors: the local interaction and the lattice mismatch between 2DM and the TM substrate. In Chap. 5, I try to separate these two factors and focus on the local atomic interaction. I calculate the adsorption of representative B/N containing molecules on TM surfaces to simulate the local atomic interaction. The calculation is within the scope of density functional theory (DFT).

Beside the geometric corrugation, the moiré pattern of hBN/TM generates a spatial modulation of the electronic properties of hBN/TM, hence providing a periodic template for adsorbates. In Chap. 6, I introduce alkali metals (Cs and K) into hBN/Ru(0001) (Sec. 6.1) and hBN/Ir(111) (Sec. 6.2) to study this templating effect. The STM measurements reveal, hBN/Ru(0001) and hBN/Ir(111) are very different templates: the preferred adsorption sites on hBN/Ru(0001) are the valley regions of the moiré unit cells, and on hBN/Ir(111) it is the hill regions. Furthermore, one valley regions on hBN/Ru(0001) can accommodate multiple alkali metal atoms, while only one single alkali metal atom can adsorb in one hill region of the hBN/Ir(111) moiré unit cell. In Sec. 6.3, I focus on an interesting feature of Cs adsorption on hBN/Ir(111). Two hill regions exist in one moiré unit cell. With the proper preparation procedure, the adsorbed Cs atoms form a honeycomb lattice.

Due to the low concentration, the alkali metal adsorption induces little modulation to the geometric and electronic structure of hBN. The angular resolved photo-emission spectroscopy (ARPES) measurements demonstrate a small rigid shift of the hBN bands towards higher binding energy (BE). To pursue a larger shift, ample alkali metal is incorporated into hBN/Ir(111) in Chap. 7. In this case, alkali metal intercalates and lifts the hBN layer up from the TM substrate. PE measurements detect large shifts of both the hBN bands and N/B 1s core levels to higher BE. Especially, ample Cs incorporation induces the largest shift of the hBN bands (3.56 eV). In the ARPES mapping of the band structure, the conduction bands of hBN is still absence below the Fermi energy. Assuming a rigid shift, this observation sets a lower bond of 5.85 eV for the hBN band gap.

Chapter 2

Theoretical Background

The discovery of graphene [1] is the start of the family of two-dimensional materials (2DM). 2DMs are the type of materials which are only one or a few atomic layer thick. By definition, 2DMs are of the smallest thickness. From a practical point of view, the ultra-thin nature of 2DMs provides new route for nanometer sized electronic devices and thus integrated circuit with higher performance. From the aspect of scientific curiosity, 2DMs pushes thin film physics to its dimensional limit. Many novel properties, electronic, optical, and mechanical, emerge in 2DMs.

The 2DM I focus on in this thesis is monolayer hexagonal boron nitride (hBN). This introductory chapter starts with the free-standing hBN, and its more famous cousin, graphene. The atomic structure and the electronic structure are introduced in Sec. 2.1. High-quality hBN can be prepared by epitaxial growth on TM surfaces. In Sec. 2.2.2, I focus on this epitaxial system, hBN/TM. The atomic structure of the (111)-surface of Pt and Ir, the TM surfaces I grow the 2DMs on, is briefly discussed in Sec. 2.2.1. Due to the lattice mismatch between the 2DM and the TM substrates, a periodic superstructure form, i.e. moiré pattern. The structure of the moiré unit cell is discussed in detail in Sec. 2.2.2. In Sec. 2.3, I introduce the incorporation of external atoms and molecules in the hBN/TM systems. This section includes the site-selectively adsorption for some atoms and molecules on hBN/TM (Sec. 2.3.1), and the geometric and electronic modification of hBN generated by alkali metal incorporation (Sec. 2.3.2).

2.1 Graphene and hBN

Graphene is formed by one single layer of C atoms. The C atoms form a honeycomb structure (Fig. 2.1a). Its Bravais lattice is hexagonal, and the basis consists of two C atoms. hBN is iso-structural to graphene, with the C atoms replaced by alternating N and B atoms (Fig. 2.1b). These two 2DMs have very similar lattice constants (graphene: 2.46 A [2], hBN: 2.49 A [3]), which leads to the possibility for them to form an atomically continuous hetero-structure. The growth of such in-plane heterostructure is discussed in Sec. 4.3.

For each atom in these two 2DMs, its $2s$, and two $2p$ orbitals (e.g. p_x and p_y) hybridize into three sp^2 orbitals, and expand in the x-y plane (Fig. 2.1c). Two sp^2 orbitals from the nearest neighboring atoms point toward each other and overlap, forming a σ-bond. These strong in-plane σ-bonds give

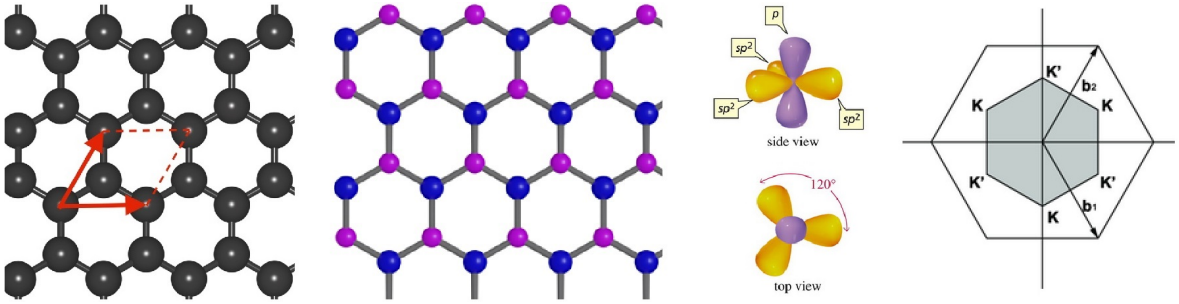

Figure 2.1: Atomic structure of graphene and hBN. The two red arrows indicate the primitive translational vectors. The rhombus indicates one primitive unit cell, which contains a bi-atomic basis.

rise to the superior mechanical strength of graphene and hBN: The ultimate tensile strength of graphene is 125 GPa [4], and hBN 70 GPa [4]. As a comparison, the ultimate tensile strength of copper (0.2 GPa [5]) and tungsten (0.55 to 0.62 GPa [5]) are relatively small. The remaining p_z orbital is perpendicular to the x-y plane.

The similarity between graphene and hBN in real space leads to the similar hexagonal reciprocal lattice. The 1st Brillouin zone is a normal hexagon (Fig. 2.1d). The high symmetry points are labeled in the Figure. The band structure along the Γ-K direction is presented in Fig. 2.2. Since the in-plane σ-bonds are very similar in graphene and hBN, the σ-bands of hBN and graphene are also very similar in shape.

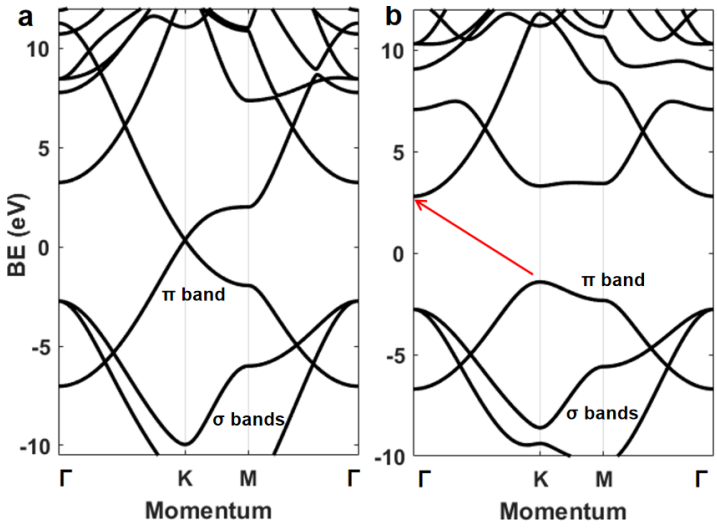

Figure 2.2: Band structure of (a) graphene and (b) hBN calculated by DFT.

In graphene, the C atom has four electrons in the L shell. Besides the three electrons forming the three σ-bonds, one remains in the p_z orbital. similar to the situation in benzene, the p_z orbitals of the neighboring atoms overlap each other side by side, forming a large molecular orbital, i.e. the π-bond. This molecular orbital provides a network for the p_z electrons. The π- and π^*-bands cross

each other at the corner of the 1BZ. Since each C atom provides one electron, the Fermi level is at the crossing point. Fig. 2.2b presents the band structure of graphene near the Fermi energy, calculated by the author with the Perdew-Burke-Ernzerhof GGA functional [6] using the ABINIT code [7, 8].

The situation is very different for hBN, where the p_z electrons are bonded to the N atoms. One B atom has three electrons in the L shell, all of which form the three in-plane σ-bonds. For a N atom, two electrons are left in the p_z orbital. However, due to the uneven potential on B and N atom, the two electrons are locally bonded to the N atom, making hBN an insulator. Thus the π-band formed by the p_z orbitals of the N atoms is fully occupied, while the π^*-band formed by the p_z orbitals of the B atoms is completely empty, leaving a large band gap between the π- and π^*-bands. The band structure of hBN is presented in Fig. 2.2b.

Though the wide band gap is one of the most appealing features of hBN, some important characteristics of its band structure remain unclear. In the reported density functional theory (DFT) calculations, both direct K-K band gap[9, 10, 11] and indirect Γ-K band gap [9, 12, 13, 14, 15] have been reported. In addition, the calculated band gap size varies from 4.3 eV [13] to 6.86 eV [9]. Especially, H. Sahin *et al.* demonstrate that the calculated size of the band gap and the HOMO/LUMO positions in the Brillouin zone is highly dependent on the pseudo-potential used in the DFT simulation [9]. On the experimental aspect, a measurement of a 5 eV band gap on hBN/Ir(111) by scanning tunneling spectroscopy was reported by M. Liu *et al.* [16]. Whereas optical absorption spectroscopy measurements reveal a 6.07 eV optical band gap [17, 18, 19]. It is worth mentioning that the optical band gap is not necessarily the same as the electronic band gap for two reasons: (i) Due to the small momentum of the photons, incident light can not excite the electrons through an indirect band gap. (ii) The excitation of an exciton reduce the photon energy needed, rendering the optical band gap smaller than the electronic band gap.

2.2 Epitaxial graphene and hBN on TM surfaces

In 2004, graphene was first unambiguously produced by A. Geim and K. Novoselov by scotch-tape method [1]. The single layer material was exfoliated from bulk graphite. Ever since, many production methods have been developed for 2DMs.

A 2DM normally have a parent bulk material. For example, bulk hBN consists of a large number of single-layer hBN. Many preparation methods of the 2DMs start with the corresponding bulk materials, and the single layers are separated from the bulk. This kind of preparation methods is categorized as top down methods. Beside the mechanical cleavage (scotch-tape method), the top down methods also include liquid phase exfoliation [20] and reduction of graphene oxide [21].

Many techniques have been developed in top down methods. But the quality of 2DMs produced by these methods is low and uncontrollable. For high quality 2DMs, the bottom up methods are used. The method I use in this study is the epitaxial growth on transition metal (TM) substrates. Before introducing the epitaxial growth, I would like to point out that both bottom up and top down methods have their own advantages and disadvantages. For example, the high cost of the bottom up methods has so far limited the application of these methods in mass production. A comparison among all the preparation methods can be found in Ref. [22].

In this study, I grow epitaxial hBN (graphene) on the low index surfaces of TM crystals, which play an important role in the structure of hBN (graphene). We first discuss the atomic structure of these TM surfaces in Sec. 2.2.1. The structure of the hBN/TM (graphene/TM) is discussed in Sec. 2.2.2.

2.2.1 (111)-surface of fcc metal and (001)-surface of hpc metal

To match the symmetry of hBN (graphene), the (111)-surface of the face-centered cubic TMs (Fig. 2.3a) and the (001)-surface of the hexagonal close packed TMs (Fig. 2.3b) are used. These surfaces have very similar atomic structure.

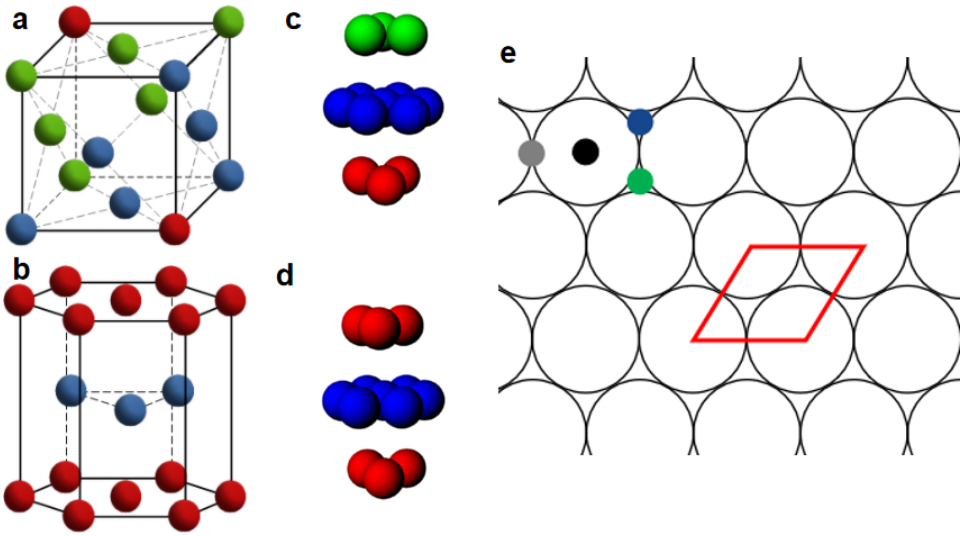

Figure 2.3: Atomic structure of (a) fcc crystals and (b) hcp crystals. The atomic layers are indicated by different colors. Stacking relation among the atomic layers in (c) fcc crystals in the (111)-direction and (d) hcp crystals in the (001)-direction. (d) Surface registries on a hexagonal surface indicated by the colored spheres. The unit cell is indicated by the red rhombus.

For both surfaces, the top layer TM atoms form a hexagonal lattice (Fig. 2.3e). There are some special registries on these surfaces (indicated by colored spheres in Fig. 2.3e). Directly on top of a TM metal is the atop site (black). In the middle of two neighboring atoms is the bridge site (gray). The blue and green spheres represent the hollow sites on the surface. When only the topmost layer of TM atoms are considered, the registries indicated by blue and green spheres are identical: a single layer system has a six-fold symmetry.

For an actual system including more than one layer of TM atoms, the two registries (green and blue) are different. The second layer TM atoms also form a hexagonal lattice. Assuming one atom in the second layer is precisely below the blue sphere, then no atom is below the green sphere. Hence the second layer of TM atoms distinguish the two hollow sites. In the (111) direction of the fcc crystals, the atomic layers are stacked in the ABC ordering (Fig. 2.3c), i.e. the third layer atoms are not below the first layer atoms. This stacking relation is similar to the green sphere in Fig. 2.3e. Thus the green registry is called fcc-hollow site. In the (001) direction of the hcp crystals, the atomic

layers are stacked in the ABA ordering. Namely, the even (odd) layers are precisely on top of each other. This stacking relation is the same as the blue sphere in Fig. 2.3e. Hence the blue registry is called hcp-hollow site.

2.2.2 Moiré pattern of the 2DM/TM systems

Except the rare coincidental cases, hBN (graphene) has a smaller lattice constant than the TM surfaces. The periodic atomic structures of hBN (graphene) and the TM surfaces produce a third larger periodic pattern, the moiré pattern. In the epitaxial systems I study in this thesis, both hBN (graphene) and the TM surfaces have hexagonal lattice. The moiré pattern is thus also hexagonal. The extended epitaxial system of 2DM/TM is the repetition of the moiré unit cells in a hexagonal lattice.

Within one moiré unit cell of hBN/TM, the N/B atoms are at different registries of the TM surface due to the lattice mismatch. Hence the interaction strength between the N/B atoms in hBN and the substrate vary. When A N atom is at the atop registry of the TM surface, this interaction is the strongest. In this region of the hBN/TM, the distance between the hBN and the TM substrate is the smallest. In the area where the N atom is not on top of an TM atom, the hBN-TM distance is large. Hence the spatially modulated hBN-TM interaction generates a corrugation geometry of the the hBN layer.

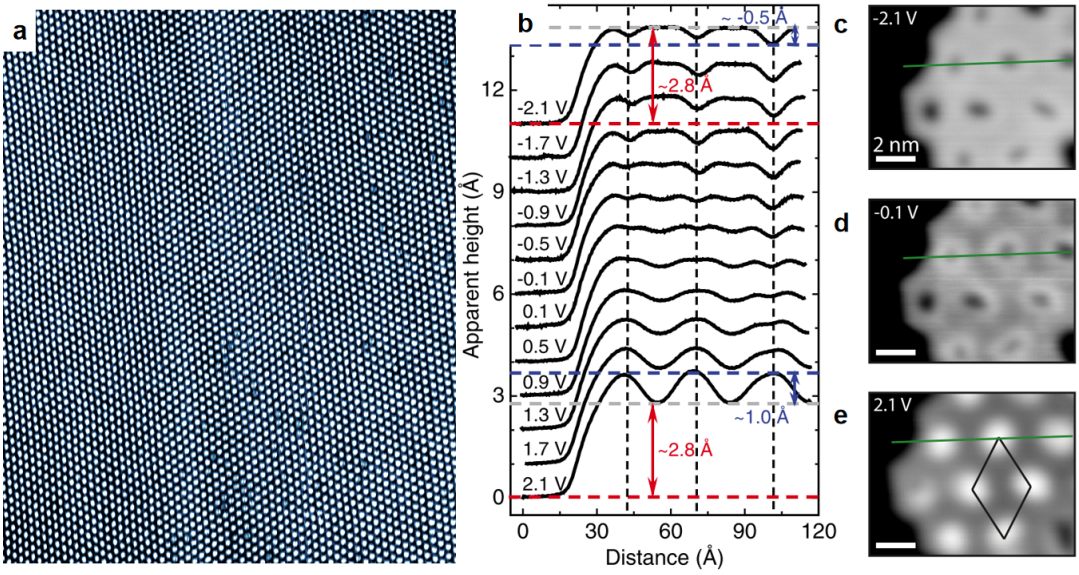

Figure 2.4: STM measurement results on hBN/Ir(111). (a) STM images on hBN/Ir(111), 200×150 nm^2, $U_\mathrm{b} = 2.4$ V, $I_\mathrm{tunneling} = 80$ pA. (b) Apparent height profile along the lines on hBN/Ir(111) crossing three moiré unit cell. (c)-(e) STM images of the same area of a hBN flake on Ir(111), imaged with different U_b. $I_\mathrm{tunneling} = 250$ pA for (c)-(e). (b)-(e) modified from Ref. [23].

Fig. 2.4a presents a large scale STM image of hBN/Ir(111). The periodic moiré pattern is very pronounced. However, the bright protrusions observed are actually the valley regions of the moiré unit cells, where the hBN-Ir(111) distance is low. The apparent height contrast is inversed from

the hBN-Ir(111) distance. F. Schulz *et al.* imaged the same area on hBN/Ir(111) with different bias voltages [23]. They observed that the apparent heights of different regions in the moiré unit cell depend on the bias voltage (Fig. 2.4b to e). The same contrast inversion is observed on hBN/Rh(111) by STM [24] and also by nc-AFM [25]. This uncertainty of height measurements by STM and AFM originates from the spatially modulated local electronic structure in the moiré unit cell, which STM and AFM measurements are highly sensitive to.

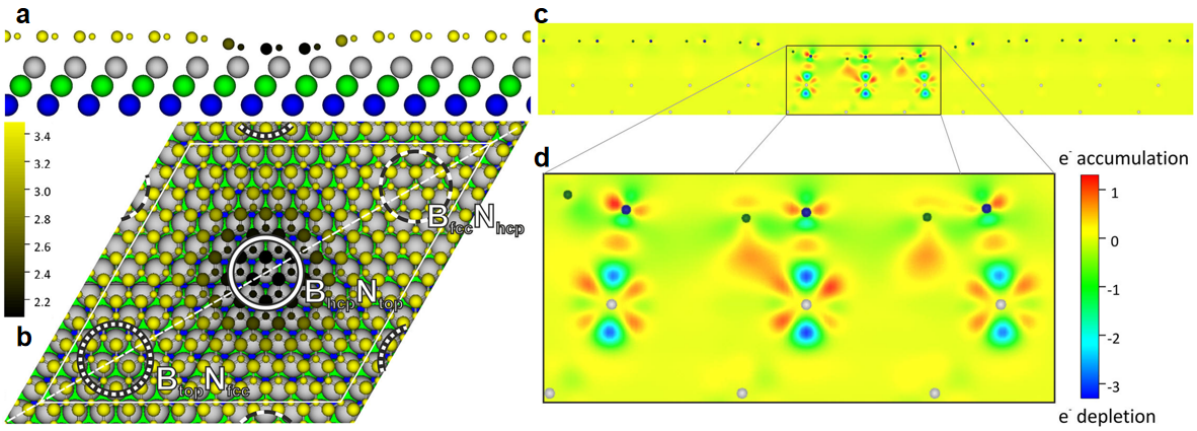

Figure 2.5: Moiré unit cell of hBN/Ir(111) calculated by DFT [26]. (a) Side view and (b) top view of the atomic structure. The height of the N/B atoms are presented by the color scale. The three typical regions in the moiré unit cell, where the N/B atoms are at specific surface registries are labeled by three circles. (c) Charge rearrangement mapping in hBN/Ir(111). (d) Magnified view of the charge transfer in the valley region. Red indicates electron accumulation, and blue indicates depletion.

Ref. [26] reports a sophisticated study of the moiré geometry of hBN/Ir(111). The DFT calculation and XSW measurements both reveal a 1.5 Å corrugation of the hBN layer. In the DFT calculation, three typical areas are identified within a moiré unit cell. The regions where the N atoms are at the atop registries of the Ir(111) surface, and B atoms are at the hcp hollow sites ($B_{hcp}N_{top}$) are identified as valleys due to the small hBN-Ir(111) distance (2.2 Å). In the regions where the N atoms are at the hcp registries and B atoms are at the fcc registries ($B_{fcc}N_{hcp}$), and the regions where the N atoms are at the fcc registries and B atoms are at the atop registries ($B_{top}N_{fcc}$), the distance between hBN and the Ir(111) substrate is large. These two regions are identified as hills. Fig. 2.5a presents the geometric structure of the moiré unit cell (side and top view).

Fig. 2.5d presents the charge rearrangement between hBN and the Ir(111) substrate in the moiré unit cell. Most charge rearrangement happens in the valley regions. In the valley regions (Fig. 2.5e) where the hBN-TM distance is small, DFT calculation reveals a charge depletion for the N p_z and Ir d_{z^2} atomic orbitals compensated by a charge accumulation between the two atoms. This charge rearrangement suggests a chemical bond formed between the Ir and the N atom. The correspondence between the small hBN-TM distance and the atop position of the N atoms is not exclusive for the Ir(111) substrate. The same corrugation geometry is also found on Rh(111) [27], and Ru(0001) [28].

2.3 Atomic and molecular incorporation in hBN/TM systems

In this section, I discuss the incorporation of external substance in the epitaxial system of hBN/TM. In this thesis, I focus on the incorporation of atoms and small molecules. The incorporation leads to mutual influence between the external substance and the hBN/TM substrate. The two following subsections discuss this mutual influence.

2.3.1 Templating effect

For atoms and small molecules, when incorporated in hBN/TM, they have two possible destinations: above or below the hBN layer. The choice depends on the size of the atoms/molecules. For small atoms like H [29] and Li [30], they penetrate the hBN layer and absorb between hBN and the TM substrate. Most other atoms and molecules with larger size adsorb on top of the hBN layer.

In the last section, I have discussed the geometric structure of hBN in the moiré unit cell: the hBN layer corrugates in the direction normal to the TM substrate. Beside the geometric modulation, the moiré pattern also produces an electronic modulation within the moiré unit cell. For example, F. Schulz *et al.* reported the local work function variation within the moiré unit cell [23]. The *I*-*z* curves are measured in the valley region and the hill regions (Fig. 2.6a). The local work function extracted from the *I*-*z* curves reveal a 0.5 eV difference. The local work function in the hill regions is larger than in the valley regions.

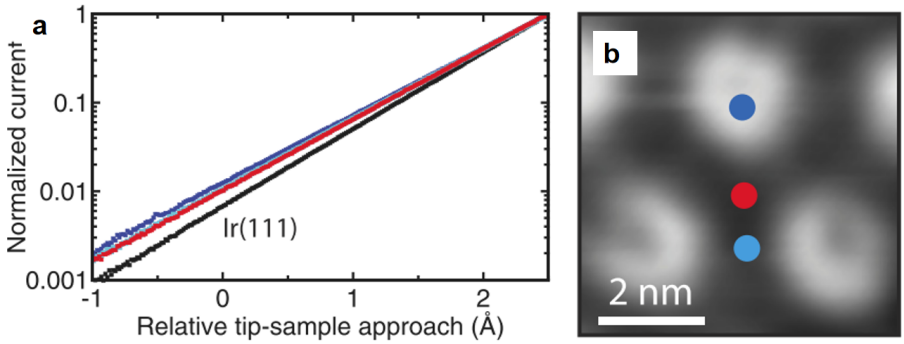

Figure 2.6: (a) *I*-*z* curves measured at different positions in the moiré unit cell of hBN/Ir(111) and on bare Ir(111). The red, dark and light blue curves are measured at the positions of the corresponding dots in (b) the STM image.

The spatial modulation of hBN/TM moiré pattern functions leads to site-selective adsorption. The exclusive adsorption of Au particles in the valley regions of hBN/Ru(0001) is observed by STM measurements [31]. To investigate this selective adsorption, B. Wang *et al.* calculated the adsorption energy of a single Au atom on hBN/Ru(0001) with DFT: the adsorption energy is 1.2 eV larger in the valley regions than in the hill regions [32]. According to their adsorption energy is also different in the two different hill regions (1.1 eV in $N_{hcp}B_{top}$, 0.7 eV in $N_{fcc}B_{hcp}$). The same selective adsorption in the valley regions is observed for Ti, Co, Mn, Fe, and Xe [33, 34, 35, 36] on hBN/Rh(111), and for Ir on hBN/Ir(111) [37]. Interesting, for Xe adsorption on hBN/Rh(111), the best adsorption site is not the center of the valley regions, but rather the edge. This off-center adsorption in the valley

regions is also observed for some organic molecules [27, 38]. A few examples of these site-selective adsorption is presented in the STM images in Fig. 2.7a to c.

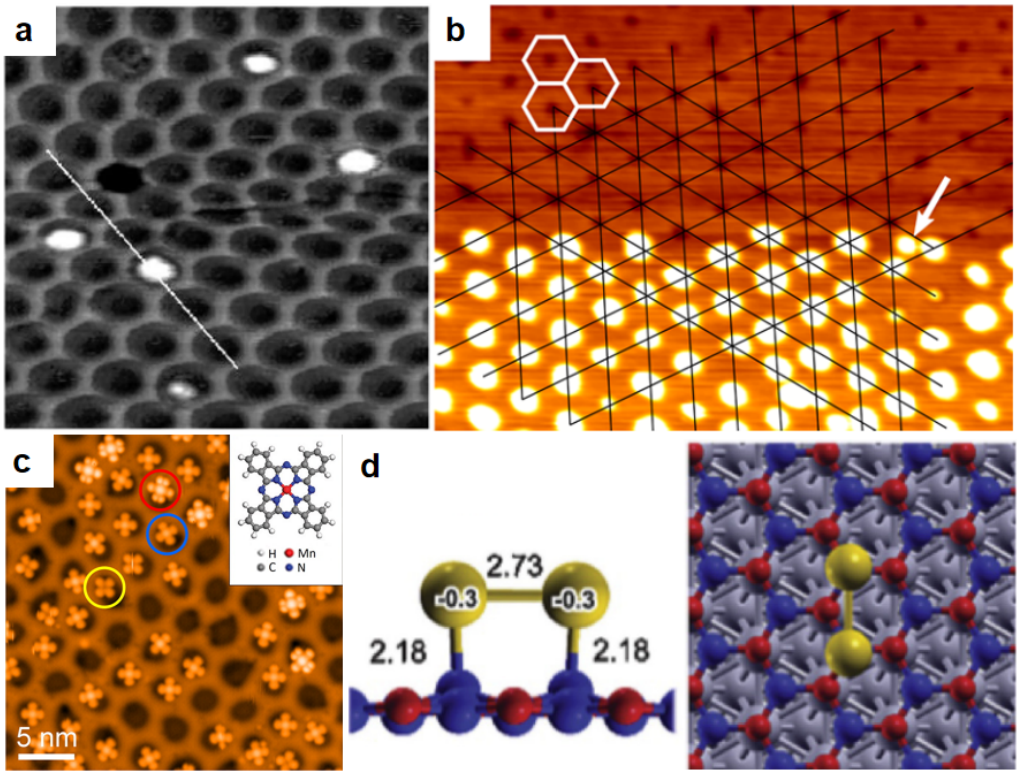

Figure 2.7: (a) Adsorption of Au atom on hBN/Ru(0001), modified from Ref. [31]. (b) Ir adsorption on hBN/Ir(111), modified from Ref. [37]. (c) Adsorption of MnPc on hBN/Rh(111), modified from Ref. [38]. (d) DFT calculated adsorption geometry of Au on hBN/Rh(111), modified from Ref. [39].

For the TM adatoms, DFT calculations reveal the TM-hBN interaction is fulfilled by a chemical bond formed between a B atom in hBN and the adsorbed TM atom [37, 39, 40] (Fig. 2.7d). As described in Sec. 2.2, the TM-N bond between hBN and TM substrate is formed by the overlap of the p_z orbital of the N atom and the d_{z^2} orbital of the TM atom. However, between adsorbed TM and hBN, all out-of-plane d_{z^2}, d_{xz}, d_{yz} orbitals of a TM atom contribute to the TM-B bond.

Due to the site-selective adsorption, the adsorbed substance can form ordered arrays. For example, W. Moritz *et al.* prepared an ordered array of the Ir clusters on hBN/Ir(111) (Fig. 2.7b). The clusters are removed in the upper part of the image to produce clear identification of the valley and hill regions. For adsorbates of higher concentration, the aggregation geometry varies for different adsorbates and different TM substrates. W. C. McKee *et al.* investigated the influence of the diffusion barrier on the aggregation geometry [41]. The adsorption of various TMs on hBN/Rh(111) were calculated with DFT. For adatoms (e.g. Au and Pt) having high barriers to diffuse between valley regions, the STM measurements reveal that they form mono-disperse nano-particles. On the other hand, it is easier for Ag adatoms to diffuse between valley sites. They form large clusters extending over multiple valley regions.

2.3.2 Gating effect

In the last subsection, I discuss the template effect of the moiré pattern of hBN/TM, namely the influence of the hBN/TM substrate on the incorporated substance. In return, the geometric and electronic structure of hBN is also modified by the incorporated substance.

For example, in Ref. [37], DFT calculation reveals the extra buckling of the hBN sheet below the Ir clusters due to the interaction to the Ir clusters. In addition, as described in Sec. 2.2.2, the 2DMs are normally corrugated due to the spatially modulated interaction with the TM substrate. It has long been demonstrated that intercalation provides a approach to remove this corrugation [42].

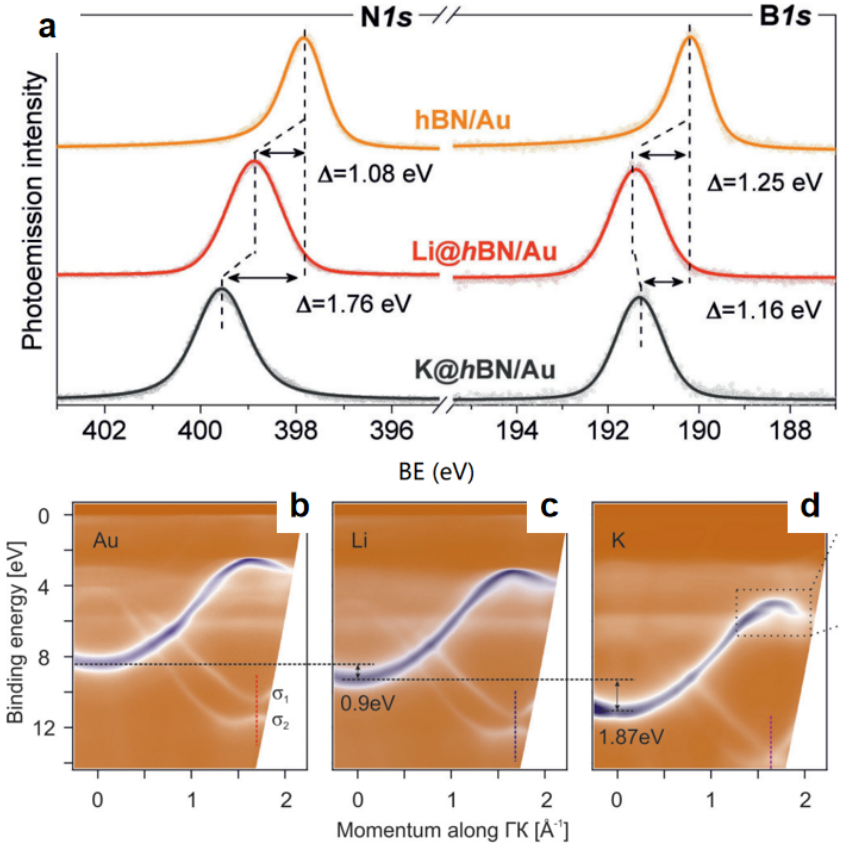

Figure 2.8: (a) N 1s and B 1s spectra measured on hBN/Au/Ni(111), Li/hBN/Au/Ni(111), and hBN/K/Au/Ni(111). ARPES mapping of the band structure measured on (b) hBN/Au, (c) Li/hBN/Au/Ni(111), and (d) hBN/K/Au/Ni(111). Modified from Ref. [43]

As for modifying the electronic structure, it is most effective to incorporate alkali metals due to their lowest ionization energies, which leads to the easy charge transfer. In Ref. [43], two different alkali metals, Li and K, are introduced into the system of hBN/Au/Ni(111). As it turns out, Li adsorbs on top of the hBN layer, while K intercalates. In both systems, the N 1s and B 1s core levels are shifted to higher binding energy (Fig. 2.8a). ARPES measurements reveal that the hBN bands are also shifted to higher binding energy (Fig. 2.8b to d).

Chapter 3

Experimentation

This chapter gives a brief introduction of the experimental methods and set-ups used in this study. Four main characterization methods are involved. Their working principles are briefly explained in Sec. 3.1 (LEED), Sec. 3.2 (STM), Sec. 3.3 (XPS), and Sec. 3.4 (XSW). The two main experimental setups involved in this study are introduced in 3.5.

3.1 LEED

Among all surface structural characterization methods, low-energy electron diffraction (LEED) is by far the most commonly used in the surface science community. The core phenomena is electron scattering by the periodic atomic structure of the sample surface. In the energy range related to LEED, the penetration depth monotonically increases with the energy of the electron. Low energy (around 100 eV) electron beam is used to achieve surface sensitivity (penetration depth less than 10 Å, i.e. a few atomic layers). An electron gun emits the monochromatic electron beam, and a fluorescent screen is used to collect and display the diffracted electrons (Fig. 3.1a).

Here we only consider the dominating elastic scattering, i.e. the electron energy is conserved in the scattering process. The parallel momenta of the incident and scattered electron are $\hbar\vec{k}_{\mathrm{i}}$ and $\hbar\vec{k}_{\mathrm{f}}$, and the change in the wave number is $\Delta\vec{k}$. The only non-neglectable scattering processes are the ones whose $\Delta\vec{k}$ coincides with a reciprocal lattice vector of the surface $\vec{g}$. The incident electron beam is normal to the sample surface ($\vec{p}_{\mathrm{i}} = \hbar\vec{k}_{\mathrm{i}} = 0$). Thus $\vec{k}_{\mathrm{f}} = \vec{g}$. The reciprocal lattice is directly presented on the fluorescent screen.

In this study, I use low index surfaces of transition metal single crystals, Pt(111), Ir(111) and Ru(0001). They all have the hexagonal arrangement of the metal atoms, which leads a hexagonal LEED pattern. The 2DMs in this study (graphene and hBN) have a honeycomb lattice, which is a hexagonal lattice with a biatomic basis. Thus the LEED pattern of the 2DM/TM system is also hexagonal. The 2DM and the TM substrates have different lattice constants. Thus the LEED pattern contains two sets of hexagonal lattices. Beside the two hexagonal lattices, satellite spots are also present in the LEED pattern, which are from the multi-scattering process. A typical LEED pattern of 2DM/TM is presented in Fig. 3.1b.

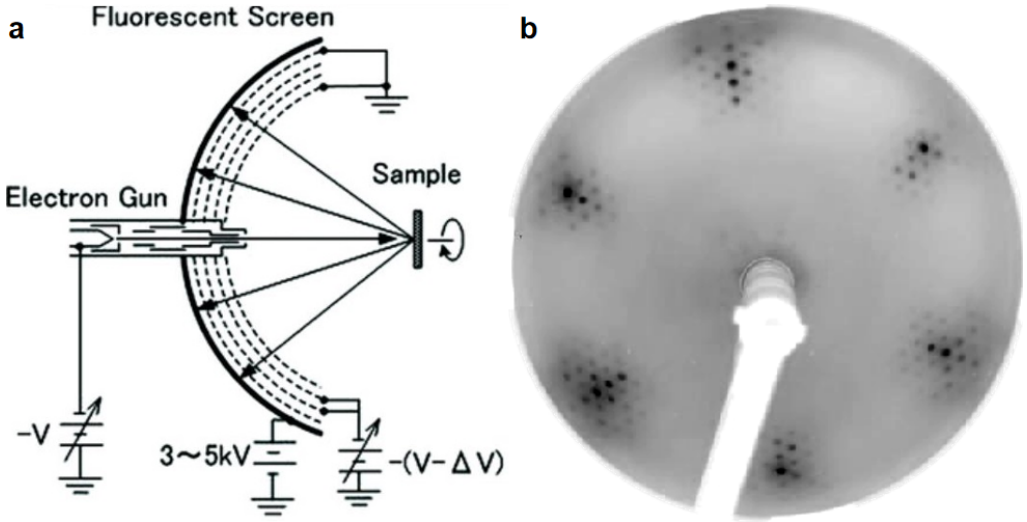

Figure 3.1: (a) A sketch of LEED setup, modified from [44]. (b) LEED pattern of hBN/Ir(111) (72 eV).

3.2 STM

Scanning tunneling microscopy (STM) is a technique that profoundly shaped condensed matter physics. It is often said that STM is to surface science what the telescope was to astronomy. Actually this saying underestimates the importance of STM. As Chen said in his book [46]: *Yet STM is capable of manipulating the objects it observes, to build nanoscale structures never existed in nature. No telescope is capable of bringing Mars and Venus together.* The inventors of STM, Gerd Binning and Heinrich Rohrer were awarded the Nobel physics prize in 1986. This section gives a brief introduction to the basics of this technique, mainly Bardeen's transfer Hamiltonian method in the one dimensional case. For a more detailed and advanced introduction to this technique, the reader is suggested to refer to literature [46, 47, 45].

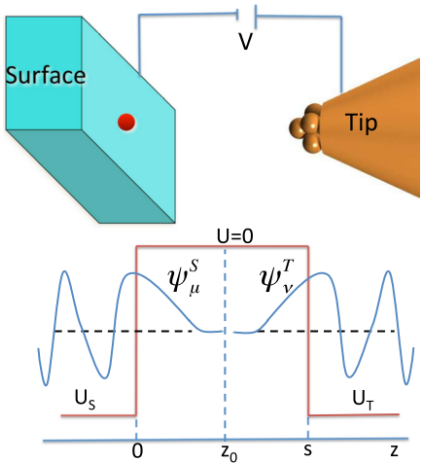

Figure 3.2: 1D model of the tunneling process between the tip and the sample [45].

The STM technique uses the simple idea of the quantum tunneling effect. A bias voltage between two electrodes separated by sub-nanometer-sized vacuum (Figure 3.2) drives a tunneling current between the two electrodes. One of the electrodes is the sample surface in investigation, while the other is the conducting probe, which in the ideal case is an atomically sharp metal tip.

The STM tip is attached to a piezo-drive, which consists of three mutually perpendicular piezoelectric transducers ($x-$, $y-$, $z-$piezos). Upon applying a voltage, a piezoelectric transducer contracts or expands, moving the tip on the surface.

A few presumptions are required for the following deduction. First of all, the interaction between tunneling electrons is ignored. Secondly, direct interaction of the tip and sample giving birth to coupled electronic states is excluded. This assumption is valid if the tip-sample distance is large enough (larger than $\sim$ 4 Å). Furthermore, we assume elastic tunneling, i.e. no energy loss of the electrons with quasi-particles in the electrodes, e.g. plasmons, phonons, etc.

When the tip is far away from the sample, the wave function of the electron in the sample (S), and the wave function in the tip (T), satisfy the Schrödinger equation:

$$i\hbar\frac{\partial}{\partial t}\psi^i = (-\frac{\hbar^2}{2m}\frac{\partial^2}{\partial z^2} + U_i)\psi^i, \tag{3.1}$$

where U_i is the potential function of electrode i (S or T), and ψ^i depends on both time and spatial coordinates. The stationary states are $\psi^i = \psi^i_\mu e^{-iE^i_\mu t/\hbar}$, with

$$(-\frac{\hbar^2}{2m}\frac{\partial^2}{\partial z^2} + U_i)\psi^i_\mu = E^i_0\psi^i_\mu, \tag{3.2}$$

where μ is the quantum number labeling different eigenstates.

Once the tip is close enough to the sample surface, the Schrördinger equation contains both potentials:

$$i\hbar\frac{\partial}{\partial t}\psi = (-\frac{\hbar^2}{2m}\frac{\partial^2}{\partial z^2} + U_\mathrm{T} + U_\mathrm{S})\psi. \tag{3.3}$$

At $t \to -\infty$, the tip is far away from the substrate and the electrons in both electrodes are in the eigenstates the Schrödinger equation (Eq. 3.2) describes, and will evolve following Eq. 3.1. The potential of the tip will be present while the tip approaching the sample. We treat the tip potential as a perturbation. We assume that the tip approaches the sample surface slowly, thereby the tip potential is turned on adiabatically. Formally we describe this adiabatic switching of the perturbation via a time-dependent potential

$$U_T(t) = U_T e^{\eta t/\hbar}, \mu > 0, \tag{3.4}$$

where U_T is independent on t and η is small and positive. At the end, η is set to 0 to make it real adiabatic.

Switching on the perturbation, the electron has a probability of populating the states of the tip states, denoted as ψ^T_ν. The electronic state which was initially ψ^S_μ evolves to:

$$\psi = a_\mu(t)\psi^\mathrm{S}_\mu e^{-iE^\mathrm{S}_\mu t/\hbar} + \sum_\nu c_\nu\psi^\mathrm{T}_\nu e^{-iE^\mathrm{T}_\nu t/\hbar}. \tag{3.5}$$

From our ansatz, $a_\mu(-\infty) = 1$ and $c_\nu(-\infty) = 0$.

The basic assumption of Bardeen's model is that the two sets of wave functions are approximately orthogonal, i.e. $\langle\psi^\mathrm{S}_\mu|\psi^\mathrm{T}_\nu\rangle = 0$. Inserting Eq. 3.5 into the time-dependent Schrödinger equation (Eq. 3.3), we obtain

$$i\hbar\frac{dc_\mu(t)}{dt} = \langle\psi^\mathrm{T}_\nu|U_T|\psi^\mathrm{S}_\mu\rangle\, e^{-i(E^\mathrm{S}_\mu - E^\mathrm{T}_\nu + i\eta)t/\hbar} + \sum_\lambda c_\lambda(t)\,\langle\psi^\mathrm{T}_\nu|U_S|\psi^\mathrm{S}_\lambda\rangle\, e^{-i(E^\mathrm{T}_\lambda - E^\mathrm{T}_\mu)t/\hbar}. \tag{3.6}$$

Two approximations have been used to achieve Eq.3.6. First of all, $a(t)$ varies slowly due to adiabatic process, i.e. $\frac{d}{dt}a_\mu(t) = 0$. Secondly, the contribution $\sim (e^{\eta t/\hbar} - 1)$ is neglected since it vanishes at $\eta \to 0$.

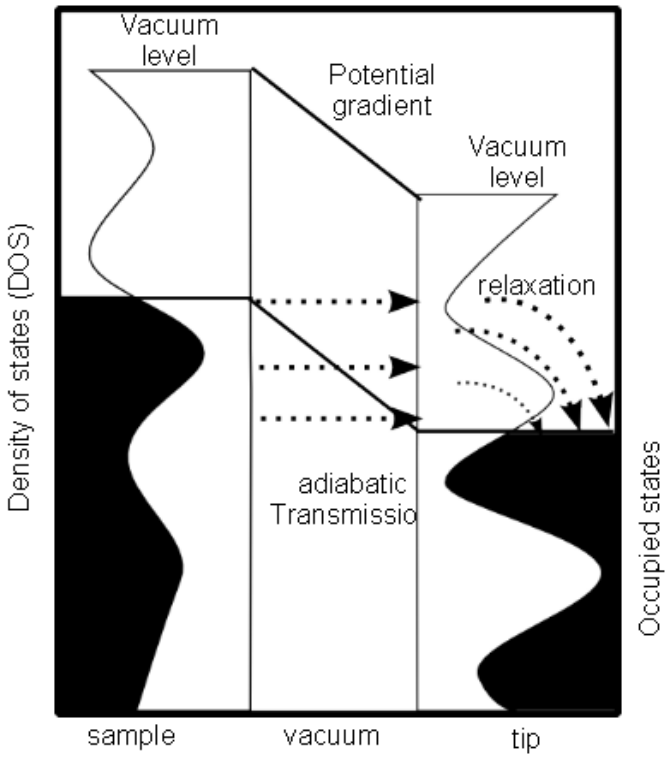

Figure 3.3: Sketch of the electron tunneling process between the tip and the sample in STM measurement. The electron transits from the occupied states in the sample to the unoccupied sates in the tip. [48]

This equation can be solved iteratively, but as a good approximation we focus only on the first order of time-dependent perturbation theory and neglect the second term on the right hand side. Then we obtain:

$$c_\mu(t) = \frac{M_{\mu\nu}}{E_\mu^{\mathrm{S}} - E_\nu^{\mathrm{T}} + i\eta} e^{-i(E_\mu^{\mathrm{S}} - E_\nu^{\mathrm{T}} + i\eta)t/\hbar}, \tag{3.7}$$

with $M_{\mu\nu} = \langle \psi_\nu^{\mathrm{T}} | U_T | \psi_\mu^{\mathrm{S}} \rangle$ being the tunneling matrix element describing the projection of the initial state ψ_μ^{S} perturbed by the potential U_T onto the final state ψ_ν^{T}.

The term $|c_\mu(t)|^2$ describes the probability that an electron which sits in the initial state ψ_μ^{S} at $t = -\infty$ populates a state ψ_ν^{T} at time t:

$$|c_\mu(t)|^2 = \frac{|M_{\mu\nu}|^2}{(E_\mu^{\mathrm{S}} - E_\nu^{\mathrm{T}})^2 + \eta^2} e^{2\eta t/\hbar}, \tag{3.8}$$

which leads to the tunneling probability per unit time

$$P_{\mu\nu} = \frac{d}{dt}|c_\mu(t)|^2 = \frac{2\eta}{(E_\mu^{\mathrm{S}} - E_\nu^{\mathrm{T}})^2 + \eta^2} \frac{1}{\hbar} e^{2\eta t/\hbar} |M_{\mu\nu}|^2. \tag{3.9}$$

Now we set η to 0. In the recognition of the delta function, i.e. $\delta(x) = \frac{1}{\pi} \lim_{\eta \to 0} \frac{\eta}{x^2 + \eta^2}$, we have the famous Fermi's golden rule:

$$P_{\mu\nu} = \frac{d}{dt}|c_\mu(t)|^2 = \frac{2\pi}{\hbar} \delta(E_\mu^{\mathrm{S}} - E_\nu^{\mathrm{T}}) |M_{\mu\nu}|^2. \tag{3.10}$$

The tunneling probability $P_{\mu\nu}$ connects the initial state ψ_μ^{S} and the final state ψ_ν^{T}. However, in both the tip and the sample, electrons sit in a lot of different states. So the tunneling current is

proportional to the sum of all the tunneling probabilities between different states in tip and sample. Furthermore, at finite temperature, we also have to include the thermal effect, which means the occupation probability of a state with eigenenergy E is described by the Fermi-Dirac distribution

$$f(E - E_f) = \frac{1}{e^{(E-E_f)/k_B T} + 1}. \tag{3.11}$$

Accounting for the occupation in this distribution, two spin directions in one state and assuming a bias voltage V, the tunneling current in thermal equilibrium from the sample to the tip, $I_{S\to T}$, and from the tip to the sample, $I_{T\to S}$ can be expressed as:

$$I_{S\to T} = \frac{4\pi e}{\hbar} \sum_{\mu\nu} f(E_\mu^{\mathrm{S}} - E_f^{\mathrm{S}})[1 - f(E_\nu^{\mathrm{T}} - E_f^{\mathrm{T}})]|M_{\mu\nu}|^2 \delta(E_\nu^{\mathrm{T}} - E_\mu^{\mathrm{S}} - eV), \tag{3.12}$$

and

$$I_{T\to S} = \frac{4\pi e}{\hbar} \sum_{\mu\nu} f(E_\mu^{\mathrm{T}} - E_f^{\mathrm{T}})[1 - f(E_\nu^{\mathrm{S}} - E_f^{\mathrm{S}})]|M_{\mu\nu}|^2 \delta(E_\nu^{\mathrm{T}} - E_\mu^{\mathrm{S}} - eV). \tag{3.13}$$

The difference between two directions is the net total tunneling current:

$$I = \frac{4\pi e}{\hbar} \sum_{\mu\nu} [f(E_\mu^{\mathrm{S}} - E_f^{\mathrm{S}}) - f(E_\mu^{\mathrm{T}} - E_f^{\mathrm{T}})]|M_{\mu\nu}|^2 \delta(E_\nu^{\mathrm{T}} - E_\mu^{\mathrm{S}} - eV). \tag{3.14}$$

The finite summation over the discrete states can be replaced by an integral over energies using the density of states $n(E)$: $\Sigma_\mu \to \int n(E)dE$. We can also get rid of the delta function using $\int \delta(x)dx = 1$. After appropriate change of variables, we have:

$$I = \frac{4\pi e}{\hbar} \int d\epsilon [f(E_f^{\mathrm{T}} - eV + \epsilon) - f(E_f^{\mathrm{S}} + \epsilon)] \times n^{\mathrm{T}}(E_f^{\mathrm{T}} - eV + \epsilon) \times n^{\mathrm{S}}(E_f^{\mathrm{S}} + \epsilon)|M(E_f^{\mathrm{S}} + \epsilon, E_f^{\mathrm{T}} - eV + \epsilon)|^2, \tag{3.15}$$

where n^{S} and n^{T} are the density of states (DOS) of the substrate and of the tip (Figure 3.3). At zero temperature or if $k_B T$ is smaller than the energy resolution required in the measurement, the Fermi distribution function can be approximated by a step function and the current simplifies to

$$I = \frac{4\pi e}{\hbar} \int_0^{eV} d\epsilon n^{\mathrm{T}}(E_f^{\mathrm{T}} - eV + \epsilon) n^{\mathrm{S}}(E_f^{\mathrm{S}} + \epsilon)|M|^2. \tag{3.16}$$

In Eq. 3.16, we find formally that the tunneling current is the convolution of the density of states of the tip and the sample.

In practice, we move the tip on the sample surface to detect the geometric structure. To keep the tunneling current constant, the tip-sample distance is regulated in order to modulate the overlap of electronic states of the tip and the sample, i.e. M. As can be seen in Eq. 3.16, the local density of states (LDOS) of the sample surface is of great importance to the tunneling current. Hence the precise height measurement on the sample is only possible for the surface of homogeneous DOS. However, this is not the case for any actual samples. The geometric structure measured with STM contains the information of the local DOS of the sample surface.

3.3 XPS

Historically the first experiments revealing the interaction of light with solids, known as the photoemission effect today, were performed by H. Hertz and W. Hallwachs (Dresden) in 1887 [49, 50]. In 1905, the *annus mirabilis*, A. Einstein invoked the quantum nature of light and introduced the concept of photon. He concludes the photoemission effect by the relation between the photon energy $h\nu$ and the maximum kinetic energy $E_{\text{kin}}^{\text{max}}$ of the emitted electrons $E_{\text{kin}}^{\text{max}} = h\nu - \phi$. The popular application of photoemission was only possible in the 1960s, after the necessary instrumental development by Kai Siegbahn [51]. More details about the history of photoemission can be found in [52].

The photoemission process is straightforward. The incident photon transfers its energy to an electron originally bound in the solid and annihilates. This electron is excited and escapes the solid into the vacuum. Due to energy conservation, we can can link the energy of the photon $h\nu$, the binding energy of the electron E_{B}, the work function of the solid ϕ, and the kinetic energy of the emitted electron E_{kin}:

$$E_{\text{kin}} = h\nu - \phi - E_{\text{B}}. \tag{3.17}$$

Knowing $h\nu$ and ϕ, the equation above provides an approach to detect the electronic structure (E_{B}) in the solid by characterizing the emission electrons.

Here I briefly go through the basic theoretical description of photoemission for the convenience of XSW introduction. In the field strength in interests, we can treat the external electromagnetic field (the photons) as a perturbation, and use Fermi's golden rule to calculate the transition rate:

$$\omega = \frac{2\pi}{\hbar}|\langle\Psi_f|\Delta|\Psi_i\rangle|^2\delta(E_f - E_i - h\nu). \tag{3.18}$$

For an electron in the electromagnetic field, in the most general form, the Hamiltonian is

$$H = \frac{1}{2m}(\vec{p} - e\vec{A}/c)^2 + V = (\frac{\vec{p}^2}{2m} + V) - \frac{e}{2mc}(\vec{A}\cdot\vec{p} + \vec{p}\cdot\vec{A}) + \frac{e^2}{2mc^2}\vec{A}\cdot\vec{A}, \tag{3.19}$$

where $\vec{A}$ and ϕ are the vector and scalar potentials of the electromagnetic field and $\vec{p}$ the momentum operator. Clearly the term, $H_0 = \frac{\vec{p}^2}{2m} + V$, is the Hamiltonian without the external electromagnetic field. The perturbation is

$$\Delta = H - H_0 = -\frac{e}{2mc}(\vec{A}\cdot\vec{p} + \vec{p}\cdot\vec{A}) + \frac{e^2}{2mc^2}\vec{A}\cdot\vec{A}. \tag{3.20}$$

Here we need to apply an approximation: We ignore the quadratic term. This non-linear term gives rise to non-linear processes, which is only relevant when a strong field is included. For the linear term, the commutation relation gives $\vec{A}\cdot\vec{p} + \vec{p}\cdot\vec{A} = 2\vec{A}\cdot\vec{p} + i\hbar(\nabla\cdot\vec{A})$. Due the transverse nature of the electromagnetic waves, the divergence of the vector potential is zero, $\nabla\cdot\vec{A} = 0$. The perturbation term is thus simplified to

$$\Delta = -\frac{e}{mc}\vec{A}\cdot\vec{p}. \tag{3.21}$$

The matrix element connecting the initial and final states ($|\Psi_i\rangle$ and $|\Psi_f\rangle$) is

$$M_{if} = -\frac{e}{mc}\langle\Psi_f|\vec{A}\cdot\vec{p}|\Psi_i\rangle. \tag{3.22}$$

According to the Fermi's golden rule (Eq. 3.18), a transition happens only when the photon energy is exactly the same as the energy difference between the initial and final electronic states. These transitions correspond to the peaks observed in the photoemission spectrum. As an example, I present in Fig. 3.4 an overview spectrum measured on hBN/Ir(111) with Cs adsorption. The dominant peaks observed are from transitions whose initial states are Ir $4f$ doublets (∼60 eV, labeled gray), B $1s$ (∼190 eV, labeled green), N $1s$ (∼400 eV, labeled blue), and Cs $3d$ doublets (∼ 740 and 725 eV, labeled red).

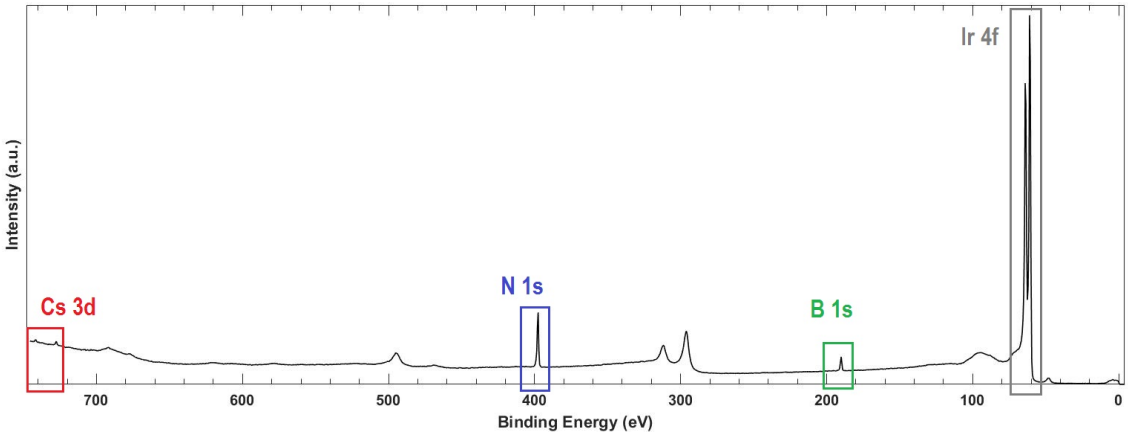

Figure 3.4: Photoemission spectrum measured on hBN/Ir(111) with Cs adsorption. $h\nu = 900$ eV.

Besides the characteristic photoemission peaks, some other features also appear in the photoemission spectrum. The two most common ones are the increasing background toward higher binding energy and the Auger peaks.

The increasing background is due to inelastic scattering. The Auger peaks originate from the Auger process: When one electron is excited, it leaves behind an unoccupied state (a hole). A second electron from a higher energy level would transit to this whole. The energy difference in this transit is transfered to a third electron. If the energy transfered to the third electron is large enough, this electron could also escape into the vacuum and get collected by the detector. One could easily distinguish Auger peaks from photoemission peaks by adjusting the incident photon energy. The kinetic energy of Auger electrons is constrained by the three energy levels involved in the process, thus independent to the photon energy. While the energy of the photoemitted electron is clearly dependent on the photon energy (Eq. 3.3). Moreover, the Auger peaks are generally broader than the photoemission peaks, since the Auger process involves three energy levels.

Due to the large binding energy, x-ray is applied to detect core levels. For the k-dispersed electronic bands, ultraviolet light beam is used. In addition to the same energy measurement of the photoelectrons as XPS, in angular resolved photoemission spectroscopy (ARPES) measurements, the emission angle of the photoelectron, hence the momentum parallel to the sample surface is also measured. Thanks to the momentum conservation, the parallel momentum of the photoelectrons is the same as when its bound in the solid. In this way the k dispersions of the binding energies, i.e. the electronic bands, are measured.

3.4 XSW

The x-ray standing wave (XSW) technique uses the x-ray diffraction on single crystals to create a standing wave field as the external field for photoemission. Tuning the standing wave field, photoemission is modulated. By analyzing such modulation, information of the surface structure can be extracted.

The basic theory of the photoemission process is introduced in the last section. In this section, we calculate the standing wave field (vector potential $\vec{A}$), and incorporate it in Eq. 3.22. Here we only focus on the normal incident situation. This is the configuration applied in my measurements and it simplifies the calculation.

The standing wave field is the interference of the incident and reflected field. Here we focus on the electric field, since the interaction with electron is due to the electric part of the electromagnetic field. For the normal incident XSW technique, the electric vector of both the incident and reflected field is perpendicular to the sample surface, and in the same (or opposite) direction. Thus the total field is

$$\vec{E} = \vec{E}_0 e^{i2\pi(\nu_0 t - \vec{K}_0 \cdot \vec{r})} + \vec{E}_H e^{i2\pi(\nu_H t - \vec{K}_H \cdot \vec{r})}. \tag{3.23}$$

The first term is the complex incident electric field, and the second term reflection. The term ν is the frequency of the wave, and $\vec{K}$ the propagation vector. We only consider elastic reflection, thus $\nu_0 = \nu_H = \nu$, and $|\vec{K_0}| = |\vec{K_H}|$.

The reflectivity R is the ratio between the square of the reflected and incident field $R = |\vec{E}_H|^2/|\vec{E}_0|^2$. A phase shift ϕ is between the incident and reflected field. In normal incidence, the electric vectors of the incident and reflected field are in the same direction. Thus the reflected field is

$$(\sqrt{R}\vec{E}_0 e^{i\phi}) e^{i2\pi(\nu t - \vec{K}_H \cdot \vec{r})} = \sqrt{R}\vec{E}_0 e^{i2\pi(\nu t - \vec{K}_H \cdot \vec{r}) + i\phi}. \tag{3.24}$$

We rewrite the total interference field as

$$\vec{E} = \vec{E}_0 e^{i2\pi(\nu t - \vec{K}_0 \cdot \vec{r})} + \sqrt{R}\vec{E}_0 e^{i2\pi(\nu t - \vec{K}_H \cdot \vec{r}) + i\phi} = \vec{E}_0 e^{i2\pi(\nu t - \vec{K}_0 \cdot \vec{r})}(1 + \sqrt{R} e^{i(\phi - 2\pi \vec{H} \cdot \vec{r})}). \tag{3.25}$$

Here I put in the difference between the propogation vectors $\vec{H} = \vec{K}_H - \vec{K_0}$, which is also normal to the surface. Therefore, the intensity of the interference field is

$$I = |\vec{E}|^2 = |\vec{E}_0|^2 |1 + \sqrt{R} e^{i(\phi - 2\phi \vec{H} \cdot \vec{r})}|^2 = |\vec{E}_0|^2 [1 + 2\sqrt{R} + \sqrt{R}\cos(\phi - 2\pi \vec{H} \cdot \vec{r})]. \tag{3.26}$$

We can see in this equation the intensity of this interference field is periodic in the direction normal to the sample surface. In the measurement, we choose the photon energy $h\nu$, so that the periodicity $d_H = 1/|\vec{H}|$ of the interference field matches with the lattice plane spacing of the single crystal substrate d. Since $|\vec{K_0}| = |\vec{K_H}|$ and both normal to the surface, we have $\vec{H} = \vec{K_H} - \vec{K_0} = -2\vec{K_0}$. Thus we can link the wavelength of the photon with the crystal lattice plane spacing:

$$d = d_H = \frac{1}{|\vec{H}|} = \frac{1}{2|\vec{K_0}|} = \frac{\lambda}{2}. \tag{3.27}$$

This is the Bragg condition for (002) x-ray diffraction. From Eq. 3.27, we can calculate the photon energy we need to create such a standing wave field:

$$E_\mathrm{b} = \frac{hc}{\lambda} = \frac{hc}{2d}. \tag{3.28}$$

Till this point, I demonstrate that we can create a standing wave field on the sample surface with the interference of incident beam and reflected beam, whose intensity is constant parallel to the sample surface but changes periodically normal to the surface. Now we consider an adsorbed atom on the surface. With such standing-wave field as external excitation, the photoemission intensity strongly depends on the distance of the adsorbate to the surface, i.e. the adsorption height. The atoms adsorb at the height of the nodes of the standing wave field have the weakest excitation, thus emit the least photoelectrons. While the atoms sitting at the antinodes have the strongest photoemission effect.

Now we can combine the external standing wave field for excitation (Eq. 3.25) and the photoemission transition matrix element (Eq. 3.22), and calculate the photoemission intensity. We firstly decompose the vector $\vec{r}$ into $\vec{R}$ and $\vec{r}_{\mathrm{e}}$. They are related as $\vec{r} = \vec{R} + \vec{r}_{\mathrm{e}}$, where $\vec{R}$ is the position of the nucleus the electron is bound to, and $\vec{r}_{\mathrm{e}}$ the position of the electron relative to the nucleus. Inserting it into Eq. 3.25, we obtain

$$\vec{E} = \vec{E}_0 e^{i2\pi(\nu t - \vec{K}_0\cdot\vec{R})} e^{-i2\pi\vec{K}_0\cdot\vec{r}_{\mathrm{e}}}(1 + \sqrt{R}e^{i(\phi - 2\pi\vec{H}\cdot\vec{R})}e^{-i2\pi\vec{H}\cdot\vec{r}_{\mathrm{e}}}). \tag{3.29}$$

In the dipole approximation, we take the exponential term $e^{-i2\pi\vec{K}_0\cdot\vec{r}_{\mathrm{e}}}$ and $e^{-i2\pi\vec{H}\cdot\vec{r}_{\mathrm{e}}}$ as 1. This approximation is justified when $\vec{K}_0 \cdot \vec{r}_{\mathrm{e}} \ll 1$ and $\vec{H} \cdot \vec{r}_{\mathrm{e}} \ll 1$, meaning the electron-nucleus distance is much smaller than the wave length of the photon. This criteria holds true for the electronic orbitals in interests in this study. For electrons in shallow orbitals, we can apply the non-dipole correction. It is applied to all XSW analysis in this study, and the results do not change within resolution. For details of non-dipole correction, readers can refer to literature [**?**]. With dipole approximation, the electric field is simplified to

$$\vec{E} = \vec{E}_0 e^{i2\pi\nu t} e^{-i2\pi\vec{K}_0\cdot\vec{R}}(1 + \sqrt{R}e^{i(\phi - 2\pi\vec{H}\cdot\vec{R})}), \tag{3.30}$$

which is no longer a function of position of the electron relative to the nucleus, but only of $\vec{R}$, the position of the nucleus. Thus we can move the electric field term out of the integral in Eq. 3.22:

$$M_{if} = -\frac{e}{mc}\vec{A}\cdot\langle\Psi_f|\vec{p}|\Psi_i\rangle. \tag{3.31}$$

With the dipole approximation, we have separated the external electric field with the electronic structure in the solid.

According to Fermi's golden rule, the transition rate is proportional to $|M_{if}|^2$, thus the photoemission yield is proportional to $|\vec{A}|^2$, thus $|\vec{E}|^2$:

$$Y \propto |\vec{A}|^2 \propto |\vec{E}|^2 \propto |1 + \sqrt{R}e^{i(\phi - 2\pi\vec{H}\cdot\vec{R})}|^2 = 1 + R + 2\sqrt{R}\cos(\phi - 2\pi\vec{H}\cdot\vec{R}). \tag{3.32}$$

Hence, the normalized intensity for an atom at $\vec{R}$ can be expressed as:

$$I = 1 + R + 2\sqrt{R}\cos(\phi - 2\pi\vec{H}\cdot\vec{R}). \tag{3.33}$$

In practice, the measurement detects a certain area, including many adsorbed atoms of one certain species. The total intensity is the sum over all these contributing atoms:

$$I = \sum_j^N I_j = N(1 + R) + 2\sqrt{R}\sum_j^N \cos(\phi - 2\pi\vec{H}\cdot\vec{R}_j), \tag{3.34}$$

where the index j indicates the jth atom. Since we modulate the incident beam and detect the change it creates in the intensity, we treat the intensity I as a function of the external field ($\vec{H}$). It is clear that the summation over all cosine functions yields again a cosine function. However $\vec{R}_j$ could vary for different atoms (different adsorption configuration). The resulting cosine function has a reduced amplitude f^H and an averaged phase P^H, i.e.

$$I = N[1 + R + 2\sqrt{R}f^H cos(\phi - 2\pi p^H)]. \tag{3.35}$$

Since $\vec{H}$ is perpendicular to the sample surface, and $|\vec{H}| = 1/d$, the phase $\vec{H} \cdot \vec{R}$ is then the height of the adsorbed atom at position $\vec{R}$ normalized to the crystal plane spacing d. Thus P^H, the coherent position, is the "average" height of the adsorbed atoms normalized to the crystal plane spacing d. The coherent fraction f^H is a measure of height distribution of all the adsorbed atoms. For example, if all the atoms sit at the same height, then $\vec{H} \cdot \vec{R}_j$ would give the same phase for every j, and f^H would be 1.

In practice, we modulate the energy of the incident light beam around the Bragg energy, thus changing $\vec{H}$, and monitor the change in the intensity. This I-$|\vec{H}|$ dependence allow us to fit the data against Eq. 3.35, and obtain the coherent position P^H and coherent fraction f^H, thus obtaining information about the structure of the adsorbed atoms.

It should be noticed that for two adsorbed atoms whose adsorption height difference is exact $n \cdot d$ (n being an integer), they are effectively at equal positions in the standing wave field, thus their photoemission yield is the same. This means the actual adsorption height could miss the P^H by some periods of standing wave field:

$$h = d \times (n + P^H), \tag{3.36}$$

n being any integer, which clearly adds some uncertainty to the structural analysis.

3.5 Setups

Three set-ups were involved in this study, the CVD/PVD machine, VT-STM, and the I09 beamline of Diamond Light Source. However, this chapter does not include a section for the home-built CVD/PVD machine, since this thesis does not contain data obtained from it. This machine is designed by the author and is dedicated to fast and convenient sample preparation.

For the preparation of the sample, the epitaxial growth of 2DMs requires a clean TM surface. The characterization of the samples is very surface sensitive. Hence the sample preparations and measurements are conducted in ultra high vacuum (UHV) environment in all three setups.

3.5.1 VT-STM

For STM measurement, a Scienta Omicron variable temperature STM (VT-STM) system is used. This system includes four UHV chambers: preparation chamber, STM chamber, deposition chamber, and fast entry lock (FEL) chamber (Fig. 3.5). The preparation chamber and STM chamber are directly connected, and the base pressure is 1×10^{-10} mbar. Between preparation chamber and FEL, between preparation chamber and deposition chamber, two manual gate valves are mounted to

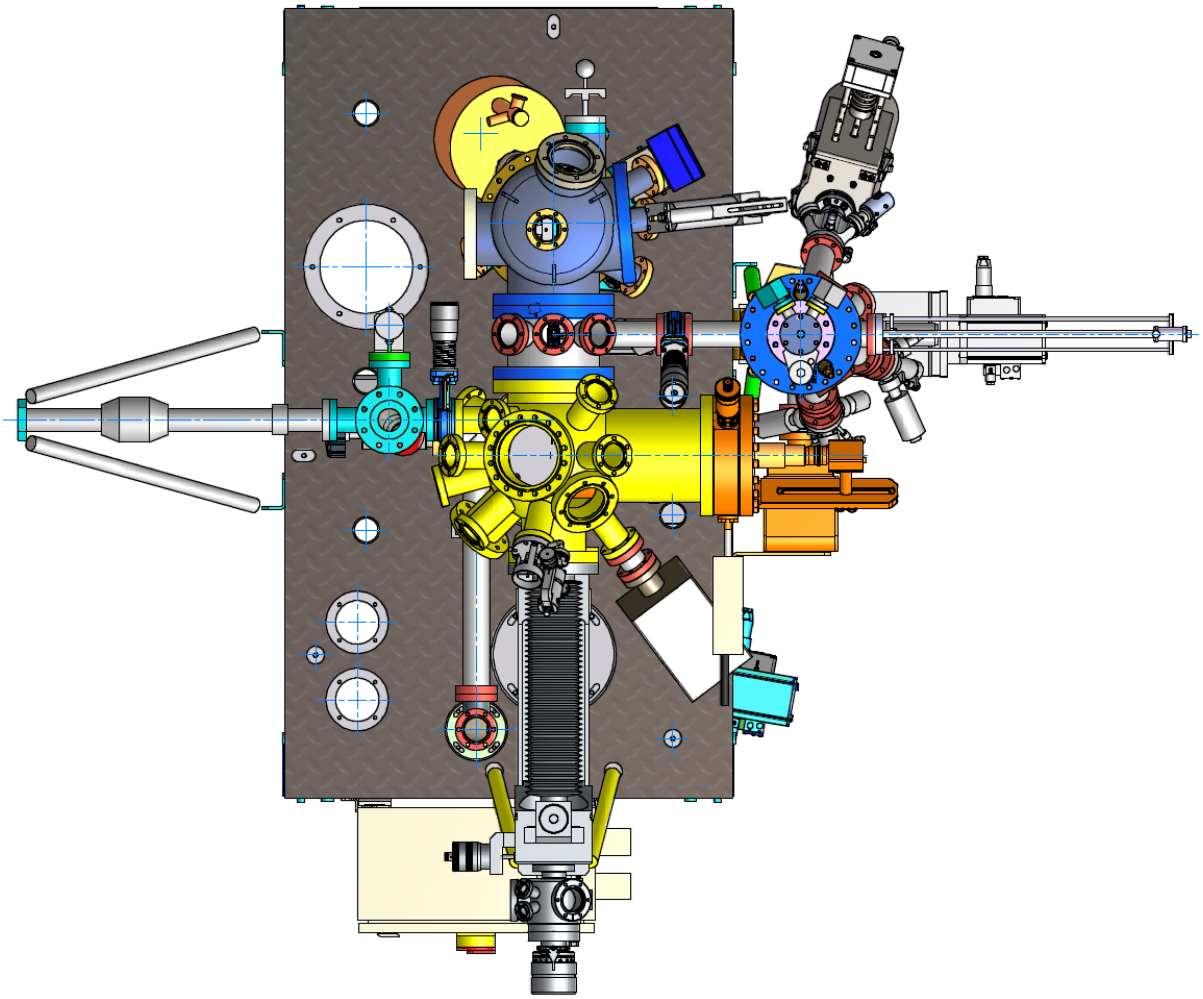

Figure 3.5: Isometric drawing of VT-STM set-up.

control the connection among these three chambers. The sample preparation and measurements in this study do not involve the deposition chamber (7×10^{-10} mbar).

The preparation chamber is equipped with: (i) a sputtering gun for sample cleaning, (ii) a LEED device for structural characterization of the sample surface, (iii) gas inlets for the growth of hBN and graphene, (iv) a four-axes manipulator with an electron beam heating stage for the sample, (v) a pyrometer for the remote temperature measurement of the sample.

A home-built alkali metal evaporator is mounted on the preparation chamber for alkali metal deposition. The evaporator is loaded with three dispensers (Li, K, Cs, SAES). A direct current is applied through the selected dispensers to deposit the selected alkali metal. The same evaporator is also used in the Diamond Light Source for PE measurements.

3.5.2 Diamond I09 beamline

The XPS and XSW measurements in this study are conducted in the I09 beamline at Diamond Light Source, United Kingdom. This beamline is designed for high-resolution studies of atomic and electronic structures of surfaces and interfaces. To apply both XPS and XSW techniques, two canted undulators are used to provide both soft (100 - 2100 eV) and (2.1 - 20 keV) hard x-rays.

In the end station (Fig. 3.6, pressure $< 2 \times 10^{-10}$ mbar), the x-ray beam is led into the analysis chamber and illuminates the sample. A VG Scienta EW4000 hemispherical HAXPES electron analyzer is equipped perpendicular to the incident beam. This analyzer is accompanied with a 17 frame/sec CCD camera having a 56° acceptance angle. The sample docks on a 5-axes manipulator. For XSW measurements, the sample is placed normal to the incident x-ray beam, with the analyzer at a grazing angle. For XPS measurements, the sample is rotated to two polar angles to fulfill the emission-angle dependence measurements in Sec. 6.3 and Chap. 7.

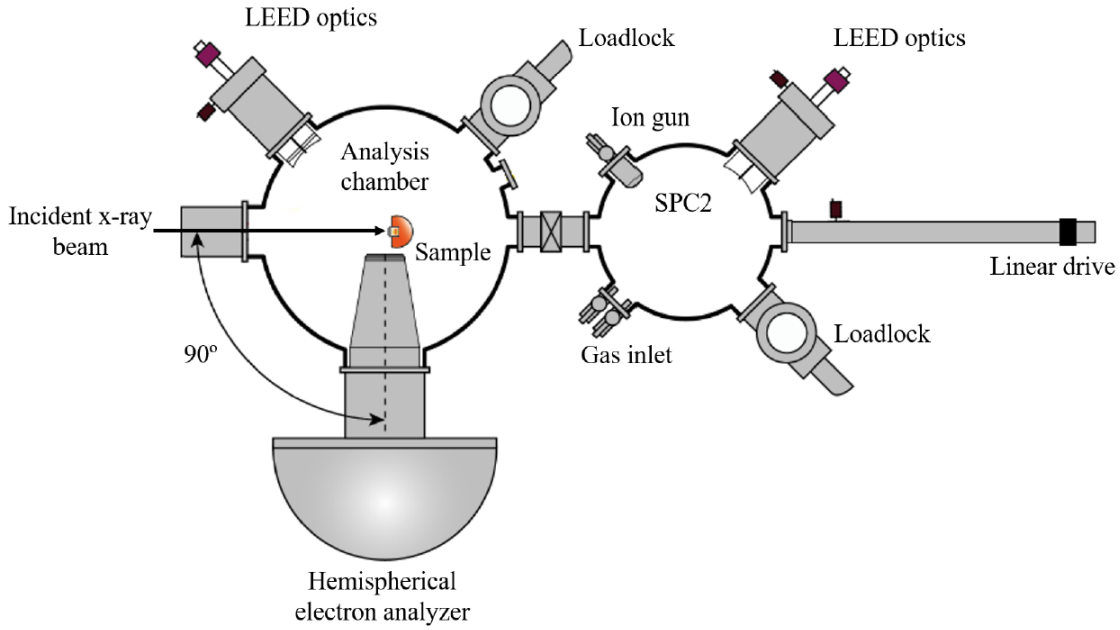

Figure 3.6: Schematic drawing of the main end-station of I09 beamline.

Apart from the analysis chamber, two UHV chambers (SPC1 and SPC2) are connected to the analysis chamber by gate valves for sample preparation. The data presented in this thesis only involves the usage of SPC2. The sample is transfered between SPC2 and the analysis chamber by a linear translator. SPC2 is equipped with the similar devices as the analysis chamber of VT-STM (Sec. 3.5.1) for sample cleaning and preparation. This includes an electron beam heating stage, a sputtering gun, a LEED, a pyrometer for sample temperature measurement and gas inlets. The alkali metal evaporator is also mounted on SPC2.

Chapter 4

Pristine epitaxial hBN/TM systems

In this chapter, I start with the discussion of the growth of hBN on Ru(0001) and Ir(111) (Sec. 4.1). Two epitaxial growth approaches are included: chemical vapor deposition (CVD) for full layer growth, and temperature programmed growth (TPG) for sub-monolayer growth.

The high quality samples with full coverage (hBN/Ir(111) and hBN/Pt(111)) discussed in Sec. 4.1 are characterized with XPS and XSW measurements. I focus on the corrugation geometry of the hBN layer. The measurement results and analysis are discussed in Sec. 4.2.

In Sec. 4.3, I briefly discuss the sequential growth of hBN and graphene on Ru(0001) and Ir(111). I focus on the influence of the in-plane epitaxy between the two 2DMs on the alignment of the 2DMs to the substrates.

4.1 Epitaxial growth of hBN/Ru(0001) and hBN/Ir(111)

High-quality 2DM can be grown by epitaxial methods on the high-symmetry surfaces of TMs. The first epitaxial growth method I apply is CVD: the TM substrate is heated to high temperature in the atmosphere of the precursor. For hBN growth, the aromatic compound, borazine ($B_3N_3H_6$), is used as the precursor. The six-atom ring structure of the borazine molecule is presented in Fig. 4.1a.

The CVD process includes three steps: (i) the adsorption of borazine on TM surface. (ii) the decomposition of the borazine molecules. (iii) the diffusion and aggregation of the radicals, forming a continuous layer of hBN sheet. These three steps in the CVD process are illustrated in Fig. 4.1b. For the whole process, the TM substrate is kept at high temperature (Fig. 4.1c), which facilitates the dehydrogenation of the borazine molecules. Once the substrate surface is fully covered with hBN, the borazine precursor is separated from the TM surface, effectively terminating the dehydrogenation, thus preventing the growth of the second layer.

In step (iii), the molecular fragment migrates on the surface. When it encounters the edge of a hBN flake, it connects to the flake, in various possible configurations. The most energetically favored aggregation configuration leads to the continuous and ordered growth of the hBN sheet. Here the high temperature plays a vital role, selecting the best agglomeration configuration. With relatively low temperature, other agglomeration configurations occur, rendering various defects in the hBN layer.

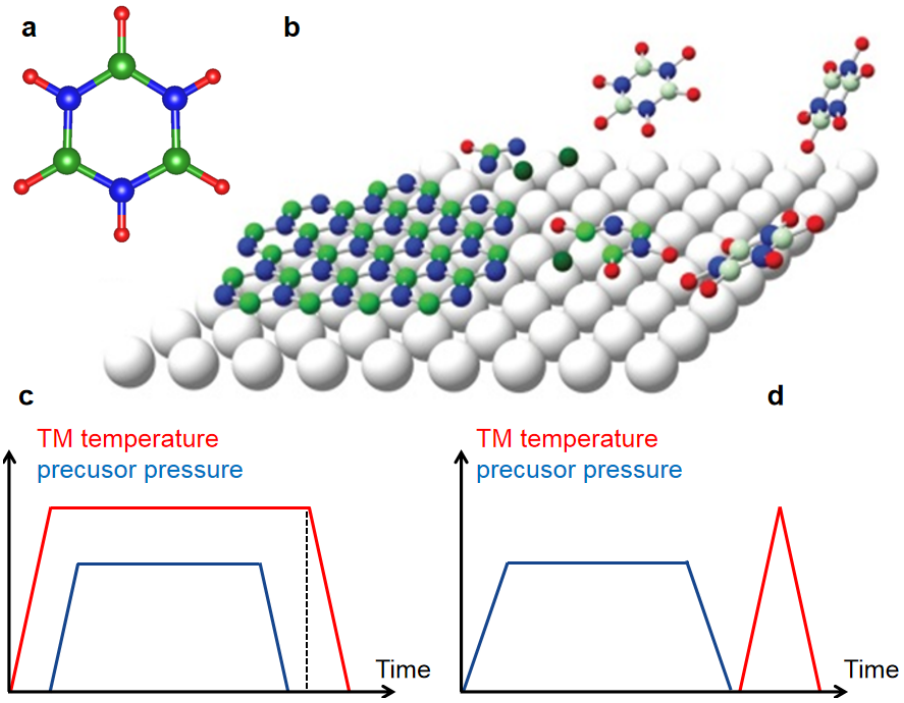

Figure 4.1: (a) Atomic structure of borazine ($B_3N_3H_6$). (b) Schematic illustration of the CVD process, modified from Ref. [53]. The chronological relation of the temperature and precursor pressure regulation in (c) the CVD process, and (d) the TPG process.

As an example, Fig. 4.2a and b present the STM images of the Ru(0001) surface after 20 minutes of 800 °C CVD growth. The obvious periodic network structure is the moiré pattern between the hBN layer and the Ru(0001) substrate. The periodic distance between the dark regions of the network is approximately 2.5 nm. It is in good agreement with the previously reported value [54]. As described in Sec. 2.2.2, the dark areas in the STM images are the valley regions of the moiré unit cell. In the valley regions, the hBN layer is closer to the Ru(0001) substrate, and the hBN-substrate interaction is strong. In contrast, the continuous bright areas in the STM images are the hill regions, where the hBN-Ru(0001) distance is large and the interaction weak.

One inevitably notices that the moiré pattern of the 800 °C-CVD sample is not perfectly periodic. A lot of defects are present in the STM images. Some are individual enlarged and misshaped dark regions. Some are connected dark regions without bright regions in between. It is worth mentioning that most of the defects appear as extra dark areas (valleys). The extra valley regions originate from the less preferred agglomeration configurations in the previously mentioned step (iii) of the CVD process: the energy loss in breaking the continuous hBN lattice is partially paid off by the extra hBN-Ru(0001) binding in the extra valley regions.

When I increase the CVD temperature, the density of the defects decreases. Fig. 4.2c and d present the STM images of the Ru(0001) surface after 20 minutes of 950 °C CVD growth. Despite the occasional extra dark regions, the degree of ordering is much higher than on the 800 °C CVD grown sample. To achieve a convincing comparison, the borazine pressure is both kept at 1×10^{-7}

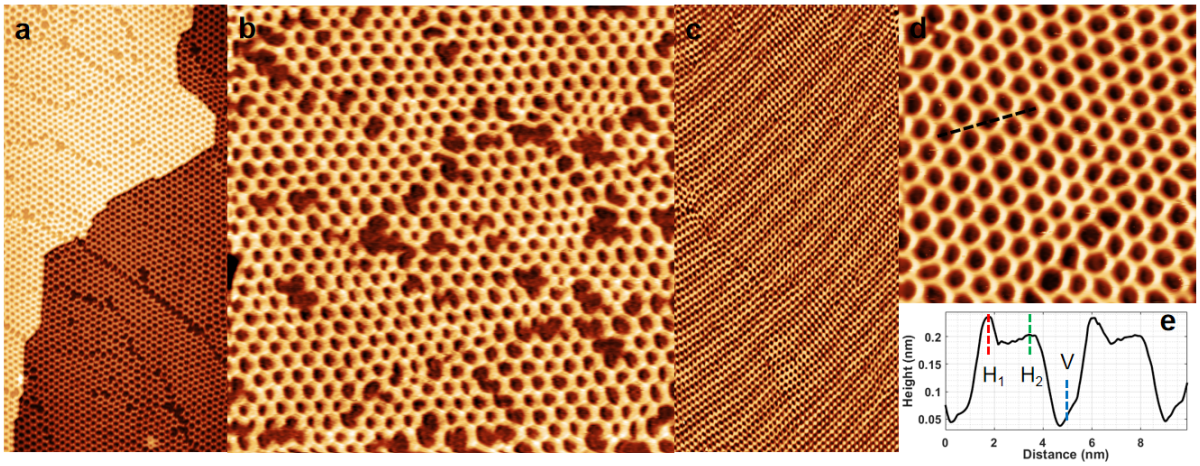

Figure 4.2: STM images of hBN/Ru(0001) prepared by CVD method. (a) 800 °C-CVD sample, $U_b = -1.0$ V, $I_{tunneling} = 100$ pA, 250×125 nm^2. (b) 800 °C-CVD sample, $U_b = -1.5$ V, $I_{tunneling} = 100$ pA, 100×100 nm^2. (c) 950 °C-CVD sample, $U_b = -1.5$ V, $I_{tunneling} = 100$ pA, 200×100 nm^2. (d) 950 °C-CVD sample, $U_b = -2.4$ V, $I_{tunneling} = 20$ pA, 40×40 nm^2. (e) Apparent height along the dashed line in Fig. 4.2d.

mbar for both 800 °C and 950 °C CVD growth.

Fig. 4.2e presents the apparent height along the dashed line in Fig. 4.2d. The dashed line crosses some hill regions (indicated by the red and green dashed lines) and valley regions (indicated by the blue dashed line). The corrugation of the apparent height is approximately 2 Å. I also notice a slight difference in the apparent height in the two kinds of hill regions (H_1 and H_2 in Fig. 4.2e) originating from the different adsorption geometries (Sec. 2.2.2).

Fig. 4.3a presents the STM image of the 950 °C-CVD grown hBN/Ru(0001) with atomic resolution. The direction of the atomic rows is indicated by the blue dashed lines. The direction of the moiré is indicated by the green dashed lines. There is a small angle between the two directions. This angle originates from the local misalignment between the atomic lattice of the hBN layer and the Ru(0001) substrate.

The Fourier transformation (FT) of Fig. 4.3a is presented in Fig. 4.3b. The bright spot in the white circle originates from the atomic lattice of hBN in the reciprocal space. The satellite spots surrounding it originate from the moiré pattern. The vertical lines are artifacts possibly from external noise. Here I can also observe the misalignment between the moiré pattern and the hBN atomic lattice (blue and green dashed lines). However, the LEED pattern obtained on this very sample (Fig. 4.3c) reveals a good alignment between the hBN layer and Ru(0001) substrate: the dashed line goes across all the hBN spots and moiré satellite spots.

Combining the macroscopic characterization by LEED and the microscopic characterization by STM, 950 °C-CVD growth yields overall aligned hBN on Ru(0001). Yet in some areas of the sample, there are some rotational hBN domains with small misalignment angle. This local misalignment is testified by the line defects in the large-scale STM images (Fig. 4.2c and d). This tendency to yield microscopic misaligned domains indicates a rather weak interaction between hBN and the Ru(0001)

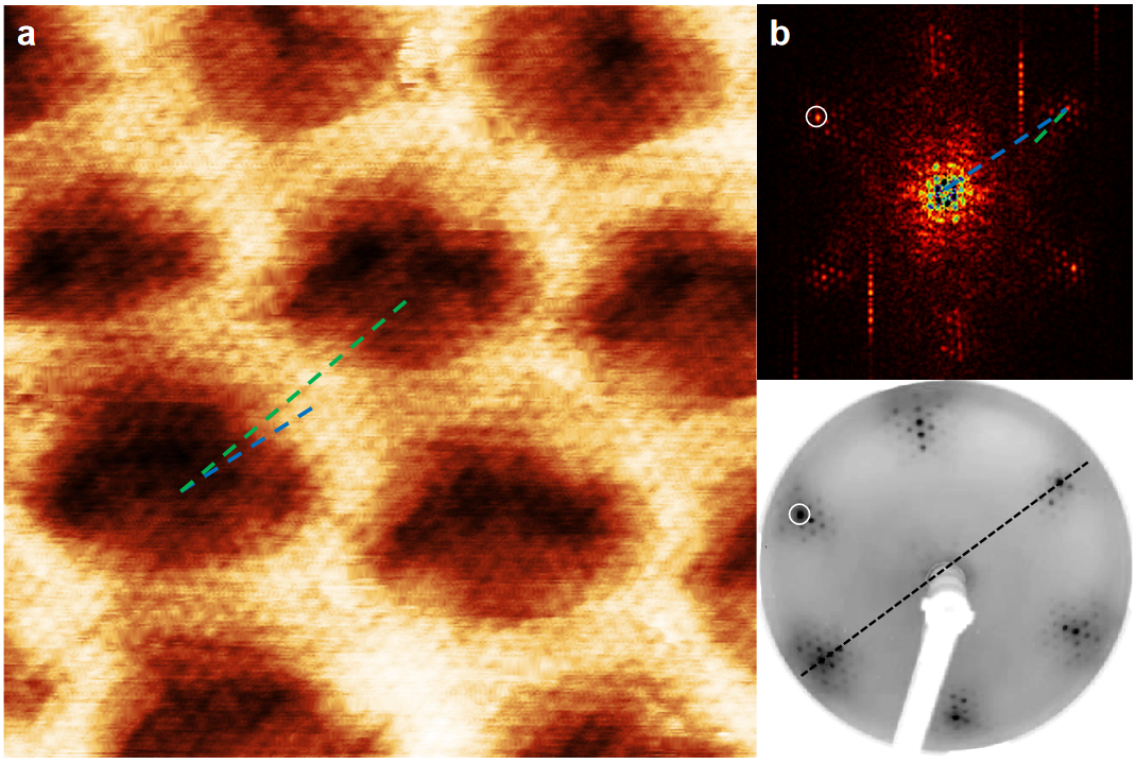

Figure 4.3: (a) Atomically resolved STM image of hBN/Ru(0001). 10×10 nm^2, $U_b = 1.0$ mV, $I_{tunneling} = 3.0$ nA. (b) FT of (a). (c) LEED image measured on the 950 °C-CVD sample. The blue and green dashed lines in (a) and (b) indicate the directions of the atomic lattice and the moiré pattern. The black line in (c) goes across the (10) and $(\bar{1}0)$ spots of hBN reciprocal lattice.

substrate. The growth of hBN/Ru(0001) with higher quality has been reported [55]: a lower borazine pressure is required, which results in a very long growth time (over 100 minutes) to achieve full layer coverage.

As comparison, I also study the preparation of hBN/Ir(111). The growth of the epitaxial hBN layer with good alignment to the Ir(111) substrate is much easier than on Ru(0001).

Fig. 4.4a presents a large scale STM image on Ir(111) after 20 minutes of 930 °C-CVD growth, I observe periodic arrays of bright protrusions. The distance between the neighboring bright protrusions is approximately 3.0 nm, which agrees with previously reported moiré periodicity [23]. The very high degree of ordering observed on hBN/Ir(111) is a sharp contrast to the relatively high density of defects present on hBN/Ru(0001) (Fig. 4.2). The borazine pressure used to prepare both samples are the same (1×10^{-7} mbar), and the substrate temperature is even slightly lower for hBN/Ir(111).

The inset of Fig. 4.4a presents the LEED pattern measured on hBN/Ir(111). A very pronounced moiré pattern with good alignment is present. Fig. 4.4b presents one STM image with atomic resolution. The red dashed line in the image indicates the direction of the atomic rows. The green dashed line indicates the direction of the moiré superlattice. They are parallel to each other, indicating the good alignment between the hBN layer and the Ir(111) substrate.

Another route for epitaxial growth of hBN on TM surface is temperature programmed growth.

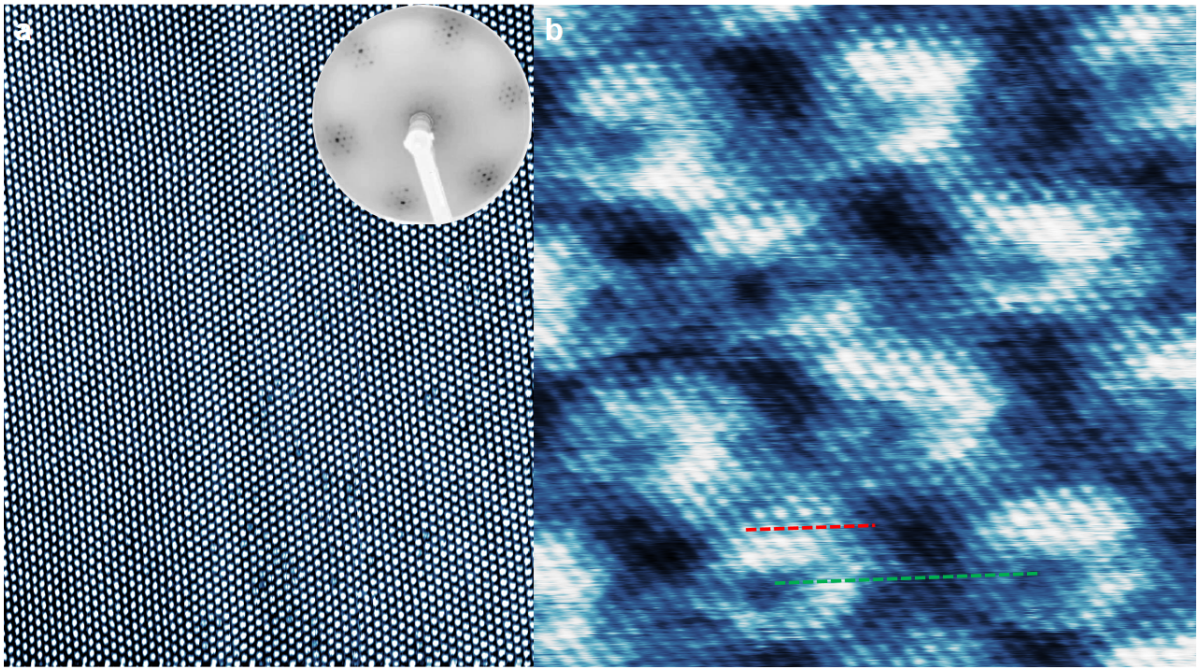

Figure 4.4: STM images of hBN/Ir(111). (a) 200×150 nm^2, $U_\mathrm{b} = 2.4$ V, $I_\mathrm{tunneling} = 80$ pA. Same as Fig. 2.4. (b) 8×8 nm^2, $U_\mathrm{b} = 7.2$ mV, $I_\mathrm{tunneling} = 3.1$ nA.

In this method, the TM substrate is first exposed to the precursor at room temperature (or even lower temperature). After saturated adsorption, it is quickly heated to high temperature. Fig. 4.1d illustrates the chronological relation between the precursor dosage and the application of high temperature in the TPG process. For graphene growth on Ir(111), TPG method proves to be an easier approach to produce a high-quality graphene layer than the CVD method [56].

One cycle of TPG growth normally yields sub-monolayer coverage of the 2DMs. This is mainly due to the larger size of the precursor molecules than the dehydrogenated radicals. For example, one TPG cycle with ethylene results in an approximately 22% areal coverage of graphene on Ir(111) [56].

In Fig. 4.5, I present the STM images of the Ru(0001) surface after one TPG cycle. Two different temperatures were applied in the heating step, 630 °C (Fig. 4.5a) and 1000 °C (Fig. 4.5b and c). On both samples, hBN forms islands. In Fig. 4.5a, there exist networks of bright areas on the hBN islands, separating dark regions. Due to the small size of the islands (less than 10 nm), the bright networks are not extended. On the 1000 °C-TPG sample, the islands are quite large. In the zoom-in image (Fig. 4.5c), I can observe the extended moiré pattern on the hBN islands. The areal coverage of both 630 °C- and 1000 °C-TPG samples is approximately 60%.

For comparison, I also prepare hBN on Ir(111) by TPG method. Fig. 4.6 presents the STM images of Ir(111) surface after one TPG cycle with different heating temperature (730 °C Fig. 4.6a, 930 °C Fig. 4.6b, 1030 °C Fig. 4.6c). The morphology of the sub-monolayer hBN is very different from that on Ru(0001). On Ir(111), hBN forms percolated networks. With increasing TPG temperature, the degree of ordering of the resulting hBN layer gradually increases. On the 730 °C-TPG sample (Fig. 4.6a), on can hardly observe the ordered moiré pattern. The hBN layer forms disordered and

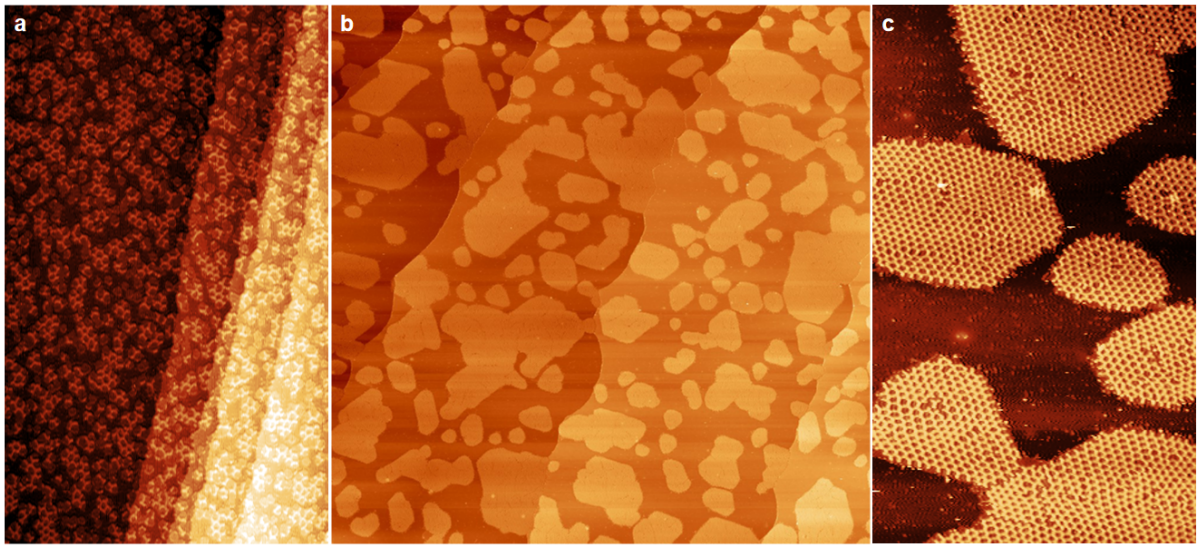

Figure 4.5: STM images of TPG grown sub-monolayer hBN/Ru(0001). (a) TPG temperature 630 °C, 250×150 nm^2, $U_\mathrm{b} = -1.0$ V, $I_\mathrm{tunneling} = 100$ pA. (b) TPG temperature 1000 °C, 1200×1200 nm^2, $U_\mathrm{b} = -2.4$ V, $I_\mathrm{tunneling} = 20$ pA. (c) TPG temperature 1000 °C, 200×120 nm^2, $U_\mathrm{b} = -2.4$ V, $I_\mathrm{tunneling} = 20$ pA.

interconnecting wires, leaving a lot of small holes, i.e. uncovered areas of bare Ir(111). On the 1030 °C-TPG sample (Fig. 4.6c), the number of the holes decreases, while their sizes increase. The degree of ordering in the hBN/Ir(111) area significantly increases with elevated TPG temperature: The moiré pattern is visible. This observed evolution of the hBN/Ir(111) morphology is in agreement with the previous STM investigation [26].

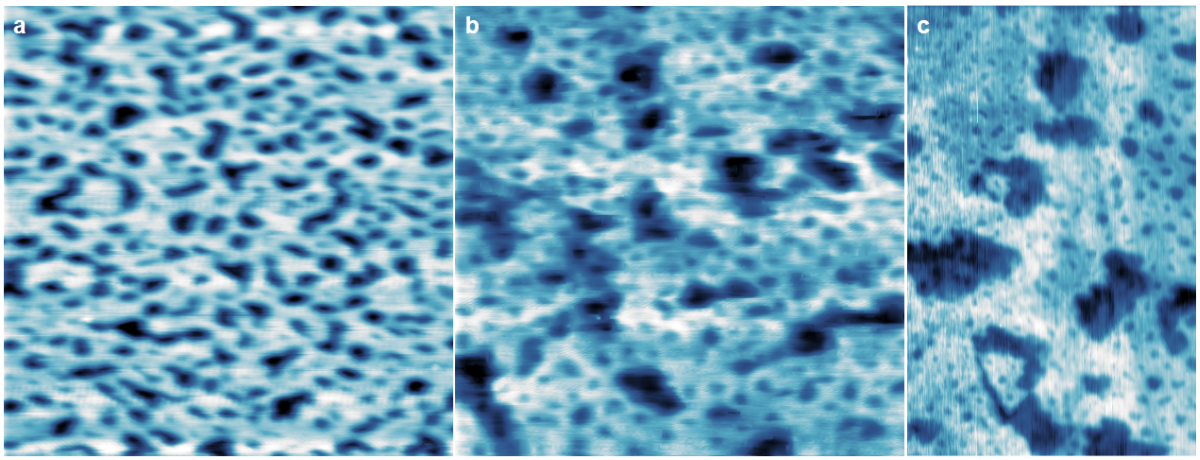

Figure 4.6: STM images of TPG grown sub-monolayer hBN/Ir(111). (a) TPG temperature 730 °C, 40×40 nm^2, $U_\mathrm{b} = -1.8$ V, $I_\mathrm{tunneling} = 250$ pA. (b) TPG temperature 930 °C, 50×50 nm^2, $U_\mathrm{b} = 2.0$ V, $I_\mathrm{tunneling} = 400$ pA. (c) TPG temperature 1030 °C, 70×45 nm^2, $U_\mathrm{b} = -1.8$ V, $I_\mathrm{tunneling} = 600$ pA.

Comparing hBN/Ru(0001) and hBN/Ir(111) by TPG preparation, one notices the difference of their sub-monolayer morphology. HBN grows into discrete islands on Ru(0001). On Ir(111), it forms a percolated network, same as the morphology reported in Ref. [26]. The critical difference between the two morphologies is the length of the edges. The island morphology has much shorter edges than the network morphology, i.e. less N/B atoms in the hBN layer bond to the TM substrate. Thus the difference in the sub-monolayer morphology indicates that the binding energy of the hBN edge is larger on Ir(111) than on Ru(0001).

It is worth mentioning that the areal coverage of hBN/Ir(111) after one TPG cycle is also 60 % [26]. Assuming no loss of N/B atoms in the TPG process, the similar areal coverage suggests a similar adsorption structure of borazine on Ru(0001) and Ir(111). However, previous photoemission study [53] suggests a planar adsorption geometry of borazine on Ir(111). Vibrational spectroscopy measurements [57, 58] indicates that the borazine molecule partly dehydrogenates and adsorbs on Ru(0001) with the six-atom ring vertical to the substrate. The disagreement between my observation and the literature demands further study of the adsorption geometry of borazine molecules on Ru(0001) and Ir(111). Yet it is not within the scope of this thesis.

4.2 PE characterization of hBN/Pt(111) and hBN/Ir(111)

In the last section, I described the LEED and STM study of the epitaxial growth of hBN on two different TM substrates, Pt(111) and Ir(111). I establish the important role played by the hBN-TM interaction in the growth process. This interaction is mainly electronic. In this section, I discuss my investigation with PE measurements (XPS and XSW) to explore the electronic properties of hBN/Pt(111) and hBN/Ir(111).

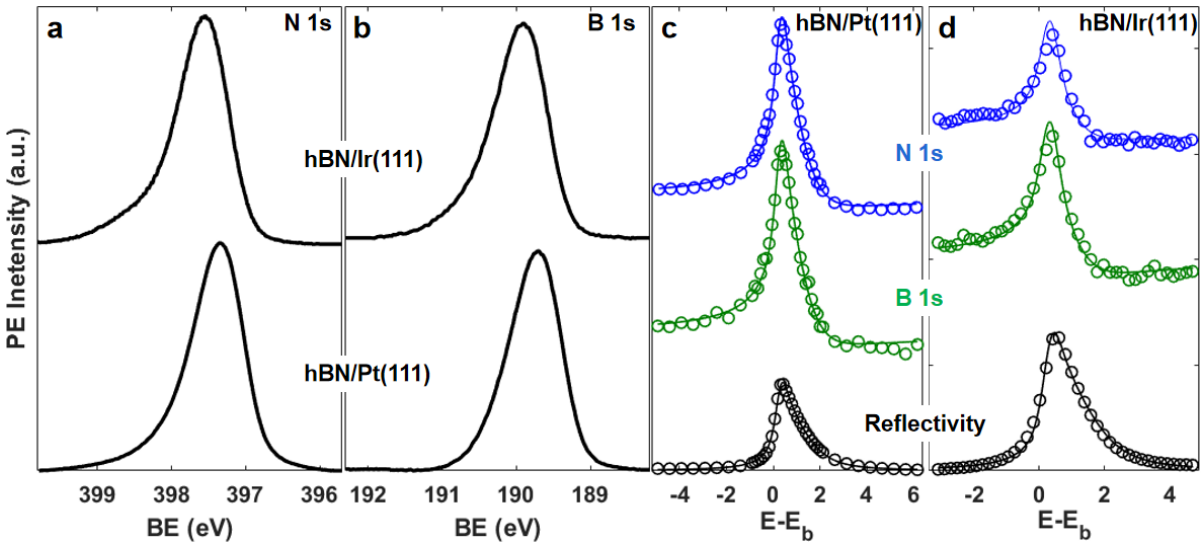

Figure 4.7: (a) N 1s spectra measured on hBN/Pt(111) and hBN/Ir(111) with 600 eV photon energy. (b) B 1s spectra measured on hBN/Pt(111) and hBN/Ir(111) with 400 eV photon energy. XSW data (circles) and fitting lines on (c) hBN/Pt(111) and (d) hBN/Ir(111). N 1s (blue), B 1s (green).

Fig. 4.7a presents the N 1s spectra measured on hBN/Pt(111) and hBN/Ir(111). Comparing between both samples, the position of the peak is higher in BE on hBN/Ir(111). The width of the peak is slightly larger. The same features are also observed in the B 1s spectra. The positions and widths of the N 1s and B 1s peaks are listed in Tab. 4.1.

		Position	FWHM	P^H	f^H
hBN/Ir(111)	N 1s	397.55	0.82	0.78	0.30
	B 1s	189.91	0.85	0.74	0.30
hBN/Pt(111)	N 1s	397.35	0.81	0.50	0.48
	B 1s	189.72	0.84	0.51	0.53

Table 4.1: Parameters obtained from XPS and XSW measurements on hBN/Ir(111) and hBN/Pt(111): position and width of N 1s and B 1s peaks, coherent position and coherent fraction.

I conduct XSW measurements for the N 1s and B 1s signals on the two samples: the intensities of the peaks are monitored when modulating the photon energy around Bragg energy (E_b). The measurement results are displayed in Fig. 4.7c and d (circles). Eq. 3.36 is used to fit the measured intensity-energy dependence (lines in Fig. 4.7c and d) as described by Vartanyants *et al.* to yield the coherent position P^H and coherent fraction f^H [59]. The optimized P^H and f^H are listed in Tab. 4.1. The measurement results on hBN/Ir(111) agrees with the results reported in Ref. [26].

The coherent fraction f^H is a measure of the height distribution of the measured elemental species. A value of 1 indicates a uniform adsorption height for all the atoms. The larger f^H measured on hBN/Pt(111) than on hBN/Ir(111) reveals that the hBN layer is flatter on Pt(111) than on Ir(111).

Ref. [55] reported a NEXAFS study which reveals a very flat hBN layer on Pt(111). For hBN/Ir(111), the N 1s (B 1s) peak can be decomposed into two components originating from the valleys and hills in the moiré pattern. XSW analysis is then made for both components and reveals the adsorption height of 3.72 Å for the hills and 2.20 Å for the valleys (for details, see Ref. [26]). These reported corrugation geometry of hBN sheet on Ir(11) and Pt(111) agrees with my conclusion based on the f^H values.

The same double-components analysis is applied on the PE data of hBN/Pt(111). The resulting coherent positions for the two components turn out to be very similar (e.g. N 1s: 0.50 and 0.53), which again suggests the flatness of the hBN layer. Using Eq. 3.36, I obtain the average adsorption height of hBN on Pt(111) is 3.41 Å. My conclusion of the flatness of the hBN layer on Pt(111) contradicts the 2.0 Å corrugation of the apparent height by the STM measurements (Fig. 4.2e). Since height regulation in STM measurements is sensitive to the local density of states. I attribute the large corrugation appearing in the apparent height to the electronic effect, rather than the actual geometric corrugation.

4.3 In-plane hetero-structure: 2d epitaxy

In this section, I briefly discuss the sequential growth of hBN and graphene on TM surfaces to form an in-plane hetero-structure, hBN-gr. The isostructure of graphene and hBN, and the very small lattice mismatch enables them to form a continuous sheet. In this thesis, I do not discuss the continuous atomic lattice across hBN and graphene, but rather the influence of the existing hBN flakes on the growth of graphene.

In Sec. 4.1, I demonstrated that the 2DM-substrate interaction has a strong effect on the quality of the 2DM. Epitaxial systems with weak 2DM-substrate interaction are prone to have rotational domains of the 2DM. DFT calculation reveals a very weak interaction between graphene and Ru(0001) [60]. The growth of an extended and aligned graphene layer on Ru(0001) has proven to be very difficult. To the best of my knowledge, no report of a successful growth has been reported so far. LEED and STM measurements reveal, besides the aligned domains of graphene on Ru(0001), the 19° and 30° rotational domains are also very easy to form [60].

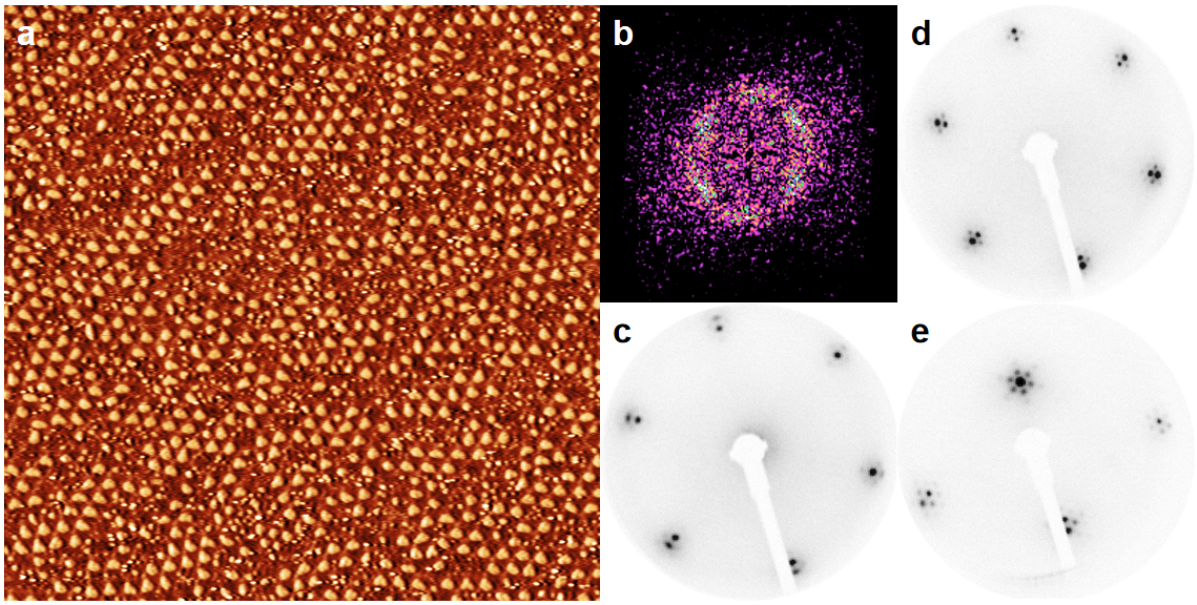

Figure 4.8: (a) STM image of gr/Ru(0001), 100×100 nm^2, $U_\mathrm{b} = 1.0$ V, $I_\mathrm{tunneling} = 200$ pA. (b) FT of Fig. 4.8a. (c) LEED pattern measured on gr/Ru(0001). (d) and (e) LEED patterns measured on hBN-gr/Ru(0001). In (e), the sample is rotated to move the zeroth order spots off the shadow of the electron gun. Electron beam energy: (c) and (d) 70 eV, (e) 44 eV.

Fig. 4.8a presents an STM image of graphene grown on Ru(0001) with the CVD method. Ru(0001) is annealed at 800 °C with the precursor (ethylene, C_2H_4) pressure of 2×10^{-8} mbar. An extended and continuous moiré pattern is absent. I observe a lot of small graphene domains containing only a few moiré unit cells. Fig. 4.8b displays the Fourier transformation of Fig. 4.8a. The six spots originated from the moiré periodicity reformulate into six arc, smearing around the (0,0) spot. These six arcs indicate the existence of the misaligned graphene domains.

The LEED pattern measured on this gr/Ru(0001) sample displays the same small arcs: the diffraction spots from graphene are elongated around the Ru(0001) spots (Fig. 4.8c). The sets of satellite spots from the moiré pattern are not extended. The second-order spots are barely visible, indicating the small size of the graphene domains.

In Sec. 4.1, I demonstrated the growth of hBN/Ru(0001) with good alignment. To prepare the in-plane hetero-structure of hBN and graphene, I use a two-step CVD process: (i) I firstly grow sub-monolayer of hBN on Ru(0001) by 10 minutes of CVD. The borazine pressure is set to 1×10^{-8} mbar to guarantee high quality of the hBN flakes. The Ru(0001) substrate is set to 800 °C. (ii) I continue the CVD process but change the precursor to ethylene (2×10^{-8}) to cover the Ru(0001) with graphene.

Fig. 4.8d and e present the LEED pattern measured on the two-step CVD growth sample. Compared with Fig. 4.8c, the diffraction spots from the 2DMs are much sharper and the arc-like feature disappears. The moiré pattern becomes more pronounced and extended. These observations indicate an increased degree of ordering on the hBN-gr/Ru(0001) sample than gr/Ru(0001).

A similar increased quality of graphene is observed on Ir(111). CVD grown gr/Ir(111) (930 °C, 5×10^{-8} mbar, 20 minutes) contains misaligned domains, indicated by the diffraction spots from graphene elongated around the Ir(111) spots (Fig. 4.9a). A two-step preparation similar to the case with Ru(0001) substrate is commissioned for hBN-gr/Ir(111). After the first step of sub-monolayer growth of hBN (930 °C, 2×10^{-8} mbar, 5 minutes). The diffraction spots from hBN is not elongated (Fig. 4.9b). The absence of the satellite spots indicates the small size of the hBN flakes. Another CVD step for graphene growth (930 °C, 5×10^{-8} mbar, 20 minutes), which is the same as the gr/Ir(111) growth, leads to the hetero-structure of hBN-gr on Ir(111). The LEED pattern indicates a good alignment between the 2DMs and Ir(111) (Fig. 4.9c).

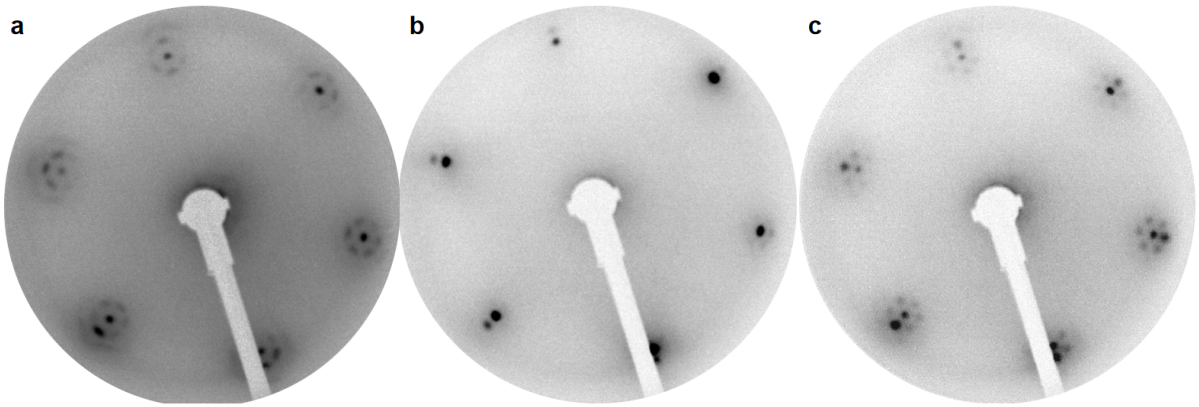

Figure 4.9: LEED patterns measured on 800 °C-CVD grown (a) gr/Ir(111), (b) sub-monolayer hBN/Ir(111), and (c) hBN-gr/Ir(111). Electron beam energy 72 eV.

For both substrates, given that the second CVD step for hBN-gr is the same as the preparation of the pure graphene sample, the increased quality of graphene is thus induced by the hBN flakes grown in first CVD step. In the adsorption-decomposition-diffusion/aggregation model of the CVD growth, when a molecular radical diffuses and encounters an existing 2DM flake, it joins the flake at the edge, leading to the growth of the flake. In the second CVD step for hBN-gr I discuss here, the C

containing radicals diffuse to join the existing hBN flakes. Since the hBN flakes are well-oriented on the TM substrate, the sequential growth of graphene will also align with the substrate. The in-plane epitaxy provides another driving force for the alignment of graphene in addition to the interaction to the substrate.

Chapter 5

Adsorption of small B/N containing molecules on TM surfaces

Contradictions on the geometric structure of epitaxial hBN from different charachterization methods can be found in many reports on the corrugation geometry of 2DM/TM systems. Such contradictions originate from some delicate obstacles in the investigations of the precise corrugation of these epitaxial systems for both experimental and theoretical approaches.

For experimental approaches, I discuss here only some characterization methods, which are categorized into two types: local measurements by SPM, and PE-based averaging measurements (XPS, XSW, PHD). Widely used SPM methods measure the height of the sample by following a contour of a specific response (tunneling current for STM, and oscillation frequency for nc-AFM) with a height adjustable tip. In brief, SPMs do not measure the height directly, hence the term apparent height. Instead, the electronic structure plays a vital role. However, the electronic structure itself is spatially modulated within the moiré unit cells.

For STM, the electronic structure (LDOS) of the epitaxial system plays a vital role for the height measurement. It has been shown that the contrast of the apparent heights of the valley and hill regions of hBN/TM can flip when using different tunneling parameters (hBN/Ir(111) [23], hBN/Rh(111) [24]). For AFM, local electronic structure can also induce the apparent height contrast inversion [25]. This contrast inversion is due to the different shapes of the force-distance-curve in the valley and hill region of the moiré unit cell.

The PE-based averaging methods collect signals from a micrometer scale area on the sample, which contains a very large amount of atoms. Thus the reliable measurement demands a high quality sample with ignorable defect concentration (including misaligned domains). For substrates interacting strongly with 2DM, such high quality samples are achievable by an optimized growth process. But for substrates, such as Cu(111), which interact very weakly with hBN, it is not an easy task to prepare a hBN layer with high quality. Rotational domains emerge [61]. To the best of the writer's knowledge, single orientation hBN/Cu(111) preparation has not been reported so far. Even for high quality 2DM layers, dividing C 1s (or N 1s and B 1s) signal(s) into individual peaks could be difficult: More than 100 C (or N/B) atoms are in one moiré unit cell. Their properties (i.e. binding energy) change gradually from hill to valley region. Categorizing all of them into a few components

can be a very rough approximation.

As for the theoretical approach, i.e. DFT calculation, a finite supercell is used: $(m \times m)$ atomic unit cells of the 2DM on $(n \times n)$ atomic unit cells of TM surface. The lattice mismatch leads to questions on commensurability: whether the 2DM/TM system is commensurate, and when it is commensurate, the correct choice of m and n. As can be imagined, the difference between m_0-n_0 and $(m_0 + 1)$-$(n_0 + 1)$ is quite small when m and n are larger than 10. Thus the determination of m-n is quite tricky. For example, there has been some debate for hBN/Ir(111) (11-12 *vs* 12-13) and hBN/Ru(0001) (12-13 [62, 63, 64] *vs* 13-14 [65]) systems. This small dimensional difference in the plane parallel to the substrate surface could lead to large difference in the corrugation geometry.

In literature, there exists an ambiguity when the 2DM-TM interaction is discussed. It is commonly accepted that Ru(0001) interacts strongly with graphene and hBN. Pt(111) and Cu(111) interact weakly. While Ir(111) lies in the middle of the spectrum. This judgment of the interaction strength is generally based on macroscopic properties of 2DM/TM systems. For example, the common emergence of rotational domains (gr/Pt(111), hBN/Cu(111) [61]) is a symbol for weak interaction. The clear modification of the 2DM's band structure means strong interaction (hBN/Ru(0001) [28]).

However, this description of the interaction strength is first of all only qualitative. Moreover, it is only a macroscopic description, which ignores the corrugation nature of the 2DM sheet. The corrugation geometry is the result of the interplay between two important factors: the **lattice mismatch** and the **local interaction** between 2DM and the underlying TM substrate. Assuming two substrates with the local interaction of the same strength, the substrate with smaller lattice mismatch to 2DM would have more atoms effectively bonded to the 2DM. This 2DM/TM system would thus display a stronger average 2DM-TM interaction in macroscopic measurements. On the other hand, on a TM substrate which has no lattice mismatch with the 2DM ($m = n = 1$) and also interacts weakly with the 2DM, the 2DM layer would always have a good alignment to the substrate. This 2DM/TM system would thus macroscopically present a strong 2DM-TM interaction.

I hereby propose a method to address part of the problems of studying the corrugation geometry of hBN/TM systems. The idea is to use small molecules to mimic hBN locally. In this way, one of the two contributing factors is avoided, i.e. lattice mismatch, and I only focus on the local interaction.

In the first section of this chapter, I calculate the adsorption of some small molecules (molecular radicals) on Ir(111), and compare them with the valley regions of hBN/Ir(111). The height of hBN in the valley regions (h_{V}) is used as a standard to select the molecules with similar adsorption height. For h_V, I use the value 2.20 Å obtained from XSW measurements [26]. DFT calculation of a moiré unit cell containing (12×12)-hBN on (11×11)-Ir(111) yields similar values (B 2.13 Å, N 2.27 Å [26]).

The second section focuses on the selected molecules, and calculates their adsorption on the different TM substrates. I firstly compare the results with the hBN's heights in the valley regions on these TM substrates. Then the adsorption energy is used as a measure of the interaction strength and the hBN-TM interaction is compared among different substrates.

The theoretical calculation is done within the scheme of DFT. This ab-initio method simplifies a N-electron problem to a single-electron problem by replacing the troubling electron-electron interaction with an effective pseudo-potential. To achieve this simplification, the electron density

distribution rather than the multi-electron wave-function is used as the basic variable. The validity of using the electron density is supported by the Hohenberg-Kohn theorem [66].

The DFT calculations are performed with the Perdew-Burke-Ernzerhof GGA functional [6] using the ABINIT code [7, 8]. The cutoff energy and the k-space Monkhorst-Pack grid are chosen after convergence calculations for each systems. For the adsorption of smaller molecules (B, N, BH, NH_3, BN_3, NB_3), a 2×2 unit cell of TM substrate including only one layer of TM atoms is used (Fig. 5.1). For the adsorption of B_3N_3 and borazine molecules, a larger unit cell (3×3, Fig. 5.2) is used. The height of the unit cells are chosen as 10 Å to have enough vacuum space above the adsorbed molecules.

I also calculate the adsorption energies of these six molecules. Firstly, the energy of the free molecule E_{mol}, and the energy of Ir(111) substrate E_{Ir} are calculated. Then I calculate the energy of the adsoprtion system $E_{\mathrm{mol/Ir}}$. The adsorption energy is calculated as the as:

$$E_{\mathrm{ad}} = E_{\mathrm{mol}} + E_{\mathrm{Ir}} - E_{\mathrm{mol/Ir}}. \tag{5.1}$$

The calculations are performed on the high-performance cluster of University of Siegen.

5.1 The adsorption of B, N, BH, NH_3, BN_3, NB_3, B_3N_3, and borazine on Ir(111)

To simulate hBN locally in the valley region of the moiré unit cell, the smallest test molecules are obviously B and N atoms. The calculation reveals different adsorption sites for B and N: B adsorbs in the hollow sites of the Ir(111) surface, while N adsorbs directly on top of one Ir atom (Fig. 5.1a and b). These adsorption sites agree with the positions of the B and N atoms in the valley regions of hBN/Ir(111) moiré unit cell [26]. However, the adsorption height is 1.19 Å for atomic B, and 1.67 Å for atomic N. They are much lower than h_{V}. The adsorption energy is quite large for both atoms: 7.43 eV for B, and 7.58 eV for N.

The much lower adsorption heights than h_V originate from the isolated nature of atomic B and N. In hBN, each N/B atom forms three 3 σ-bonds to the neighboring B/N atoms. To simulate this bonding configuration, the adsorption of BH_3 and NH_3 are calculated.

The calculation reveals that BH_3 is not stable when adsorbed on Ir(111). It dehydrogenates. The adsorption of BH is calculated instead. The adsorption geometry is presented in Fig. 5.1c. The B atom still locates at the hollow site. The H atom sits on top of B, i.e. the H-B bond is perpendicular to the Ir(111) substrate. The adsorption height of B is 1.42 Å, slightly higher than the atomic B, yet still much lower than h_{V}.

The adsorption geometry of NH_3 is presented in Fig. 5.1d. The N atom sits directly on top of one Ir atom. The three N-H bonds expand towards the three nearest Ir atoms in plane, and upwards in the normal direction. Comparing with the structure of isolated NH_3, it is clear that the lone pair of electrons of the N atom forms a bond with the Ir atom below N. The height of the H atoms is 2.33 Å. The height of the N atom is 2.02 Å, which is similar to h_{V}. Previous DFT calculations [67] using more than one layer of Ir atoms as the substrate yields a higher adsorption height for NH_3 (2.15 Å),

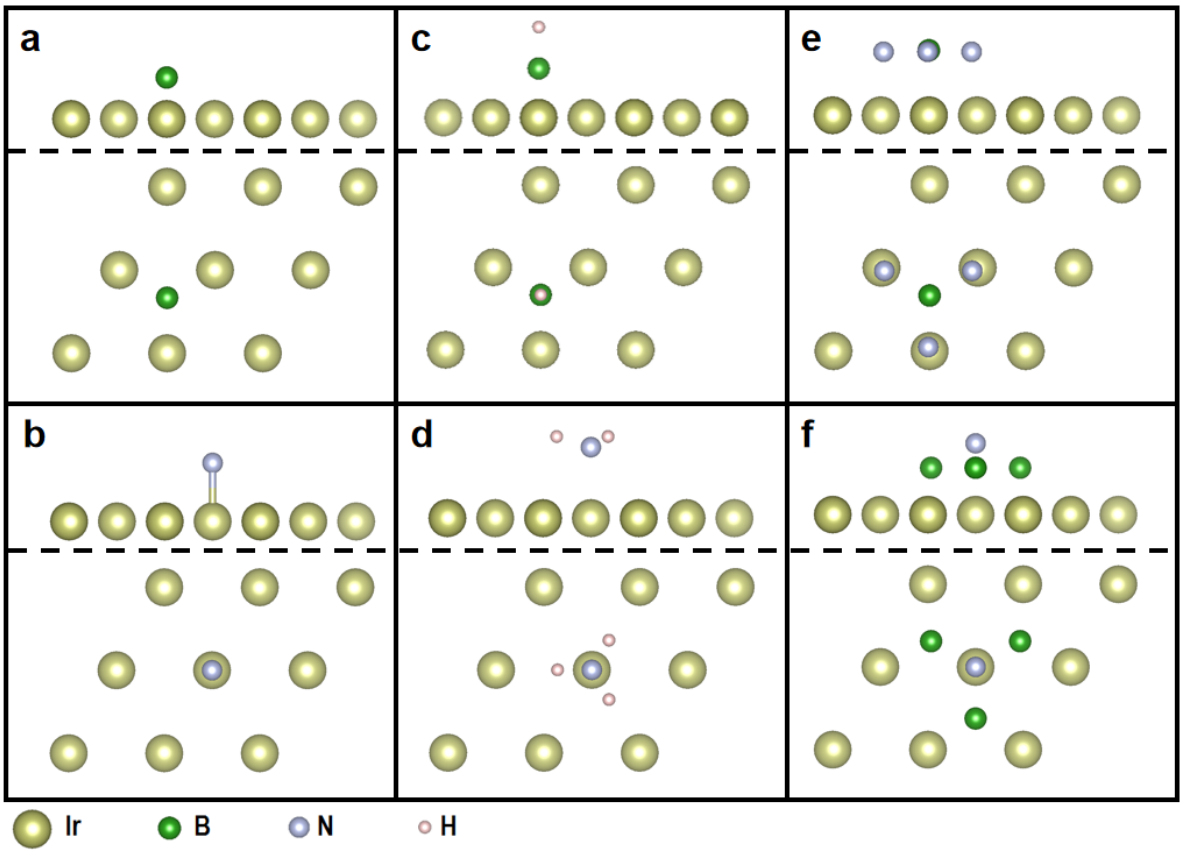

Figure 5.1: Adsorption geometries of (a) atomic B, (b) atomic N, (c) BH, (d) NH_3, (e) BN_3, and (f) NB_3 on Ir(111). Each subfigure presents the side view of the adsorption geometry in the top panel, and top view in the bottom panel.

which is even closer to h_V. Hence the ammonia molecule is a good candidate to simulate hBN in the valley regions of the moiré unit cell.

A previous ARPES measurement showed that the hollow site of Ir(111) is favored for saturated 1×1 adsorption of ammonia. However, previous DFT calculations agrees with my calculated adsorption geometry [67, 68]. The 2×2 unit cell corresponds to a 25% coverage. The different coverages might be the cause for such difference to the measurement results. Another point worth mentioning is that the directions of the three σ-bonds formed by the N atoms in NH_3 are towards the three nearest Ir atoms in plane. However, the three σ-bonds on N atom in the valley regions of hBN/Ir(111) moiré unit cells points to the neighboring hollow sites.

In the NH_3 molecule, the N atom is bonded with three H atoms, while in hBN, three B atoms. To achieve the same bonding configuration of the B/N atoms, I also calculate the adsorption of BN_3 and NB_3 on Ir(111). The adsorption geometries are presented in Fig. 5.1e and f. For BN_3, the B atom locates at the hollow site. The three N atoms are nearly on top of the three nearest Ir atoms. They are slightly shifted towards the B atoms in the center. The heights of the B and N atoms are almost the same (N: 1.89 Å, B: 1.82 Å). Compared with the adsorption height of NH_3, they are not close to h_V. Hence they BN_3 does not mimic hBN in the valley regions.

For NB_3, the N atom sits directly on top of one Ir atom at the center, and the three B atoms sit at the neighboring hollow sites. The adsorption height of the N atom (2.05 Å) is close to h_V. However, the B atoms are very close to the Ir(111) substrate (1.35 Å).

The adsorption heights of the B/N atoms in the six molecules (excluding BH_3) are summarized in Tab. 5.1. Comparing among these six molecules, I found that the intrinsic adsorption site for B atom is the hollow site. This results in a very low adsorption height. For N atom, it adsorbs directly on top of one Ir atom, and the adsorption height is much higher than B. Hence when a molecule contains a B-N pair, the N atom drags the B atom away from the Ir(111) substrate, since the N-B bond length is shorter than the distance between the nearest adsorption positions of N and B. Taking h_V as a reference for the adsorption height, NH_3 turns out to be the best candidate to simulate hBN in the valley regions of the moiré unit cell.

	B	BH	BN_3	N	NH_3	NB_3	B_3N_3	borazine
Height (Å)	1.19	1.42	1.89/1.82	1.66	2.02	1.35/2.02	1.69/1.97	2.07/2.02
Energy (eV)	7.43	7.22	5.02	7.58	1.24	4.68	4.53	1.45

Table 5.1: Adsorption heights and adsorption energies of B, BH, BN_3, N, NH_3, NB_3, B_3N_3, $B_3N_3H_6$. For molecules containing both B and N atoms, the first/second value is for the adsorption height of the B/N atom(s).

The adsorption energies of the six molecules are listed in Tab. 5.1. Apart of NH_3, all other molecules contains atoms with unpaired electrons which leads to extra bonding to the Ir(111) substrate. Hence the adsorption energies of these five molecules are much larger than NH_3. The full-shell structure of all the atoms in NH_3/Ir(111) is another support for NH_3 to be the best candidate to simulate hBN in the valley regions of the moiré unit cell.

Additional to the six small molecules, I also calculate the adsorption of borazine and its dehydrogenated compound B_3N_3 on Ir(111). A (3×3) Ir(111) unit cell is used to exclude inter-molecular interaction. The adsorption geometries are presented in Fig. 5.2a and b. The positions of N/B atoms are very similar to those in the valley regions of hBN/Ir(111). For the borazine molecule, the six H atoms bend away from the Ir(111) substrate. The heights of the N and B atoms are quite similar, rendering a rather flat ring parallel to the substrate. For B_3N_3, it does not sustain the flat ring geometry. Due to the unpaired electrons, the B atoms sink deeper into the hollow sites to gain additional binding to the substrate. This additional binding gives rise to the larger adsorption energy than borazine. In the valley regions of hBN/Ir(111), the six-atom ring is rather flat, i.e. the N and B atoms are at a similar height (N 2.22 Å, B 2.17 Å [26]), which resembles the geometry of the borazine molecule.

Summarizing, using h_V as the standard for the adsorption height, I find that among all the molecules I investigated, the ammonia and borazine molecules resemble the valleys of hBN/Ir(111) most.

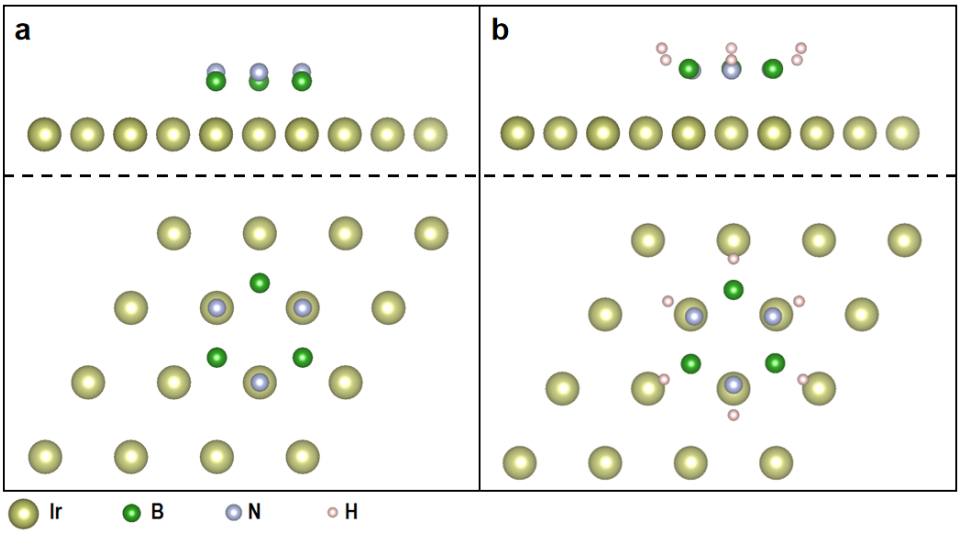

Figure 5.2: Adsorption geometries of (a) B_3N_3 and (b) borazine, ($B_3N_3H_6$) on Ir(111) in a single layer 3×3 unit cell. Each subfigure presents the side view in the top panel, and top view in the bottom panel.

5.2 Ammonia and borazine adsorption on Ni(111), Pt(111), Ir(111), and Ru(0001)

In the last section, I have calculated the adsorption of many small molecules on hBN/Ir(111). And the ammonia and borazine molecules turn out to be the best candidates to simulate the valleys of hBN/Ir(111). In this section, I calculate the adsorption of these two molecules on different TM substrates.

For the NH_3 molecule, the adsorption is calculated on four different TM substrates: Ni(111), Ru(0001), Ir(111), and Pt(111). The adsorption geometry is very similar on these four substrates (see Fig. 5.1d): The adsorption heights on these four substrates are very similar. The orientation of the NH_3 molecule with respect to the four substrates is also the same. The adsorption height and energy on different substrates are listed in Tab. 5.2. I firstly compare the calculated adsorption height of ammonia with the height of the valley regions of the hBN/Ni(111), hBN/Ru(0001), and hBN/Pt(111). I exclude the Ir(111) substrate since it is already discussed in the last section.

	Ni(111)	Ru(0001)	Ir(111)	Pt(111)
Height of N (Å)	1.96	2.07	2.02	2.04
Height of H (Å)	2.27	2.39	2.32	2.34
Energy (eV)	0.46	1.33	1.24	0.73

Table 5.2: Adsorption heights and adsorption energies of ammonia molecule on Ni(111), Ru(0001), Ir(111), and Pt(111).

For hBN/Ni(111), hBN has a lattice constant very close to that of Ni(111), leading to a 1×1 on 1×1 superstructure. Several measurements on its geometry have been reported. A LEED intensity analysis reported an adsorption height of 2.22 Å for the N atoms, and 2.04 Å for the B atoms [69]. Angle-scanned XPD experiments combined with single- and multiple scattering calculations yielded 1.95 Å and 1.88 Å [70, 71]. XSW measurements yielded 2.13 Å and 1.98 Å [72]. Since the unit cell contains only very few atoms, I have also conducted a DFT calculation of hBN/Ni(111) with two layers of Ni atoms. The calculation yields the adsorption height of 2.13 Å for N atoms, and 2.03 Å for B atoms. All the reported adsorption heights and my calculation results are very similar. The calculated adsorption height of ammonia (1.96 Å) is also very close to these values.

For hBN/Ru(0001), a DFT calculation with a 14(hBN):13(Ru) supercell yielded the adsorption height of approximately 2.0 Å in the valleys [73]. Another calculation reported used a smaller supercell (13:12), and yielded a higher adsorption height of 2.14 Å [28, 74]. My calculation of NH_3/Ru(0001) yielded a adsorption height (2.07 Å) in between these two reported values. On the experimental side, the preliminary analysis of the XSW measurements on hBN/Ru(0001) yields a height of 2.01 Å for the valleys of hBN/Ru(0001), which is also close to the DFT calculation.

For hBN/Pt(111), the XSW measurements reveal an average adsorption height of 3.41 Å, which is much higher than the calculated adsorption height of NH_3 (2.04 Å). However, the separation of the valley regions in the N 1s and B 1s spectra proves to be very difficult. The size of the valley regions (number of atoms that are strongly bonded to the substrate) is very small due to the large lattice mismatch between hBN and Pt(111). Hence I deduce that h_V in hBN/Pt(111) is much lower than the average height. To the best of the author's knowledge, no precise measurement of the hBN/Pt(111) corrugation geometry has been reported.

Summarizing, the adsorption height of ammonia is very similar to h_V on Ni(111), Ru(0001), and Ir(111). Hence I can use it to simulate N atoms in the valley regions: the adsorption energy of ammonia can be used as a measure to the local hBN-TM interaction in the valley regions. Comparing the adsorption energies on the four substrates, I find the local interaction strength between hBN and the substrate is similar on Ru(0001) and Ir(111). The interaction strength is weak on Ni(111) and Pt(111). The absolute values give a relation: $E_{\mathrm{Ru}} > E_{\mathrm{Ir}} > E_{\mathrm{Pt}} > E_{\mathrm{Ni}}$.

	Ru(0001)	Ir(111)	Pt(111)
Height of B (Å)	2.04	2.02	2.05
Height of N (Å)	2.04	2.07	2.10
Height of H (Å)	2.38/2.67	2.35/2.73	2.35/2.70
Energy (eV)	2.45	1.45	0.34

Table 5.3: Adsorption heights and adsorption energies of borazine molecule on Ru(0001), Ir(111), and Pt(111). For H, the first/second value is for the H atoms bonded with N/B atoms.

For the borazine molecule, I calculate the adsorption on Ru(0001), Ir(111), and Pt(111). The adsorption geometry is also similar on the three substrates (Fig. 5.2b): N atoms sit on top of one TM atom, and B atoms sit in the neighboring hollow sites. The six-atom ring stays rather flat, i.e. the height of B and N atoms are similar. The B-H and N-H bonds bend upward. For the adsorption

energy, the relation $E_{\mathrm{Ru}} > E_{\mathrm{Ir}} > E_{\mathrm{Pt}}$ still stands. However, comparing between the absolute values, I find that the difference between E_{Ru} and E_{Ir} is 1.0 eV, much larger than the difference calculated by ammonia molecule adsorption (0.09 eV).

Comparing between the adsorption of the ammonia and borazine molecules, I find that the N atoms are shifted to the center of the six-atom ring in the borazine adsorption, hence slightly off the top of the Ir atom. For NH_3, the N atom locates exactly on top of a TM atom. This difference originates from the fact that the lattice constants of both TM substrates are larger than the N-N distance in the borazine molecule. Hence the two N-B bonds drag the N atom off the center of the top site. Beside the N-Ir bonding similar to the NH_3/Ir(111) case, borazine also endures deformation when adsorbed on the TM substrate, which reduces the adsorption energy. The lattice constant of Ir(111) is larger than that of Ru(0001), and they are both larger than the N-N distance in the borazine molecule: $a_{\mathrm{Ir}} > a_{\mathrm{Ru}} > d^{\mathrm{N\text{-}N}}_{\mathrm{borazine}}$. When adsorbed on Ir(111), the deformation of the borazine molecule is severer than on Ru(0001). This deformation leads to the relatively large difference in the adsorption energies on Ru(0001) and Ir(111) for the borazine molecules.

The dimensional difference between the borazine molecule and the TM substrate resembles the lattice mismatch between hBN and the TM substrates. Hence the adsorption geometry of borazine is the trade-off between the dimensional mismatch and the atomic interaction to the TM substrate. While for the adsorption of the ammonia molecule, the only factor involved is the atomic interaction.

Summarizing, based on the adsorption energies of NH_3, the local atomic bonding to the substrate is similar for Ir(111) and Ru(0001). However, based on the adsorption of borazine, a macroscopic stronger hBN-Ru(0001) interaction than hBN-Ir(111) is then expected, which agrees with the strong modification of the hBN band structure on Ru(0001) [28], yet rather pristine band structure on Ir(111) [75]. For Ni(111) and Pt(111), the local atomic interaction is weak. The very close lattice constant between hBN and Ni(111) leads to two very well-defined orientation of hBN domains [76]. While the large lattice mismatch between hBN and Pt(111) leads to easy misalignment (see Sec: 4.1).

Chapter 6

Alkali metal adsorption on hBN/Ru(0001) and hBN/Ir(111)

In this chapter, I present the adsorption of alkali metals on the hBN/TM system. When deposited on hBN/TM, the adatoms can either directly go between the hBN layer and the substrate (atomic H onto hBN/Rh(111) [29], Li onto hBN/Ir(111) [30]), or adsorb on top of the hBN sheet (most other larger atoms).

As demonstrated in Sec. 2.3.1, the moiré pattern of hBN/TM provides a template for the adsorbates. This templating effect originates from the spatially modulated adsorption energy within the moiré unit cell, resulting in certain preferred adsorption sites. In the apparent "hill and valley" (historically "wire and pore") description of the moiré geometry, most adatoms prefer the valley regions of the moiré unit cell. Some examples are the adsorption of Ir on hBN/Ir(111) [37], the adsorption of Ti, Cr, Mn, Fe, Co, Au, and Xe on hBN/Rh(111) [36, 35, 33, 77], the adsorption of Au on hBN/Ru(0001) [63]. Due to the periodicity of the moiré pattern, the preferred adsorption sites form a hexagonal lattice, hence the ordering of the adsorbates, i.e. the templating effect.

When the adatoms reach certain density on the surface, interaction between the adatoms comes into play. For adatoms with attractive interatomic interaction, they aggregate and form monolayer islands (Au/hBN/Pt(111) [78]) or clusters with vertical stacking (Au/hBN/Rh(111) [78], Ir/hBN/Ir(111) [37]). These islands or clusters still take the moiré pattern as a template. With high enough adatom density, they have the possibility to coalesce and grow across several moiré unit cells.

To the best of my knowledge, there have not been many studies reported on the systems of alkali metal adsorption on hBN/TM. Ref. [43] studied the adsorption of Li on hBN/Au/Ni(111). They observe a shift of the hBN bands due to the charge transfer from Li to the substrate. Interestingly, even though the hBN sheet is a large band gap insulator, the alkali metal still ionizes. As a result, the adsorbed alkali metal atoms are positively charged, thus repulsive to each other. Intuitively, they would not aggregate. The competition between the interatomic repulsion and the spatially modulated adsorption determines the geometric arrangement of the alkali metal atoms. In this section, I present the investigation of the adsorption morphology of Cs and K, on hBN/Ru(0001) and hBN/Ir(111).

The pristine hBN/Ru(0001) and hBN/Ir(111) are prepared as described in chapter 4. The high quality of the samples is testified by LEED and STM. The alkali metals are deposited from a home-

built evaporator, where a direct current is driven through the alkali metal dispensers. For the consistency of the deposition rate, the sample and evaporator are always kept at the same positions for all preparations. The distance between the dispensers and the sample is around 10 cm. This distance is chosen to achieve reasonable deposition rate, and to avoid heating on the sample by the hot dispensers. The absence of sample heating by the dispensers is testified by a thermocouple near the sample.

In Sec. 6.1 and 6.2, I present the STM study of alkali metal (Cs and K) adsorption on hBN/Ru(0001) and on hBN/Ir(111) respectively, mainly with relatively low adsorption density. Sec. 6.3 addresses honeycomb structured Cs adsorption on hBN/Ir(111) achieved by depositing Cs on the hot substrate. The geometric and electronic properties are systematically studied by PE characterization methods.

6.1 Alkali metal adsorption on hBN/Ru(0001)

When deposited on hBN/Ru(0001), Cs and K atoms selectively sit in the valleys of the moiré unit cell. As an example, Fig. 6.1 presents an STM image of hBN/Ru(0001) after 10 minutes of Cs deposition (dispenser current 5 A). The dark circular regions are the valleys in the moiré pattern. The bright protrusions in the valleys are the adsorbed Cs atoms.

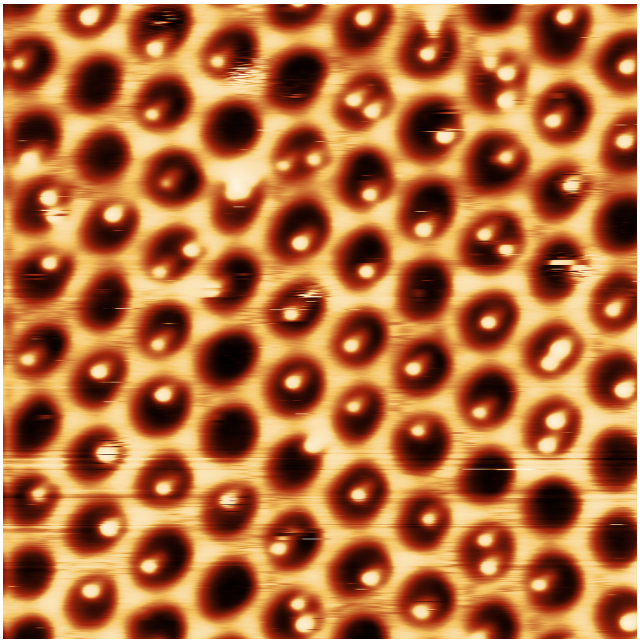

Figure 6.1: STM image of Cs adsorption on hBN/Ru(0001). 30×30 nm^2, $U_\mathrm{b} = -2.0$ V, $I_\mathrm{tunneling} = 20$ pA.

One inevitably notices that some valleys are occupied by more than one Cs atom, which can be easily distinguished by separated bright protrusions in the STM image. This distinguishability of individual Cs atoms stands out among other adsorbates (especially transition metals), which are normally imaged as continuous islands or clusters on hBN/TM [37, 78].

Having the lowest ionization energies, alkali metal atoms are prone to lose the single electron in

their outmost s orbitals. Once positively charged, they repel each other, leaving detectable distance between them. Instead of using apparent heights or sizes of the islands or clusters as an indirect indicator [79], I can directly determine the number of atoms in each moiré unit cells.

To systematically study the adsorption process, a series of samples are prepared with different amount of Cs deposition (Fig. 6.2). With increasing amount of Cs deposited, more and more valleys are occupied, and the average occupation number of Cs atoms in one valley increases.

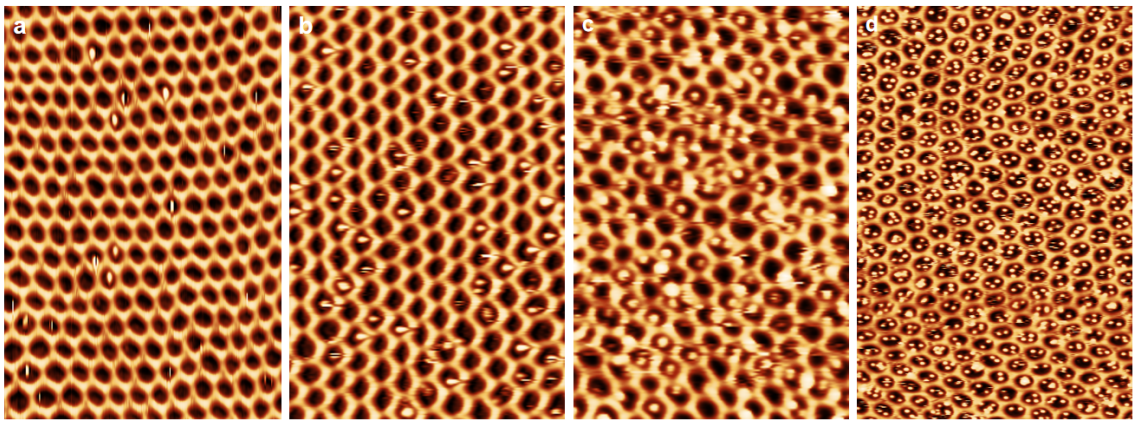

Figure 6.2: hBN/Ru(0001) with different amount of Cs adsorption. Deposition time: (a) 1 minute, (b) 4 minutes, (c) 10 minutes, (d) 20 minutes. 40×60 nm^2, $U_\mathrm{b} = -2.4$V, $I_\mathrm{tunneling} = 20$ pA.

For each sample, the numbers of atoms in over 1000 moiré unit cells are counted. The deposition time and the average occupation number λ for each sample are listed in Tab. 6.1: I calculate the

Deposition Time	1 min	4 min	10 min	20 min
Average Occupation λ	0.049	0.225	1.107	3.194

Table 6.1: Deposition time and average occupation in one moiré unit cell of the samples presented in Fig. 6.2.

ratio of moiré unit cells with different occupation numbers among all moiré unit cells counted. The distributions of occupation number from the four samples are presented in Fig. 6.3 (blue bars).

Poisson Distribution

Firstly, I compare the observed distribution with the Poisson distribution. For Poisson distribution, the ratio of the cells with n adatoms inside over all the cells is

$$P(\lambda, n) = \lambda^n e^{-\lambda}/n!, \tag{6.1}$$

λ being the average number of adatoms in one cell. The Poisson distribution for each sample is plotted as yellow bars in Fig. 6.3. Comparing between the blue and yellow bars, it is clear that the Poisson distribution is much broader than the observed one. This is due to the absence of a crucial presumption for Poisson distribution: each event being independent to others. Once a Cs atom occupies a moiré unit cell, it repels other Cs atoms. Thus the probability for another Cs atom to

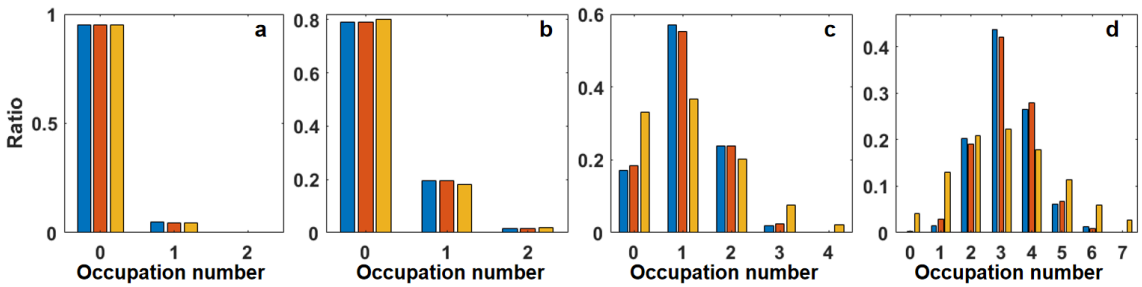

Figure 6.3: The distribution of occupation numbers of the four samples presented in Fig. 6.2: experimentally observed (blue), Monte Carlo simulation (red), and Poisson model (yellow).

go into this cell is reduced. To describe such an collective adsorption process, a simple Monte-Carlo simulation is made.

Monte Carlo Simulation

This simulation contains two parts: (i) the calculation of the energy of n adatoms in one moiré unit cell; (ii) Monte Carlo (MC) process for a large system to reach equilibrium.

To calculate the energy of one cell with n adatoms, $\epsilon(n)$, a simple model is used. A circular infinite rectangular potential well confines n charged particles (Fig. 6.4a):

$$V(\vec{r}) = \begin{cases} 0 & |\vec{r}| \leq R_0 \\ +\infty & |\vec{r}| > R_0 \end{cases} \tag{6.2}$$

In this model, the minimal energy for each n is achieved by all the atoms siting at the circular edge of the well and forming a regular polygon. Some typical moiré unit cells occupied by 1 to 5 Cs atoms are presented in Fig. 6.4b-f. The energy levels $\epsilon(n)$, calculated with this simple model, are listed in Tab. 6.2:

n	1	2	3	4	5	6	7
$\epsilon(n)$	0	0.5	1.732	3.828	6.883	10.964	16.133

Table 6.2: Energies $\epsilon(n)$ of n atoms occupying one moiré cell, in the unit of q^2/R_0.

The initial state of the MC process is a Poisson distribution: a large number of atoms ($N \cdot \lambda$) are randomly and independently assigned to a large number (N) of cells. The system then goes through some diffusion steps. One diffusion step involves the hopping of one adatom from one randomly selected cell to its neighboring cells. After enough hopping steps, the occupation number distribution remains in a stable final state.

Now let us look at one hopping step more closely. Assuming the occupation number of the randomly selected cell is N_0, and the neighboring cells respectively have n_i ($i = 1, 2, ..., 6$) atoms (Fig. 6.4g). After one hopping step, there are 6 possible configurations: ($n_0 - 1$,$n_1 + 1$,n_2,n_3,n_4,n_5,n_6), ($n_0 - 1$,N_1,$n_2 + 1$,n_3,n_4,n_5,n_6),..., ($n_0 - 1$,N_1,n_2,n_3,n_4,n_5,$n_6 + 1$). Additionally, it is also possible that the atom stays and this local 7-cell system remains unchanged, i.e. (N_0,N_1,n_2,n_3,n_4,n_5,n_6). The

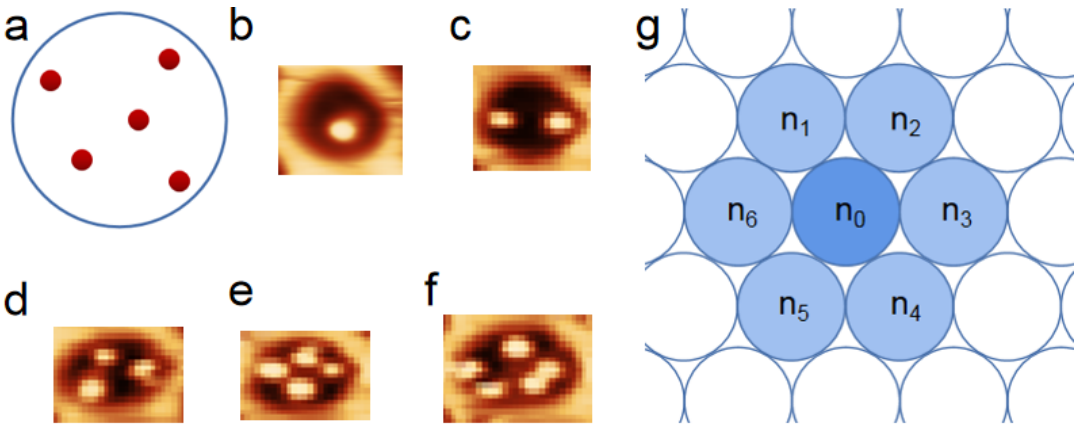

Figure 6.4: (a) Sketch of the model: multi charged particles trapped in a circular well. (b)-(f) STM images as examples of 1 to 5 Cs atoms inside one valley of the moiré cell. (g) Example of a hopping step in the MC process.

probability (p_i) to end in each of these 7 possible final configurations depends on the energies (E_i) of these 7 configurations, where

$$E_0 = \epsilon(n_0) + \sum_{i=1}^{6} \epsilon(n_i),$$

and for $i = 1, 2, ..., 6$

$$E_i = \epsilon(n_0 - 1) + \epsilon(n_i + 1) + \sum_{j \neq i} \epsilon(n_j).$$

Treating this hopping step in these 7 cells as a local canonical ensemble, the probabilities that the final state turns out to be these 7 configurations are respectively:

$$p_i = \frac{e^{-E_i/kT}}{\sum_{i=0}^{6} e^{-E_i/kT}}. \tag{6.3}$$

I measure the distances between the two adatoms in 20 double occupation moiré unit cells and use the average value 1.34 nm, as the diameter of the well used in the MC simulation. As can be seen from the description above, then there is only one free parameter in this MC process, the charge of the adatoms q. This parameter is manually adjusted to make the best fit between the simulated distribution and the observed one. The optimized simulated distributions for each adsorption density are presented as red bars in Fig. 6.3. In general, they resemble the observed distributions (blue bars), much better than the Poisson distribution. The best fits are achieved with $q = 0.22e_0$ for 1 min, 4 min, and 10 min Cs deposition, and $q = 0.14e_0$ for 20 min Cs deposition.

The decreased average charge transfer is explained as follows. With hBN being a large band gap insulator, electrons transfer from adsorbed Cs to the Ru(0001) substrate. The positively charged Cs adsorption and negatively charged Ru(0001) substrate create a static electric field between them. Adding additional Cs adsorption strengthens this field. Yet the additional charge transfer has to go against this electric field. Hence, even though the charge density increases from the 10-minute

sample to the 20-minute sample ($0.22e_0 \cdot 1.107 < 0.14e_0 \cdot 3.194$), the average charge transfer for each Cs atom decreases.

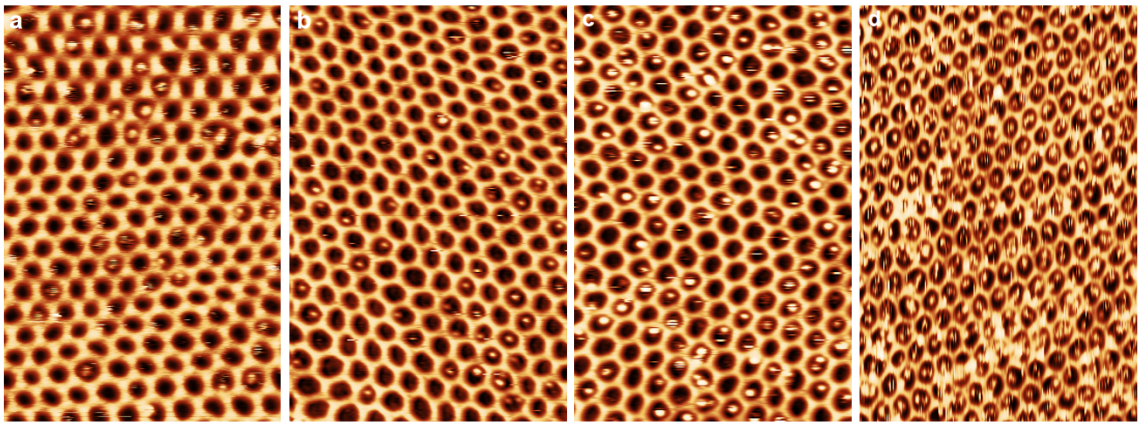

Figure 6.5: hBN/Ru(0001) with different amount of K adsorption. K deposition time: (a) 2 minutes, (b) 6 minutes, (c) 15 minutes, (d) 30 minutes. 40×60 nm^2, $U_\mathrm{b} = -2.4$V, $I_\mathrm{tunneling} = 20$ pA.

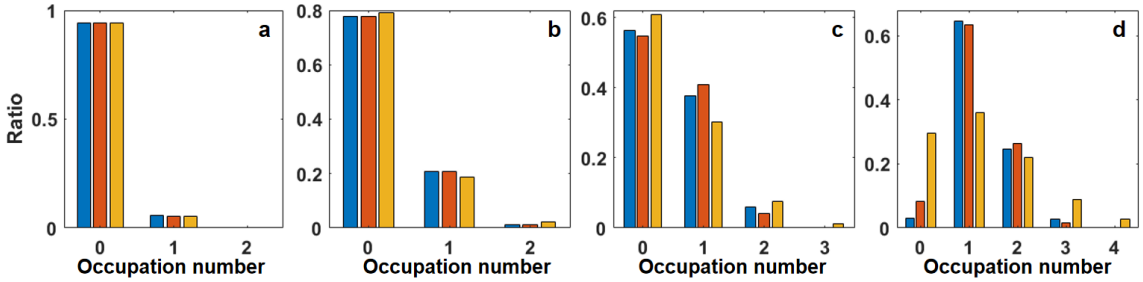

Figure 6.6: The distribution of occupation numbers on the four samples presented in Fig. 6.5: experimentally observed (blue), Monte Carlo simulation (red), and Poisson model (yellow).

A similar set of preparations and measurements are made for K adsorption on hBN/Ru(0001). The STM measurement results are displayed in Fig. 6.5. The behavior of the adsorbed K atoms is very similar to Cs. This similarity is expected since the two elements have very similar chemical properties. The occupation number distributions are presented in Fig. 6.6 as blue bars. The deposition time and average occupation for each sample is listed in Tab. 6.3. Poisson distributions (yellow) and the MC simulated distributions (red) are displayed for comparison in Fig. 6.5. For the MC simulation, 1.14 nm (average of 20 double occupation cells measured) is used as the diameter of the potential well. And the best fit for all four samples is achieved by setting $q = 0.26e_0$.

Deposition Time	2 min	6 min	15 min	30 min
Average Occupation λ	0.058	0.235	0.497	1.22

Table 6.3: Deposition time and average occupation in one moiré unit cell of the samples presented in Fig. 6.5.

Cs (3.89 eV [80]) has a lower ionization energy than K (4.34 eV [80]), hence easier to lose the s electron. However, the analysis of the STM data suggests a higher charge transfer of K than Cs when adsorbed on hBN/Ru(0001). At the moment, I lack a sound explanation for this contradiction. I venture three possible directions for further investigation, which I list in the summary and outlook chapter (Chap. 8).

6.2 Alkali metal adsorption on hBN/Ir(111) at room temperature

Now I present the results of Cs/K adsorption on hBN/Ir(111). Fig. 6.7a presents a large STM image of the sample after 1 minute deposition of Cs with 5.0 A through the dispenser. Quite distinctive from the preferred adsorption in valley regions of hBN/Ru(0001), here Cs atoms (bright protrusions in the image) always reside in the hill regions of the hBN/Ir(111) moiré unit cell.

I attribute this preferred adsorption in the hill regions to the work function modulation in the moiré unit cell. The local work function is 0.5 eV larger in the hill regions than in the valley regions [23]. Assuming that the ionization energy does not depend on the details of the substrate electronic structure, charge transfer in the area where the local work function is large is energetically favored [81].

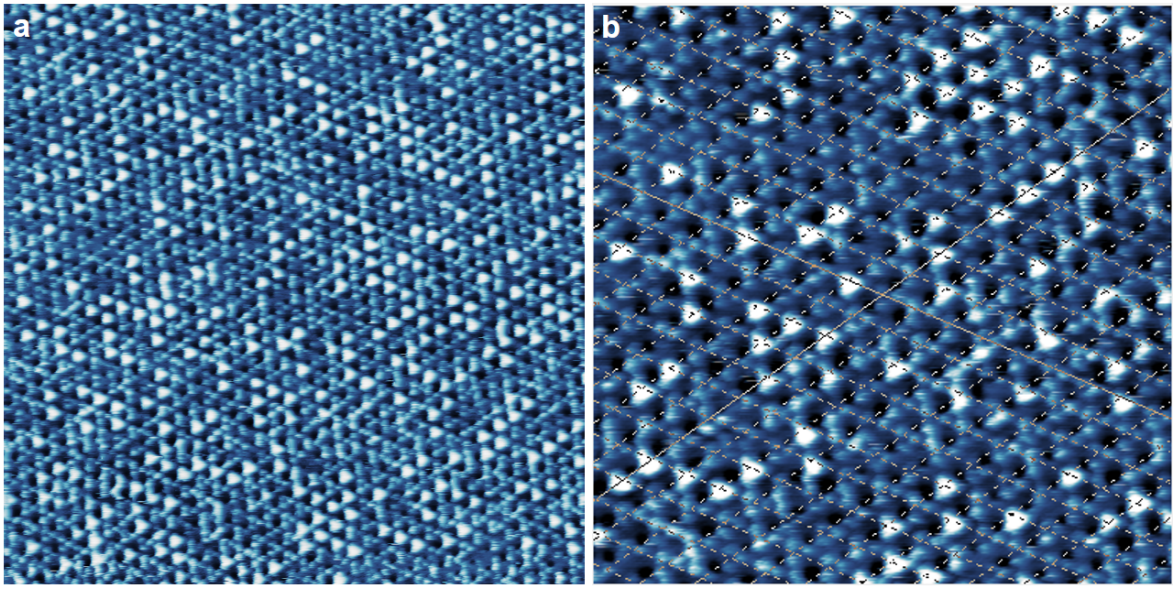

Figure 6.7: Cs adsorption on hBN/Ir(111). (a) 100×100 nm^2, (b) 50×50 nm^2. $U_\mathrm{b} = -1.6$V, $I_\mathrm{tunneling} = 20$ pA.

A closer look (Fig. 6.7b) reveals that all the Cs adatoms sit on a hexagonal lattice (the dashed mesh in the image). As described in Sec. 4, there are two hill regions in one moiré unit cell, forming two hexagonal sublattices. The fact that almost all the Cs atoms are found in only one of these two sublattices indicates that the adsorption energy in one of the hill regions is much larger than the other (compared to $k_\mathrm{B}T = 25.9$ meV). In rare cases, Cs atoms sit in the other hill regions (red circles in Fig. 6.7a). For convenience, in the rest of the thesis, the dominant hill region is called "good

hill" (GH), and the minor one is called "bad hill" (BH). Clearly, the GH and BH are the best and the second best adsorption sites within one moiré unit cell. In other words, GH and BH have the highest and the second highest adsorption energy. After examining over 0.1 µm^2 on the sample (over 20000 moiré unit cells), I obtain the ratio between the Cs atoms adsorbing in GH and BH is around 400. Since the Cs concentration is quite low (around 0.3 Cs per moiré unit cell), the interatomic interaction is ignorable. Hence I can estimate the adsorption energy difference (ΔE) between the two hill regions:

$$\frac{p_1}{p_2} = e^{\Delta E/k_\mathrm{B}T} \approx 400,$$

yielding $\Delta E \approx 155$ meV.

To systematically study the adsorption behavior, I prepared a series of samples with different Cs deposition time. Fig. 6.8a-c present the STM images obtained from three samples with 5 minutes, 10 minutes, and 15 minutes of Cs deposition (5.2 A). The majority of the Cs atoms sit at the GHs, until almost all these regions are occupied. I obtain the occupation rate of the GH regions by counting over 1000 moiré cells, and they are listed in Tab. 6.4.

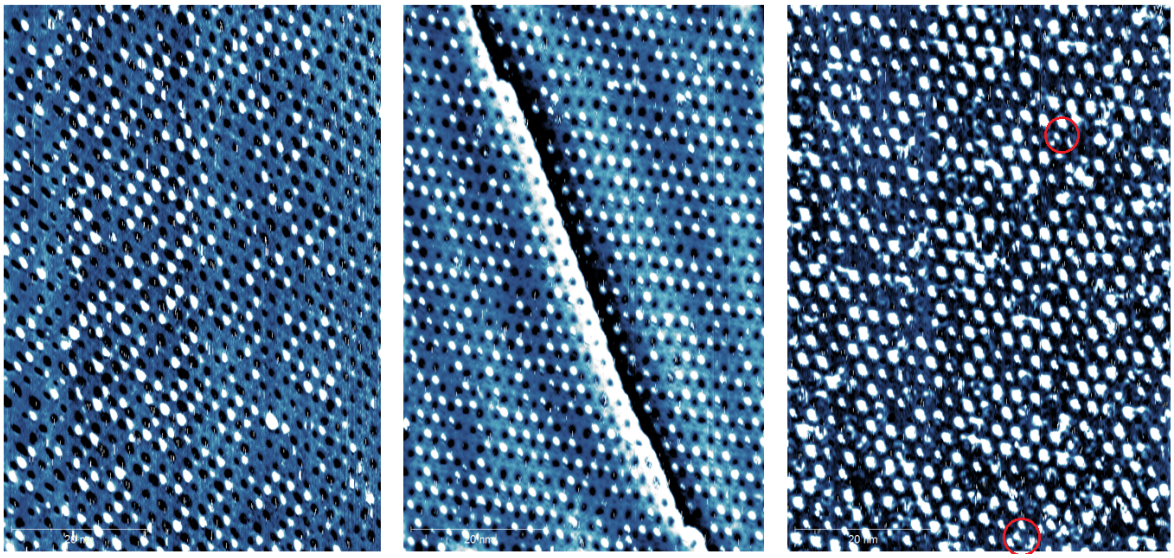

Figure 6.8: hBN/Ir(111) with different amount of Cs adsorption. Cs deposition time: (a) 5 minutes, $U_\mathrm{b} = -2.0$V, $I_\mathrm{tunneling} = 10$ pA. (b) 10 minutes, $U_\mathrm{b} = -1.5$V, $I_\mathrm{tunneling} = 20$ pA (c) 15 minutes, $U_\mathrm{b} = -1.5$V, $I_\mathrm{tunneling} = 20$ pA. (a)-(c) 40×60 nm^2.

Deposition Time	5 min	10 min	15 min
Average Occupation θ	0.35	0.66	0.95

Table 6.4: Deposition time and average occupation in one moiré unit cell of the samples presented in Fig. 6.8.

Another apparent observation from the STM images in Fig. 6.8 is that the bright protrusions do not have a uniform apparent size. This observation raises the question about the nature of

these bright protrusions. Are they individual Cs atoms appearing differently, or Cs clusters/islands with different numbers of atoms thus having different sizes? To answer this question, I calculate the amount of Cs deposition from the observed Cs adsorption by different assumptions, and then compare them with the deposition time. The three samples presented in Fig. 6.8 are prepared with 5, 10, and 15 minutes of Cs deposition. Thus the correct assumption should yield a linear relationship with the Cs deposition among these three samples.

Assuming one GH is occupied by $i-1$ Cs atoms, the adsorption energy of the ith atom to occupy the same GH is ϵ_i. Apparently, with increasing i, ϵ_i decreases due to the repulsive interaction between the Cs atoms. At some point, $\epsilon_n > 0$, while $\epsilon_{n+1} < 0$. The $(n+1)$th atom can no longer adsorb in this adsorption site. Then n is the maximum occupation number. Beside the maximum occupation number, there is another unknown factor: the behavior of this $(n+1)$th atom. When the energy barrier between two neighboring hill regions is low, the $(n+1)$th atom could diffuse into a neighboring empty or partially occupied adsorption site. The alternative behavior is simply desorption. One should notice that if the $(n+1)$th Cs atom desorbs (desorption model), instead of diffuses (diffusion model), the amount of Cs observed by STM measurement is then lower than the amount deposited.

For the desorption model, I perform a simple simulation. I start with a large number (10^6 to ensure accuracy) of empty cells. For each Cs atom, one cell is selected randomly. If the selected cell is occupied by less than n atoms, then the Cs atom goes in, adding 1 to the occupation number of this cell. If the occupation number of the selected cell already reaches n, then the simulation directly goes on to the next atom, simulating the desorption of this atom. The atoms are added to the cells one by one, and once the occupation rate of all the cells reached the θ values observed in the STM images (Tab. 6.4), the simulation stops. The total number of Cs atoms involved, including the desorbed ones, are taken as the amount of Cs deposition. The deposition density (λ) is then the amount of Cs deposition normalized by the number of cells.

The simulation reveals that, within the desorption model, the maximum occupation number n is actually irrelevant: the Cs deposition density λ for the three samples presented in Fig. 6.8 are 0.42, 1.10, and 2.90 monolayer for all n (blue dots and line in Fig. 6.9a). One monolayer (ML) is defined as the density of all GHs occupied by 1 Cs atom.

To understand this n independence, one simply needs to realize the similarity between this desorption model and the Poisson process. The only difference between the simulation process described in the last paragraph and a Poisson process is that when a Cs atom is selected to a full cell, the occupation number of this cell does not increase. Then all the $i \leq n$ terms in the Poisson distribution (Eq. 6.1) can be treated as n occupation. Adding up all these p_i in the Poisson distribution with $i \leq n$, and using the sum as the new p_n, I end up with the same distribution as the simulated one. Since the occupation rate θ observed in the STM images is used, in other words, the un-occupation rate $(1-\theta)$, as the standard, the problem simplifies to the calculation of λ from $p_0 = 1-\theta$ for the three samples. The λ values calculated in this way are 0.42, 1.10, and 2.90, same as the values I obtained from the simulation.

In the last three paragraphs, I described two methods, within the desorption model, to obtain the amount of Cs deposition from the Cs adsorption density observed in STM. The dependence on

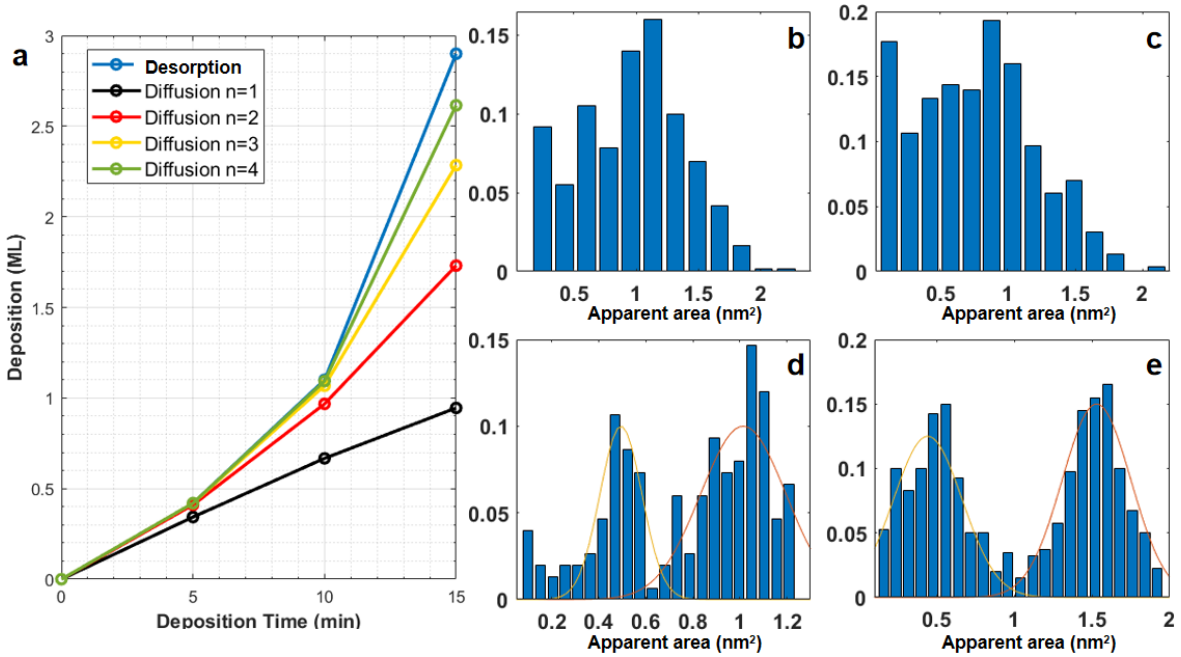

Figure 6.9: (a) Simulated deposition densities of the 5-, 10-, and 15-minute samples, based on different kinetic models. (b) Apparent size distribution collected on Fig. 6.7, and Fig. 6.8 a-c.

the deposition time (blue dots and line in Fig. 6.9a) is far from linear.

Now I turn to the diffusion model. One realizes that the final state of the previous simulation performed for the desorption model also applies for the diffusion model: The occupation rate of the cells is θ, and the maximum occupation n standard is met. The only atoms needed to be counted are the atoms that are in the cells, i.e. excluding the desorbed ones. The simulation results (λ) for different n are plotted in Fig. 6.9a ($n = 1$ black, $n = 2$ red, $n = 3$ yellow, $n = 4$ green).

Since in the diffusion model, the desorbed Cs atoms are excluded, while in the desorption model, I include them, the difference between the data points in these two model is the density of Cs desorption. With increasing n, each adsorption site can accommodate more Cs atoms, i.e. less desorption, thus the curve moves closer to the desorption model curve (blue). Comparing all the curves, I find that only the $n = 1$ curve in the diffusion model is close to a linear relation. Thus I conclude that the bright protrusions in the STM images with different apparent sizes are all individual single Cs atoms.

Before moving on to the next argument supporting the single-occupation model, I discuss two more points about the previously mentioned models. (i) The θ values in Tab. 6.4 only include the Cs atoms occupying the GHs. One can observe a minority of adsorbed Cs atoms sit in BHs. On the 5- and 10-minute-deposition samples, the ratio is below 1%, thus ignorable. However, on the 15-minute-deposition sample, though difficult to obtain a accurate coverage, the amount of Cs atoms which do not adsorb in GHs shall be added back when calculating the Cs depositions. In the fore-mentioned calculation, they are not included, which could account for the "bend-down" of the $n = 1$ curve. (ii) In the diffusion model, there is actually a hidden assumption, i.e. the infinite diffusion

length. The newly added Cs atoms can always find the partly filled cells. And the fact that on the 15-minute-deposition sample, even though some cells are still empty, some Cs atoms still absorb in the BH regions suggests that the diffusion length is finite.

To explore the nature of the bright protrusions in the STM images from another angle, I obtain the size distribution (apparent area) of the bright protrusions in the three STM images in Fig. 6.7 and Fig. 6.8 by WSxM software [82] (Fig. 6.9b-e). One can see that the apparent areas of the bright protrusions in Fig. 6.7 are quite mono-dispersed. The distributions from the 10 and 15 minutes deposition images (Fig. 6.9d and e) clearly demonstrate a double-peak feature. I use two Gaussian curves to fit the peaks, and use the areas under the Gaussian curves as the number of the two different kinds of protrusions. With the multi-occupation assumption, the peak with small/large apparent areas corresponds to the adsorption sites accommodating one/two Cs atom(s). Combining the occupation rate θ, I can calculate the ratio of the empty, single occupation, and double occupation cells are 35%, 17.6%, and 47.3% for the 10-minute-deposition sample, and 7%, 35.6%, and 57.4% for the 15-minute-deposition sample. On the 10-minute-deposition sample, there are fewer single occupation cells than both empty and double occupation cells. This distribution can only happen when there is attractive interaction between the adsorbates, which clearly does not apply to the Cs atoms. Thus based on this observation of the 10-minute-deposition sample, I conclude that the multi-occupation assumption does not stand. This is another evidence to support the single-occupation model.

Fig. 6.10a and b present STM images with almost 1 ML Cs adsorption, with 5.6 A dispenser current for 5 minutes. I define 1 ML as one Cs atom in one moiré unit cell. The adsorbed Cs atoms occupy almost all GHs, and form a rather good hexagonal lattice. In Fig. 6.10a, one can also observe some intercalation at the Ir(111) step edges. Similar to the case with less Cs adsorption, occasional Cs adsorption on BHs can also be observed (red circles in Fig. 6.10b).

Fig. 6.10c and d present STM images with 10 minutes of Cs deposition (5.6 A dispenser current). Due to the doubled deposition time, the adsorption density shall be twice the density observed in Fig. 6.10a and b (2 ML). Some inhomogeneity is present on the surface. In some areas, for example, the bottom two third of Fig. 6.10c, and the triangular area in the center of the Fig. 6.10d, the adsorbed Cs atoms still form a simple hexagonal lattice. They occupy all the GHs, and occasionally the BHs. When scanning with positive bias voltage, the Cs atoms in the neighboring GHs and BHs cannot be imaged individually. The Cs atoms in the BHs, together with the neighboring three Cs atoms in the GHs, display a "Y" shaped bright protrusion in the STM image (red circles in Fig. 6.10c). In this type of areas, the adsorption density is still near 1 ML.

In other areas (top part of Fig. 6.10c, and outside the triangular area in Fig. 6.10d), the additional Cs atoms reduce the degree of ordering. The template of the hBN/Ir(111) moiré pattern fails to arrange all the adsorbed Cs atoms into an ordered structure. The surface appears amorphous. Similar to the 5-minute-deposition sample (Fig. 6.10a), I also observed occasional intercalation (not shown).

In Fig. 6.11, I present the STM images of hBN/Ir(111) with different amount of K adsorption (4.0 A through the dispenser). The behavior is very similar to Cs adsorption. The two hill regions in the moiré unit cell are preferred adsorption sites. The majority of the adsorbed K atoms occupy

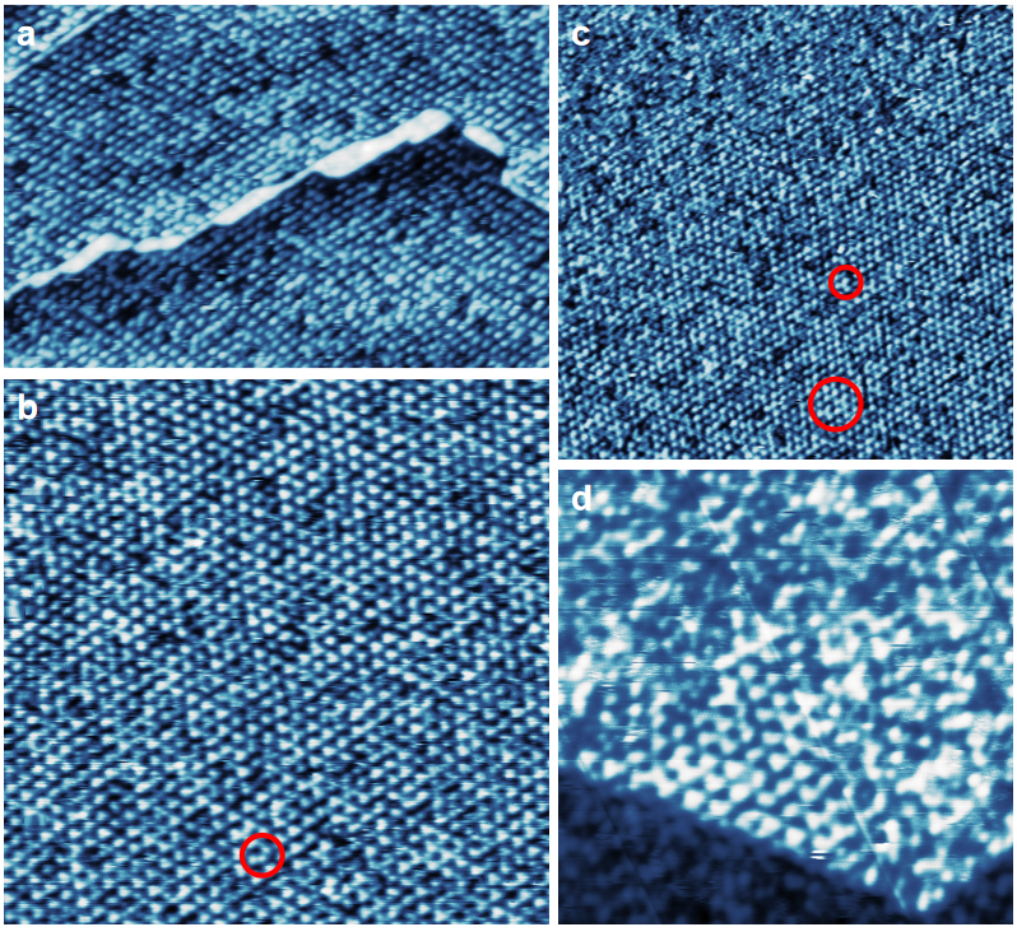

Figure 6.10: hBN/Ir(111) with more Cs adsorption than in Fig. 6.8. Dispenser current 5.6 A. Cs deposition time: (a) and (b) 5 minutes, $U_{\mathrm{b}} = -2.0$V, $I_{\mathrm{tunneling}} = 10$ pA. (c) and (d) 10 minutes, $U_{\mathrm{b}} = -1.5$V, $I_{\mathrm{tunneling}} = 20$ pA. (a) 100×160 nm^2, (b) 100×100 nm^2, (c) 150×150 nm^2, (d) 55×55 nm^2.

the GHs, and the minority the BHs. With increasing K adsorption, more and more hill regions are occupied. And at some point, when almost all the GHs are occupied, intercalation starts.

So far, I have discussed the Cs (K) adsorption on hBN/Ir(111) in this section. Based on the observations, I extract the adsorption energy diagram as illustrated in Fig. 6.12a. There are two preferred adsorption sites in one moiré unit cell, i.e. the two hill regions. The Cs atoms prefer one (GH) more than the other (BH): $E_1^G > E_1^B$. After all the GHs are occupied, additional Cs atoms adsorb in the BHs. This indicates that accommodating two Cs atoms in the GH has an higher energy then distributing these two Cs atoms in GH and BH separately: $E_2^G < E_1^B$.

For comparison, I illustrate the energy diagram of the Cs (K) adsorption on hBN/Ru(0001) in Fig. 6.12b. In contrast to hBN/Ir(111), there is only one adsorption site, i.e. the valley region, in one moiré unit cell. The valley regions can accommodate multiple alkali metal atoms, hence the multi energy levels in Fig. 6.12b. The maximum number of Cs atoms observed in one valley is 7, and 5 for K. This two numbers are not necessarily the maximal occupation numbers. The experiments of

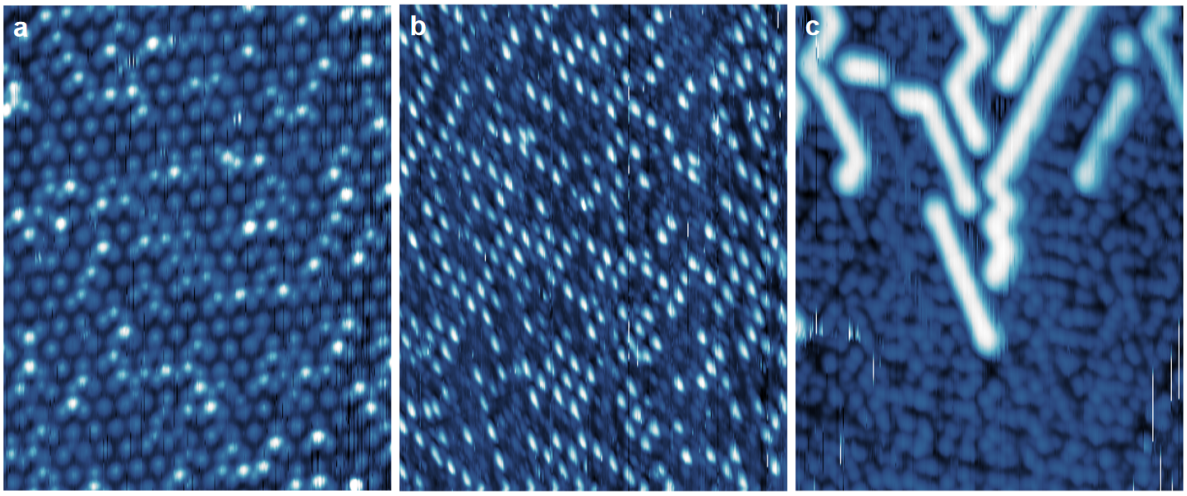

Figure 6.11: K adsorption on hBN/Ir(111). K deposition time: (a) 2 minutes, (b) 5 minutes, (c) 10 minutes. 48×60 nm^2 $U_{\mathrm{b}} = 1.8$V, $I_{\mathrm{tunneling}} = 10$ pA.

alkali metal adsorption on the two different surfaces, hBN/Ru(0001) and hBN/Ir(111), thus reveal a fundamentally different adsorption behavior. This difference originates from the interaction of hBN and the underlying TM substrate.

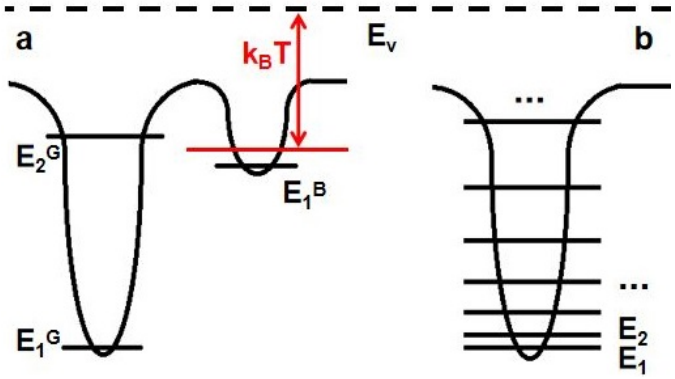

Figure 6.12: Energy diagrams of Cs/K adsorption on (a) hBN/Ir(111), and (b) hBN/Ru(0001).

6.3 Cs adsorption on hBN/Ir(111) at elevated temperature

The last two sections both discussed the adsorption of alkali metals on hBN/TM at room temperature. On hBN/Ir(111), there are two preferred adsorption sites in one moiré unit cell, i.e. the two hill regions (Fig. 6.12a). Intuitively, the structure with the lowest energy with 2 ML Cs adsorption is a honeycomb lattice (a bi-atomic basis on a hexagonal lattice). However, the Cs adsorption morphology descends into disorder when the adsorption density increase over 1 ML (Fig. 6.10c and d).

To achieve an ordered Cs honeycomb structure, I prepare the sample by keeping the substrate hot during Cs deposition. The elevated temperature enhances the diffusion of Cs atoms. From

the kinetic point of view, the thermal energy k_BT is increased. When k_BT is comparable to the adsorption energy, and $E' < k_BT < E_1^B$, E' being the adsorption energy of the Cs atom at the third best adsorption site, saturation of the Cs adsorption is reached when both the best two adsorption sites, i.e. the two hill regions, are occupied.

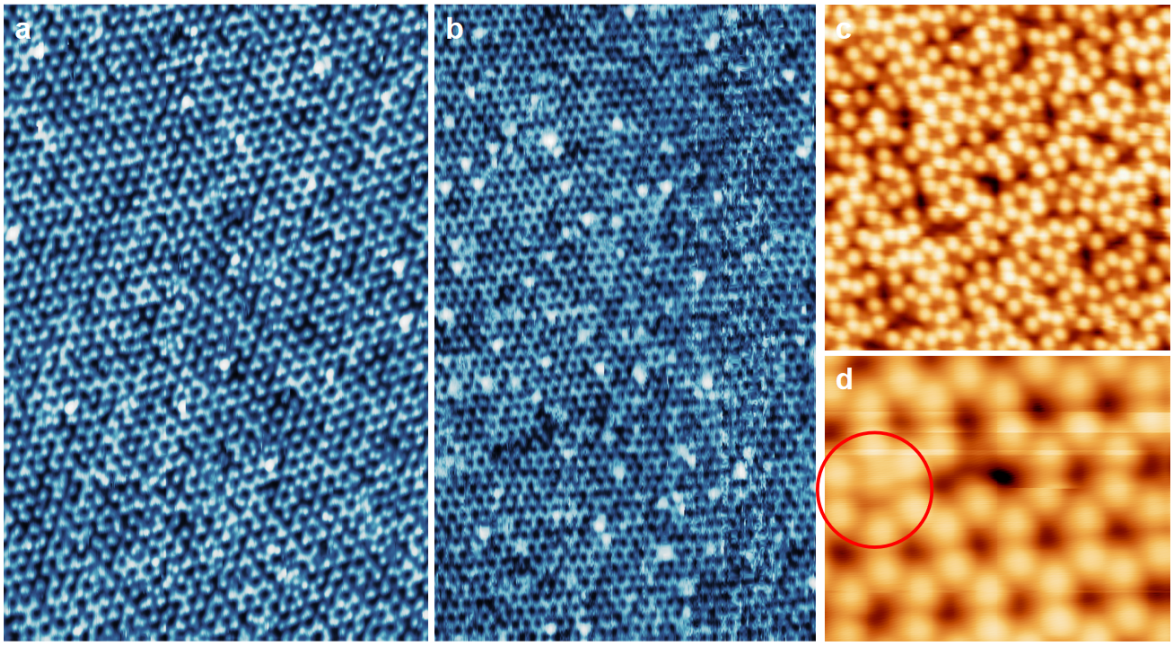

Figure 6.13: Cs adsorption on hBN/Ir(111), with sample kept at 400 °C during deposition. (a) 15 minutes deposition, 120×80 nm^2, $U_b = 2.4$V, $I_{tunneling} = 20$ pA; (b) 25 minutes deposition, 150×90 nm^2, $U_b = 2.4$V, $I_{tunneling} = 20$ pA. (c) 50×50 nm^2, $U_b = 3.0$V, $I_{tunneling} = 50$ pA; (d) 15×10 nm^2, $U_b = 3.0$V, $I_{tunneling} = 50$ pA. (c) and (d) are measured at 5 K, with LTSTM cologne.

The sample temperature is carefully controlled and tested, and I obtain the most ordered structure with the deposition temperature around 400 °C (Fig. 6.13). Fig. 6.13a presents the surface of hBN/Ir(111) after 15 minutes of Cs deposition (5.6 A through the dispenser). All the GHs and part of the BHs are occupied. Thus the STM image presents honeycomb structure in some areas, while hexagonal in some others. Another 10 minutes of Cs deposition fills almost all the BHs, and almost the whole surface is covered with Cs atoms arranged in a honeycomb lattice. It is obvious that a perfectly ordered honeycomb lattice is not yet achieved. Defects such as distortions, missing and extra Cs atoms still exist on the surface (Fig. 6.13c, d).

The defects originates from the tight temperature window for the honeycomb structure. The co-existence of the local extra and missing Cs atoms suggest that the difference between E_1^B and E' is very small. Additional Cs atoms at the center of the six-Cs-atom hexagon (red circle in Fig. 6.13d). Their appearance are quite rare for a quantitative estimation of the relative adsorption energy. One should also notice that defects in the hBN sheet or the underlying substrate could also lead to defects of the adsorbed Cs honeycomb structure.

Photoemission measurements have been conducted on the $Cs_{honeycomb}$/hBN/Ir(111) sample. The ARPES mapping on this sample is presented in Fig. 6.14a. The hBN σ-bands, degenerate at the

Γ-point, split into two branches towards higher binding energy. The bottom of the π-band is found at the Γ-point. Its top is at the K point, where this band also constitutes the valence band maximum (VBM). The Ir bands are visible in the low-binding-energy range (around 1 eV). This band structure resembles the band structure of pristine hBN/Ir(111) (not shown, similar to that in Ref. [75]). This similarity indicates a weak influence of the adsorbed Cs on the hBN and Ir electronic structure.

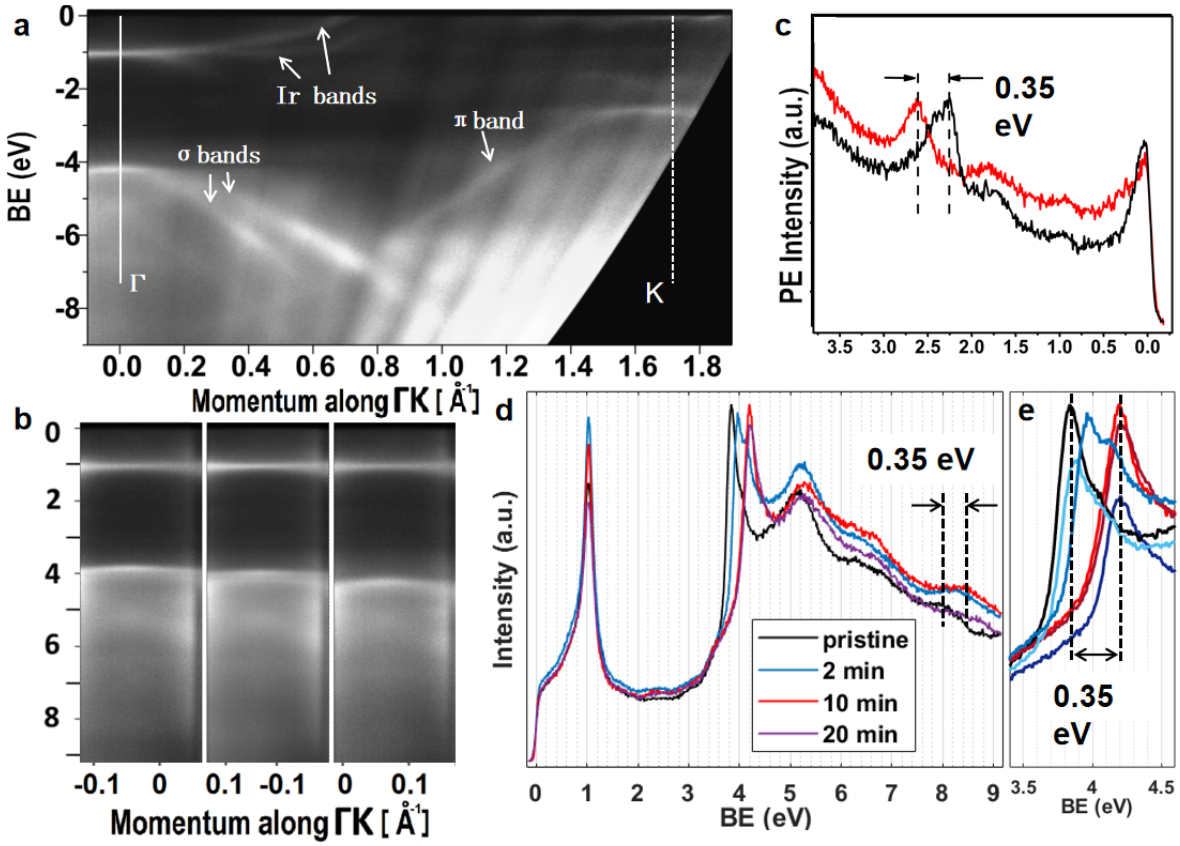

Figure 6.14: (a) ARPES measurement results on $Cs_{honeycomb}$/hBN/Ir(111). (b) PE intensity mapping around the Γ-point on pristine hBN/Ir(111), 2 minutes Cs deposition, 10 minutes Cs deposition (left to right). (c) PE intensity at the K-point versus BE measured on pristine hBN/Ir(111) (black) and $Cs_{honeycomb}$/hBN/Ir(111) (red). blue line is measured on an Cs intercalation sample discussed in the next chapter. (d) PE intensity at the Γ-point vs BE measured on pristine hBN/Ir(111), and after different amount of Cs deposition (see the legend in the image).

A careful comparison between the ARPES results on $Cs_{honeycomb}$/hBN/Ir(111) and pristine hBN/Ir(111) reveals a small shift of the hBN bands. Fig. 6.14b presents the ARPES mapping around the Γ-point with increasing Cs deposition (left to right). A gradual shift of hBN's σ-bands is observed. Fig. 6.14c and d extract the PE intensity at the K- and Γ-point as a function of BE. At the Γ-point, the top of the σ-bands is at around 4 eV, and the bottom of the π- band is at around 8 eV. For a clearer view, Fig. 6.14e zooms in around 4 eV for the exact position of the top of the σ-bands. Without Cs adsorption, the peak locates at 3.85 eV in BE (black curve). The three blue curves are from the sample after 1 minute, 2 minutes and 5 minutes (light to dark) of Cs deposition. The peak

gradually shifts to higher BE. The width of the peak broadens due to the inhomogeneous Cs concentration on the surface. A double-peak feature is observed in the 2-minute curve, which probably originates from some ordered superstructure of Cs at certain concentration. After 10 minutes of deposition, the peak shift to 4.21 eV in BE (purple curve). Even more Cs deposition no longer changes the location of the peak (red). This stability indicates the saturation of Cs adsorption. According to the STM observation, this saturated adsorption corresponds to the honeycomb lattice of the Cs atoms. Comparing the black and red curves, I measure a shift of $\Delta E = 0.35$ eV at the top of the σ-bands.

The same ΔE can be measured at the bottom of the π-band at the Γ-point near 8 eV (black dashed lines in Fig. 6.14d) and at the top of the π-band at the K-point (Fig. 6.14c). In absolute numbers, the VBM shifts from 2.26 eV for hBN/Ir to 2.61 eV for $Cs_{honeycomb}$/hBN/Ir(111). The occurrence of the same ΔE of both σ- and π-bands at different positions in the Brillouin zone suggests a rigid shift of the band structure. In contrast, the iridium band at the Γ-point stays at 1.0 eV before and after Cs adsorption (Fig. 6.14d).

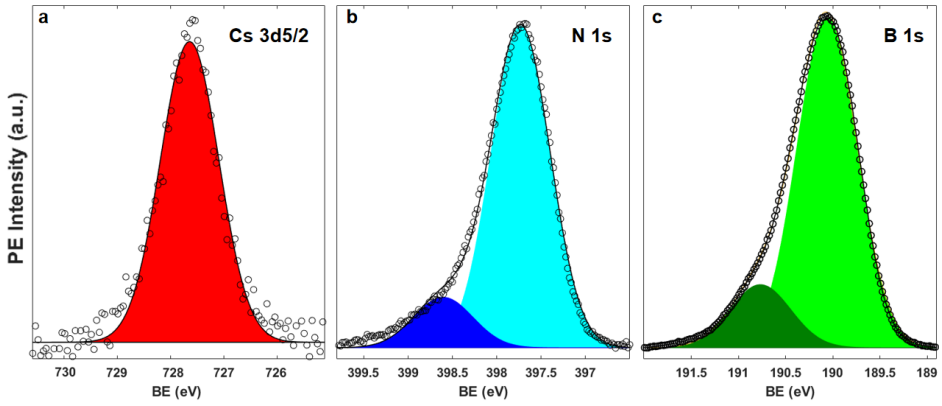

Figure 6.15: XPS results of $Cs_{honeycomb}$/hBN/Ir(111): (a) Cs $3d_{5/2}$ spectrum measured with $h\nu = 900$ eV. (b) N 1s spectrum measured with $h\nu = 600$ eV. (c) B 1s spectrum measured with $h\nu = 300$ eV.

The XPS measurements collect the PE intensity from the core levels. Fig. 6.15a presents the Cs $3d_{5/2}$ spectrum with the peak at 727.7 eV in BE. The fact that the Cs $3d_{5/2}$ spectrum consists of only one component indicates that the Cs atoms adsorbed at the GHs and BHs are very similar electronically. The N 1s and B 1s spectra are presented in Fig. 6.15b and c. For N 1s, the dominating component (N_0) is found at 397.7 eV, and a small shoulder (N_1) appears at 398.6 eV. Only minor changes are present when comparing this double-peak spectrum to the N 1s spectrum measured on pristine hBN/Ir(111) (not shown, same as Ref. [26]). Thus I use the same assignment as pristine hBN/Ir(111): the N_0 corresponds to the hill regions in the moiré unit cell, and N_1 to the valley regions. The same resemblance is also observed for the B 1s spectrum. The position and the width of all the components in N 1s and B 1s spectra are listed in Tab. 6.5, in comparison to the ones measured on pristine hBN/Ir(111).

Comparing the precise locations of the N 1s (B 1s) components measured on pristine hBN/Ir(111) and $Cs_{honeycomb}$/hBN/Ir(111), I measured a small shift of the core levels. The the N 1s (both N_0 and N_1) peak shifts approximately 0.15 eV to higher BE. And the shift of the B 1s (both B_0 and B_1)

	Position	FWHM	P^H	f^H	n	h(Å)
Cs $3d_{5/2}$	727.7	1.29	0.97	0.94	2	6.56
N_0	397.73	0.79	0.63	0.70	1	3.62
N_1	398.60	0.79	0.12	0.55	1	2.48
B_0	190.02	0.76	0.66	0.54	1	3.69
B_1	190.80	0.76	0.08	0.73	1	2.40
N_0	397.58	0.79	0.68	0.40	1	3.72
N_1	398.46	0.79	0.00	0.92	1	2.22
B_0	189.92	0.76	0.67	0.37	1	3.70
B_1	190.72	0.76	-0.02	0.64	1	2.17

Table 6.5: Position and width of all N 1s, B 1s, Cs $3d_{5/2}$ components measured in XPS spectra. Fitting parameters for XSW results on $Cs_{honeycomb}$/hBN/Ir(111). Errors: $\Delta P^H = \pm 0.01$, $\Delta f^H = \pm 0.04$, $\Delta h = \pm 0.02$ Å.

peak is approximately 0.09 eV. Compared with the shift of the valence bands, the core levels endure smaller shifts. One possible explanation of this smaller shift is that the N 1s and B 1s orbits reside much deeper in the atomic structure and thus are screened by the electrons in the outer orbitals.

The $Cs_{honeycomb}$/hBN/Ir(111) sample is also characterized by XSW measurement for structural analysis. The results of the Cs $3d_{5/2}$ spectrum, and the four components in N 1s and B 1s are presented in Fig. 6.16a. The circles indicate the measured PE intensity, and the lines are the fitting results. The N 1s and B 1s curves are very similar to the ones measured on pristine hBN/Ir(111). The optimized fitting parameters P^H and f^H are summarized in Tab. 6.5. The adsorption height of each species is calculated using Eq. 3.36. Here d is the distance between atomic layers of Ir(111) (2.217 Å[83]). Based on the stacking relation between Cs and hBN, I assign the values of n, and calculate the heights. To obtain a sense of the distance among Cs, hBN and Ir(111) substrate, a sketch drawn to scale is presented in Fig. 6.16b. For Ir (gray), the nearest-neighbor (nn) distance ($d_{Ir,nn} = 2.71$ Å[83]) is used. For N (blue) and B (green) the van der Waals diameters ($d_{N,vdW} = 3.10$ Å, $d_{B,vdW} = 3.84$ Å[84]) are used. For Cs (pink), I use the ionic diameter ($d_{Cs,ion} = 3.48$ Å[85]).

Comparing the N 1s and B 1s components in $Cs_{honeycomb}$/hBN/Ir(111) and pristine hBN/Ir(111), some small changes in the hBN corrugation geometry are detected. The height of the hills, where the Cs directly adsorbed on, does not change, while the valleys rises. These observations on the corrugation geometry are confirmed by DFT simulation (see below).

From the PE measurements, I calculate the charge density using a simple parallel capacitor model. Treating the Cs adsorption (positive) and the Ir(111) crystal (negative) as the two contacts of the capacitor, a static electric field exists between them. The hBN sheet locates in this field, thus having a higher electric potential than the Ir(111) substrate (grounded). This elevated electric potential leads to the shift of the hBN electronic structure. Effectively, the adsorbed Cs ions act as a top gate for the hBN sheet. Within this simple model, the relation between the charge density σ and the

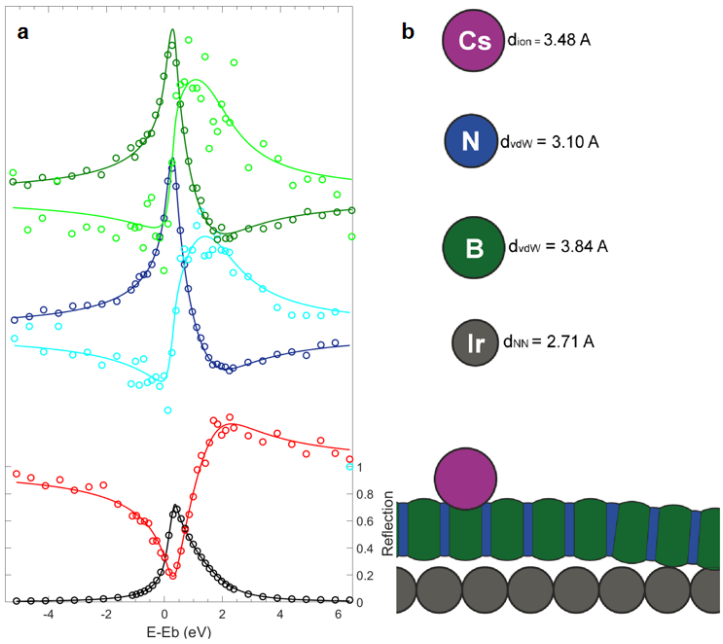

Figure 6.16: (a) XSW results for Cs $3d_{5/2}$ (red), the two components of N 1s (N_0 dark blue, N_1 light blue) and B 1s (B_0 dark green, B_1 light green) in $Cs_{honeycomb}$/hBN/Ir(111). The measured intensities are presented in circles, and the lines are from the optimized fitting to Eq. 3.36. (b) Relative position of adsorbed Cs, hBN, and the first layer of iridium atoms in $Cs_{honeycomb}$/hBN/Ir(111); the sphere sizes indicate the van der Waals radius, ionic radius or nearest neighbor distance, and relative height extracted from XSW results.

adsorption height of hBN h is:

$$\sigma = \epsilon_0 E = \epsilon_0 \frac{V}{h}.$$

Here E is the strength of the electric field, and V the potential difference between the hBN sheet and Ir(111) substrate. For V, I use the shift of the hBN bands measured with ARPES (0.35 eV, Fig. 6.14), rather than the BE shift of the core levels (Fig. 6.15). The core levels locate deep in the atomic structure, and the BE shift are reduced by the screening of the electrons in the shallower orbitals.

On the other hand, two Cs ions adsorb in one moiré unit cell, thus the charge density is

$$\sigma = \frac{Q}{A} = \frac{2q}{a_{\text{moiré}}^2 \sin 60°},$$

where q is the charge of a single Cs atom, and $a_{\text{moiré}}$ the lattice constant of the moiré superlattice. Here I do not distinguish the Cs atoms adsorbed in GHs and BHs: Since the XPS measurement (Fig. 6.15a) only reveals one component, the electronic properties of these two types of Cs atoms are very similar. Combining the two equations above, I obtain:

$$q = \frac{\epsilon_0 V a_{\text{moiré}}^2 \sin 60°}{2h} = 3.23 \times 10^{-20}\text{C} \approx 0.20 e_0.$$

DFT simulation of $Cs_{honeycomb}$/hBN/Ir(111)

The DFT simulation is carried out by N. Atodiresei et al. (Forschungszentrum Jülich). Two Cs atoms are included in a supercell of (12) unit cells of hBN and (11 × 11) unit cells of Ir(111) (three atomic layers). The initial state of hBN/Ir(111) is the same as the DFT simulation reported in Ref. [26]. The positions of the B, N, Cs, and the top layer Ir atoms are relaxed. The final relaxed positions of the Cs atoms are presented in Fig. 6.17a and b.

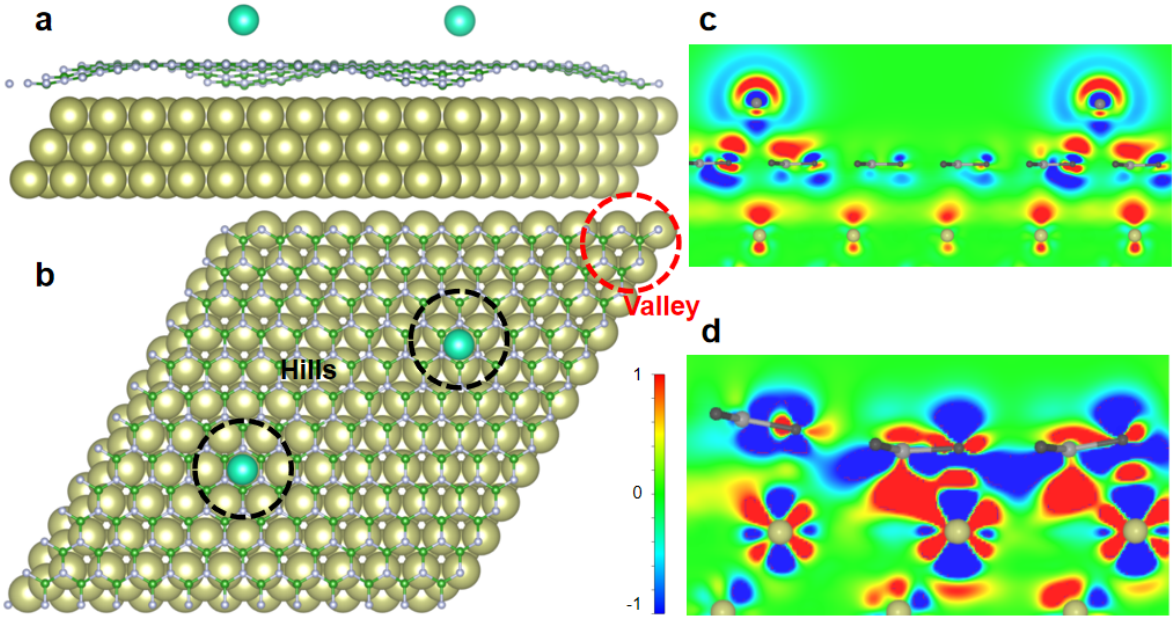

Figure 6.17: (a) Side and (b) top views of the moiré unit cell of $Cs_{honeycomb}$/hBN/Ir(111). Ir, B, N, and Cs atoms are indicated by yellow, green, gray and cyan spheres. The hill and valley regions of the moiré unit cell are labeled with black and red circles. Charge rearrangement mapping in the (c) hill and (d) valley regions. Warm/cold color indicates negative charge accumulation/depletion.

The two Cs atoms sit in the center of two B-N rings in the two hill regions. Compared with Fig. 2.5 in Sec. 2.2.2, the corrugation geometry of hBN is conserved after Cs adsorption. Following the analysis procedure in Ref. [26], I categorize B/N atoms into two groups: 21 B/N atoms for the valley region, and 123 for the hill regions. The average B/N-Ir(111) distance in each group is defined as the height of hBN in the corresponding regions: 2.50 Å in the valley regions and 3.40 Å in the hill regions. The calculated height of hBN in pristine hBN/Ir(111) is 2.32 Å in the valley regions and 3.40 Å in the hill regions. The DFT simulation reveal the stability of hBN in the hill regions and the small height increase in the valley regions, which agrees with the XSW analysis results.

In Fig. 6.17c and d, I present the charge rearrangement mapping in the hill and valley regions. In the hill regions (Fig. 6.17c), the electron depletion of N atoms and Cs atoms, and the electron accumulation between them indicates chemical bonding between Cs and N atoms. In addition, the first layer Ir atoms are clearly negatively charged, which supports my modeling of parallel capacitor. In the valley regions (Fig. 6.17d), the charge rearrangement is very similar to the case of pristine hBN/Ir(111) (Fig. 2.5d): N atoms still bind to the Ir atom below.

Comparison between honeycomb lattice and hexagonal lattice

In $Cs_{honeycomb}$/hBN/Ir(111), two Cs atoms adsorb in one moiré unit cell. For the same adsorption density, M. Petrović *et al.* report a different adsorption morphology of Cs on gr/Ir(111) [86]. The adsorbed Cs atoms form a simple hexagonal lattice on gr/Ir(111). In Cs/gr/Ir(111) system, one moiré cell just has one preferred adsorption site, i.e. the only hill region. Thus with density higher than 1ML, the adsorbed Cs atoms do not follow the periodicity of the moiré pattern. Due to the interatomic Coulomb repulsion between each other, they form a simple hexagonal lattice.

In the Cs/hBN/Ir(111) system, the repulsive Coulomb interaction between the Cs atoms is not included in the discussion. So far I have only considered the templating effect of the moiré pattern, and I can account for the honeycomb lattice of the adsorbed Cs atoms, which indicates that the spatially modulated adsorption is the dominant factor. However, due to the similarity between Cs/hBN/Ir(111) and Cs/gr/Ir(111) and the rather distinguished structures of the Cs adsorption in them, it is worthwhile to have a further discussion. For this, I calculate the total energy, including the adsorption energy and Coulomb energy, of one Cs atom, in the observed honeycomb lattice on hBN/Ir(111), and compare it with the total energy of a virtual simple hexagonal lattice with the same Cs density.

First I address the interatomic Coulomb energy. The electric energy between two Cs atoms (indicated by the indices m and n) is

$$E_{mn} = \frac{q^2}{4\pi\epsilon_0 r_{mn}} e^{-r_{mn}/\lambda}.$$

Here q is the charge of the Cs atoms, r_{mn} the distance between the two atoms, and λ the screening length. Here I assume all Cs atoms have the same amount of charge q. The distance in-plane is in the range of the moiré lattice parameters (around 3 nm), while the height difference is less than the moiré corrugation (< 2 Å). Thus for r_{mn}, I only consider the distance parallel to the Ir(111) surface. Here I include the exponential screening term. For Cs/gr/Ir(111), the electron density rearranges in graphene and $\lambda = 0.66$ nm [86]. Moreover, if the bare Coulomb energy is used, the total interatomic energy does not converge (see later discussion). When $\lambda = +\infty$, then it goes back to the bare Coulomb potential. The total interatomic energy on Cs atom m is then the sum

$$E_{q,m} = \sum_{n \neq m} \frac{q^2}{4\pi\epsilon_0 r_{mn}} e^{-r_{mn}/\lambda}$$

Here n runs over all the atoms except m itself.

Now I introduce the lattices (Fig. 6.18a). The simple hexagonal lattice is represented by small black dots, and the honeycomb lattice is indicated by the green and blue circles. I use a non-Cartesian coordinates for the simplicity of the calculation. The two axes are in the (10) and (01) direction of the hexagonal lattice, with 60° between them. First I consider the simple hexagonal lattice. Each Cs atom can be straightforwardly labeled with the pair of indices (i, j), with i and j indicating the position in the two directions.

In the simple hexagonal lattice, I focus on the Cs atom at $(0, 0)$. The distance to another Cs atom (i, j) is then

$$r_{ij} = \sqrt{(ia)^2 + (ja)^2 + 2(ia)(ja)\cos 60^\circ} = a\sqrt{i^2 + j^2 + ij},$$

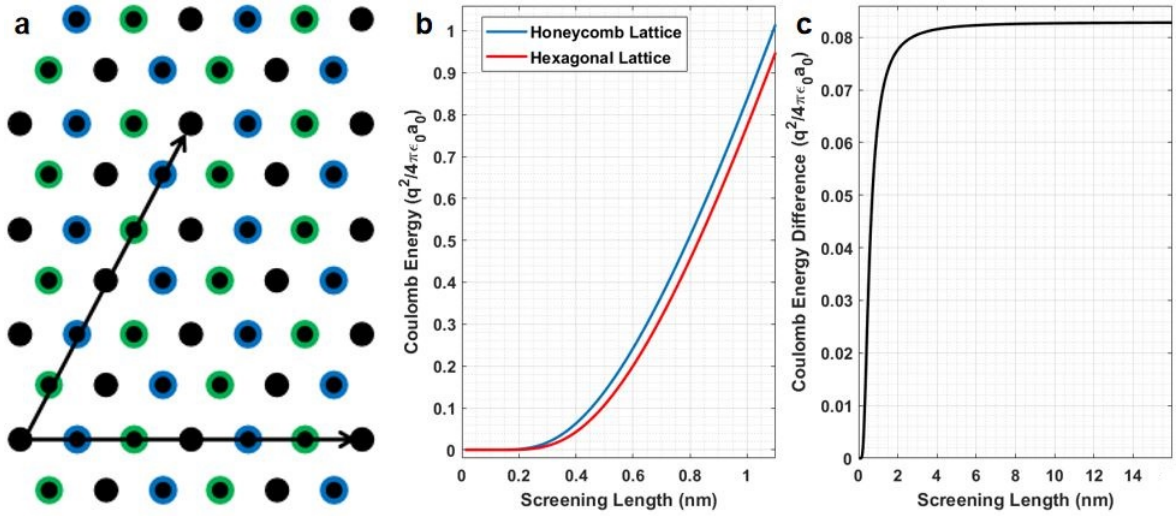

Figure 6.18: (a) Comparison between simple hexagonal lattice (black dots) and honeycomb lattice (blue and green circles). (b) Coulomb energy of charged particles in the simple hexagonal lattice (red) and honeycomb lattice (blue) as a function of the screening length. (c) Difference in the Coulomb energy between the two lattices as a function of the screening length.

a being the atomic spacing. Thus the total interatomic energy of the $(0,0)$ Cs atom is

$$E_{\mathrm{q}} = \sum_{i \cdot j \neq 0} \frac{q^2}{4\pi\epsilon_0 a\sqrt{i^2+j^2+ij}} \cdot e^{-\frac{\sqrt{i^2+j^2+ij}}{\lambda/a}}. \tag{6.4}$$

Here i and j run from $-\infty$ to ∞ except (0,0).

For the honeycomb lattice (blue and green circles), I treat it as the $(\sqrt{3}\times\sqrt{3})$R30° reconstruction of the simple hexagonal lattice, with 1/3 of the lattice points unoccupied. From this point of view, the terms with $(i-j) \equiv 2 \pmod 3$ in Eq. 6.4 should be excluded in the sum for the honeycomb lattice. Thus for one Cs atom is the honeycomb lattice, the total Coulomb energy is

$$E_{\mathrm{q,honey}} = \sum_{i \cdot j \neq 0} \frac{q^2}{4\pi\epsilon_0 a\sqrt{i^2+j^2+ij}} \cdot e^{-\frac{\sqrt{i^2+j^2+ij}}{\lambda/a}} \qquad (i-j) \equiv 0,1 (\mathrm{mod}\ 3).$$

Since the occupation rate is different for hexagonal and honeycomb lattice, the nearest neighbor distance must also be different to keep the Cs atom density the same for the two lattices. For the hexagonal lattice, in the smallest rhombus (red rhombus in Fig. 6.18), there is one Cs atom. While for honeycomb lattice, the number is 2/3. Hence

$$\frac{2/3}{a_{\mathrm{honey}}^2} = \frac{1}{a_{hex}^2}.$$

For simplicity, I define $a_0 = a_{\mathrm{moiré}}/\sqrt{6} = 1.196$ nm. Thus $a_0 = a_{\mathrm{honey}}/\sqrt{2} = a_{\mathrm{hex}}/\sqrt{3}$.

Introducing a_0, the Coulomb energy of hexagonal and honeycomb lattice is then simplified to:

$$E_{\mathrm{q,hex}} = \frac{q^2}{4\pi\epsilon_0 a_0} \cdot \sum_{i \cdot j \neq 0} \frac{e^{-\frac{\sqrt{3(i^2+j^2+ij)}}{\lambda/a_0}}}{\sqrt{3}},$$

and

$$E_{\mathrm{q,honey}} = \frac{q^2}{4\pi\epsilon_0 a_0} \cdot \sum_{i\cdot j\neq 0} \frac{e^{-\frac{\sqrt{2(i^2+j^2+ij)}}{\lambda/a_0}}}{\sqrt{2}} \qquad (i-j) \equiv 0,1(\mathrm{mod}\ 3).$$

Numerical calculation indicates that for the same screening length λ, the Coulomb energy in the honeycomb lattice is always larger than in the simple hexagonal lattice (Fig. 6.18b). With increasing λ, the Coulomb energy for both lattices increases, approaching a linear dependence for large λ. Thus for bare Coulomb potential ($\lambda = \infty$), the total energy does not converge. Since I want to compare the two lattices, the difference in Coulomb energy $\Delta E_q = E_{\mathrm{q,honey}} - E_{\mathrm{q,hex}}$ is presented in Fig. 6.18c. With increasing λ, ΔE_q increases and converges to a constant, $0.084q^2/4\pi\epsilon_0 a_0$. Considering the interatomic interaction between one Cs atom and other Cs atoms far away, due to the isotropy of the Coulomb interaction, the discrete summation is equal to an integral

$$E_{\mathrm{q}} = \int \frac{q\rho(r)}{4\pi\epsilon_0} \mathrm{e}^{-r/\lambda} \mathrm{d}r.$$

Since both lattices have the same Cs density ρ. For large r, the integral is the same for both lattices. The difference in total Coulomb energy only comes from the interaction to the Cs atoms nearby.

The numerical calculation reveals purely from the interatomic Coulomb interaction aspect, the simple hexagonal lattice is more energetically favorable. The energy difference is smaller than the convergence value: $0.084q^2/4\pi\epsilon_0 a_0 = (\frac{q}{e_0})^2 \cdot 1.2\mathrm{eV}$. Due to the insulating nature of hBN, in Cs/hBN/Ir(111), the screening λ should be larger than the one in Cs/gr/Ir(111) (0.66 nm, [86]). According to Fig. 6.18c, ΔE_{q} is close to the convergence value.

Now I discuss the adsorption energy. For simplicity, I ignore the difference between GHs and BHs, and use the sum of three cosine function to model the periodic modulation (illustrated in Fig. 6.19):

$$E_{\mathrm{ad}}(\vec{r}) = \frac{2}{3}E_m - 2E_m(\cos(\vec{k_1}\cdot\vec{r}) + \cos(\vec{k_2}\cdot\vec{r}) + \cos(\vec{k_3}\cdot\vec{r})). \tag{6.5}$$

The three $\vec{k}$ vectors fulfill $|\vec{k_1}| = |\vec{k_2}| = |\vec{k_3}| = 2\pi/a_{\mathrm{moiré}}$, and $\angle\vec{k_1},\vec{k_2} = \angle\vec{k_1},\vec{k_3} = 120°$. Within one moiré unit cell (black rhombus in Fig. 6.19), there exist two points with maximum value of this function (E_m) representing the two hill regions, and one point with minimum value (0) representing the valley region.

For the honeycomb lattice, all the Cs atoms sit in the hill regions. The adsorption energy of one Cs atom is E_m. For the simple hexagonal lattice, since the Cs lattice does not follow the moiré template, the adsorption energy varies for every Cs. I use the average for comparison:

$$E_{\mathrm{ad,hex}}(x) = \lim_{N\to\infty} \frac{1}{N} \sum_{i=0}^{N} E_{\mathrm{ad}}(\vec{r}_i).$$

Numerical calculation including over 10^8 atoms yields $E_{\mathrm{ad,hex}} = \frac{2}{3}E_m$. Thus the adsorption energy of the simple hexagonal lattice is lower than the honeycomb lattice by $E_m/3$.

Experimentally, I observe the honeycomb lattice of Cs adsorbed on hBN/Ir(111), thus the total energy of the honeycomb lattice for Cs atoms must be smaller than the hexagonal lattice:

$$E_{\mathrm{q,honey}} - E_{\mathrm{ad,honey}} < E_{\mathrm{q,hex}} - E_{\mathrm{ad,hex}}.$$

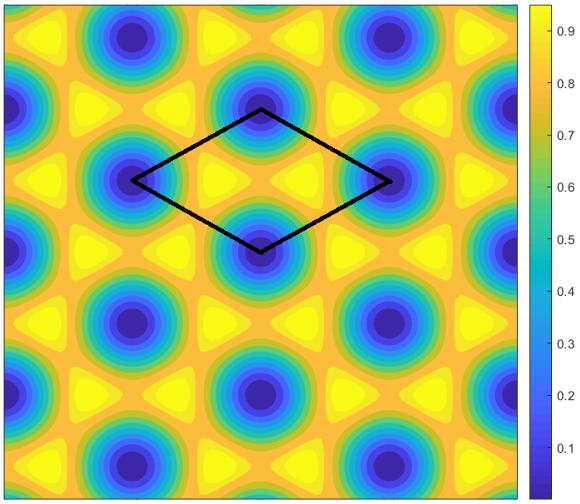

Figure 6.19: Simulated adsorption energy mapping on hBN/Ir(111) by Eq. 6.5.

Here I explain the plus/minus signs in this formula: The Coulomb energy originates from the interatomic repulsion. A low Coulomb energy is favored. Yet the adsorption energy is the energy gain due to charge rearrangement in the adsorption process. A large adsorption energy is favored.

Both energies are higher for the honeycomb lattice. Hence I define ΔE_{q} as $E_{\mathrm{q,honey}} - E_{\mathrm{q,hex}}$, and ΔE_{ad} as $E_{\mathrm{ad,honey}} - E_{\mathrm{ad,hex}}$. Rearranging the adsorption energy to one side of the formula, and Coulomb energy to the other, I obtain:

$$\Delta E_{\mathrm{q}} < \Delta E_{\mathrm{ad}}. \tag{6.6}$$

First I estimate the adsorption energy difference on the right hand side of Eq. 6.6. In Sec. 6.2, I observe the ratio between the GH/BH occupation and calculate the adsorption energy difference $E_1^G - E_1^B = 155$ meV. In Eq. 6.5, E_m is the maximal variation of the adsorption energy within one moiré unit cell. Hence $E_m > 155$ meV, and $\Delta E_{\mathrm{ad}} = E_m/3 > 51$ meV. On the left hand side of Eq. 6.6, the numerical calculation yields $\Delta E_{\mathrm{q}} < (q/e_0)^2 \cdot 1.2$ eV. From the ARPES and XSW measurement results, I obtain $q = 0.2e_0$ within the parallel capacitor model. Thus $\Delta E_{\mathrm{q}} < 48$ meV. Based on these assessments, Eq. 6.6 clearly stands. Hence the honeycomb lattice observed in STM measurements is energetically favored.

I would also point out that, the difference between the term on the two sides of Eq. 6.6 is not as small as 3 meV. In the assessment, I already overestimate ΔE_{q} due to the finite screening length. And for E_m, according to the energy diagram (Fig. 6.12a), maximal variation of the adsorption energy within one moiré unit cell is also much larger than $E_1^G - E_1^B$.

Honeycomb-structured Cs: artificial graphene?

The honeycomb structured Cs adsorption is of particular interest due to its iso-structure to graphene. The C atoms are also arranged in a honeycomb lattice in graphene. The novel electronic structure of graphene, such as the Dirac cones, originates from the π-electrons constrained in a honeycomb network. Similar electronic properties can be created in an artificial system providing

a honeycomb network for a two-dimensional electron gas [87, 88]. The pursuit of such systems, i.e. *artificial graphene*, is of great interest.

If the electrons are mobile among the Cs atoms in the $Cs_{honeycomb}$/hBN/Ir(111) system, one could expect graphene-like electronic structures. Previously in this section, I treat the Cs atoms classically, and consider their interatomic interaction purely as Coulomb repulsion. Now I discuss the problem again in the quantum mechanics picture.

The easiest approach is to calculate the hopping amplitude in the tight binding (TB) model. TB approximation is based on the perturbation theory. The basis here is the wave function of the 6s electron of the Cs atom $\psi(\vec{r})$. Luckily, the 6s wave function is spherically symmetric. The nearest neighbor (nn) amplitude is the convolution between the two 6s electron wave function in the neighboring Cs atoms and the atomic Coulomb potential:

$$t_{\mathrm{nn}} = \int \mathrm{d}\vec{r}\psi^*(\vec{r})\Delta V(\vec{r})\psi(\vec{r}-\vec{\delta}_{\mathrm{nn}}), \tag{6.7}$$

$\vec{\delta}_{\mathrm{nn}}$ being the vector between the nearest neighbor Cs atoms. The next nearest neighbor (nnn) hopping amplitude is similar: One simply has to change $\vec{\delta}_{\mathrm{nn}}$ to the nnn vector $\vec{\delta}_{\mathrm{nnn}}$. In the honeycomb lattice of Cs atoms, the length of $\vec{\delta}_{\mathrm{nnn}}$ is $a_{\mathrm{moiré}}$. And the length of $\vec{\delta}_{\mathrm{nn}}$ is $a_{\mathrm{moiré}}/\sqrt{3}$. The calculated dependence of the nn and nnn hopping amplitude on the moiré periodicity is presented in Fig. 6.20a.

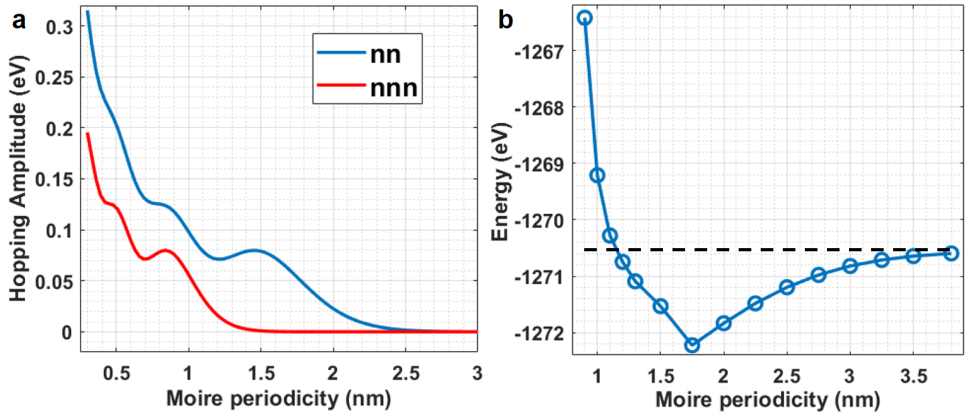

Figure 6.20: (a) Hopping amplitudes, nn (blue) and nnn (red), in tight binding model of honeycomb Cs lattice by Eq. 6.7. (b) Energy of one bi-atomic unit cell of the Cs honeycomb lattice by DFT. The horizontal dashed line indicates the energy of two Cs atoms without interaction.

In the TB calculation, the hopping amplitudes determine the band width. In order to make the band structure detectable, the hopping amplitudes need to be large enough (0.05 eV). In the $Cs_{honeycomb}$/hBN/Ir(111) system, the moiré periodicity is around 3 nm. Clearly, the hopping amplitude is too small (< 0.01 eV). To achieve a detectable and meaningful band structure, the moiré periodicity need to shrink below 1.8 nm.

Density functional theory is also applied to calculate the energy of Cs honeycomb lattice. Similar to the TB model, I calculate the moiré periodicity dependence of the unit cell energy (Fig. 6.20b). For moiré periodicity of around 3 nm, one can see that the interaction (difference between the data points and the dashed line) is very weak for any meaningful binding between the Cs atoms.

Chapter 7

Ample alkali metal incorporation in hBN/Ir(111)

In chapter 6, I discussed the adsorption of alkali metals (Cs and K) on hBN/Ru(0001) and hBN/Ir(111). The geometric and electronic structure of hBN/TM is only slightly modified by the alkali metal adsorption. The hBN/TM substrate functions as a template for the adsorbed alkali metal atoms. When the adsorption density reaches certain value, the alkali metals start to intercalate (Fig. 6.10a and 6.11c).

In Ref. [89], M. Petrović *et al.* report their study on the mechanism of Cs intercalation on gr/Ir(111). The binding energies for different Cs densities are calculated for both adsorption and intercalation morphologies. The calculation reveals that for a dilute density, the adsorption morphology has a higher binding energy. For Cs of high densities, it prefers the intercalation morphology over adsorption.

On the one hand, intercalation lifts up the 2DM, effectively breaking the binding between the 2DM and the TM substrate. On the other hand, direct contact with the TM substrate facilitates easier charge transfer from the alkali metal to the substrate. The work function of TM substrate is higher than the alkali metal. Hence the charge transfer lowers the energy of the system. These two factors compete against each other and determine the morphology of the alkali metal incorporation.

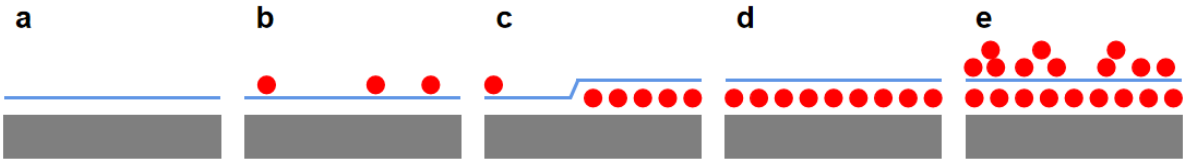

Figure 7.1: The process of alkali metal (K and Cs) incorporation, with increasing amount of alkali metals (left to right). The gray block indicates the TM substrate. The blue line indicates the hBN sheet. The red spheres indicates the alkali metal atoms.

In Fig. 6.10a and 6.11c, I observe the co-existence of alkali metal intercalation and adsorption. Namely alkali metals prefer the pristine hBN/TM area than the intercalated region. In the last chapter, I explained the decisive role of the local work function in the adsorption location. From the

PE measurements, I learn that the alkali metal incorporation lowers the work function of the surface. The work function of pristine hBN/TM is larger than that of the intercalated area. Based on this local work function difference, it is clear that the pristine hBN/TM area is preferred for adsorbed alkali metal atoms over the intercalated area.

With increasing amount of deposition, the intercalation area grows and the pristine hBN/TM area shrinks until full intercalation. With even more deposition, the extra alkali metals can adsorb on intercalated hBN. However, since the interaction between hBN sheet and TM substrate is effectively reduced by the intercalation, the intercalated hBN no longer provides a template for the adsorbed alkali metal atoms. The extra alkali metal atoms hence adsorb in a disordered morphology.

A complete process with increasing amount of alkali metals (Cs and K) is presented in Fig. 7.1. The templating effect of hBN/TM is not illustrated in the sketches, since hBN/Ru(0001) and hBN/Ir(111) function as very distinvtive templates. I would like to point out that, this process does not neccessarily apply to the incorporation of all alkali metals. M. Petrović *et al.* recently report the incorporation of Li in hBN/Ir(111) [30]. Due to its small size, the Li atom does not adsorb on hBN/Ir(111), even at very low concentration. Instead, Li directly intercalates the hBN layer.

In this chapter, I focus on the case of ample alkali metal incorporation (Fig. 7.1e) in hBN/Ir(111). The two sections discuss the incorporation of Cs and K respectively.

7.1 Ample Cs incorporation in hBN/Ir(111)

A high current (6 A) is sent through the alkali metal dispenser for ample alkali metal deposition. Fig. 7.2a presents the LEED result measured on the sample after 30 minutes of Cs deposition on hBN/Ir(111) at RT. Besides the diffraction spots from hBN and Ir(111) substrates, I can observe a sets of additional spots with smaller distance to the center. They correspond to the intercalated Cs, which forms an ordered $\sqrt{3} \times \sqrt{3}$R30° superstructure on Ir(111). The same superstructure is also observed when Cs is directly deposited on bare Ir(111) (not shown).

Fig. 7.2b presents an STM image measured on the same sample. The surface of the sample is covered with clusters of Cs atoms in a disordered manner. Since in quantum tunneling, the tunneling current exponentially decays with the the distance, making STM imaging very surface sensitive. For this type of samples with disordered alkali metal adsorption, STM measurement does not reveal much information on the underlying structure. Hence PE characterizations are performed.

The N 1s and B 1s spectra are displayed in Fig. 7.2c and d. The maxima of the two spectra are found at 400.51 eV and 192.62 eV. Compared to the spectra measured on pristine hBN/Ir(111) (N 1s 397.58 eV, B 1s 189.92 eV), I observe large shifts to higher BE. The shifts are much larger than the ones observed on the $Cs_{honeycomb}$/hBN/Ir(111) (397.73 eV, 190.02 eV, Fig. 6.15). The comparison of the N 1s spectra measured among these three samples are displayed in Fig. 7.2e. Another important observation is that the shape of the N 1s spectrum is very different from pristine hBN/Ir(111) and $Cs_{honeycomb}$/hBN/Ir(111). This change of the peak shape indicates the fundamental modification of the hBN structure: The absence of the double peak feature reflects the decoupling of the hBN layer from the substrate. The increased peak width originates from the inhomogeneous chemical environment induced by the disordered Cs adsorption.

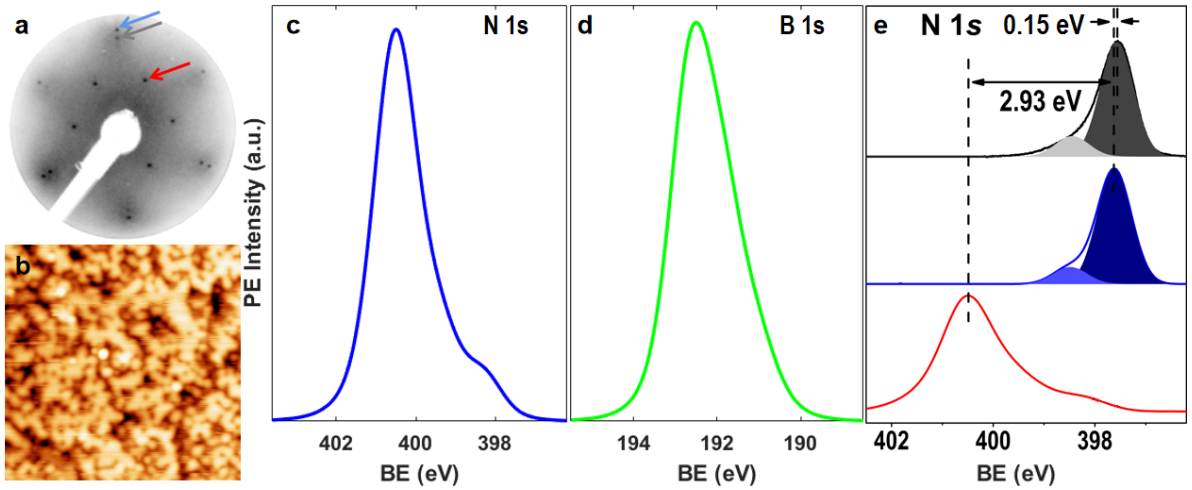

Figure 7.2: Measurement results on hBN/Ir(111) after ample Cs deposition. (a) LEED pattern displays the diffraction spots from hBN (blue arrow) and Ir(111) (gray arrow), together with diffraction spots from intercalated Cs (red arrow). (b) STM image of ample Cs/hBN/Cs/Ir(111) surface. 120×80 nm^2, $U_b = 2.4$V, $I_{tunneling} = 20$ pA. (c) N 1s spectrum $h\nu = 600$ eV. (d) B 1s spectrum measured with photon energy $h\nu = 300$ eV. (e) Comparison of N 1s spectra measured on pristine (gray), $Cs_{honeycomb}$/hBN/Ir(111) (blue), and Cs/hBN/Cs/Ir(111) (red).

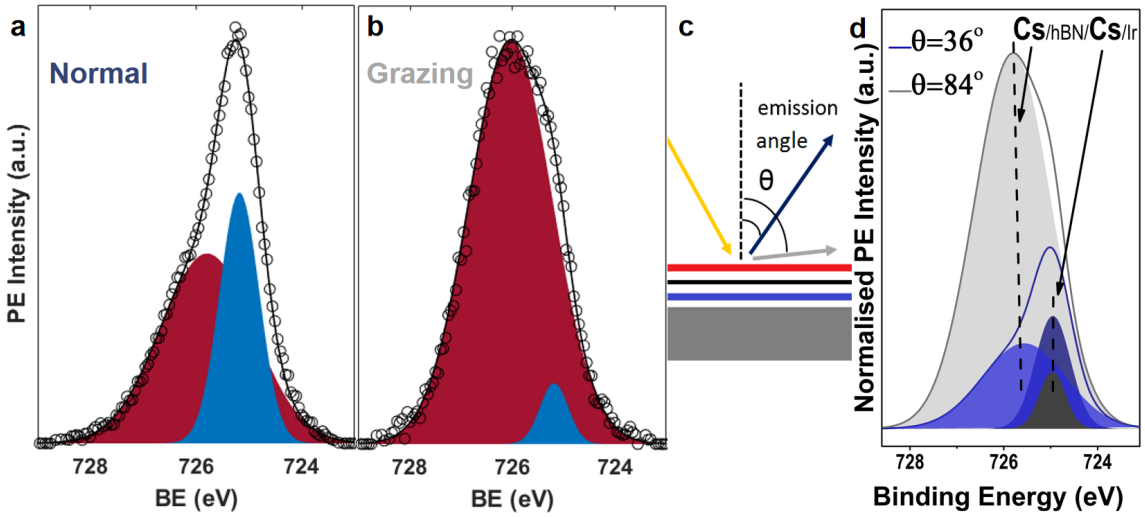

Figure 7.3: Cs $3d_{5/2}$ spectrum, $h\nu = 900$ eV. (a) measured at emission angle $\theta = 36°$. (b) measured at emission angle $\theta = 84°$. (c) Sketch of the PE signal from a system with stacking. (d) Cs $3d_{5/2}$ spectra in (a) and (b) normalized to the corresponding N 1s intensity.

The shape of the Cs $3d_{5/2}$ spectrum is quite intriguing. Fig. 7.3a and b display the Cs $3d_{5/2}$ spectrum measured at two different emission angles. They appear quite different in the shape. The maximum of the two spectra are even at different BE (Fig. 7.3a 724.95 eV, Fig. 7.3b 725.57 eV).

On the ample Cs sample, there are two types of Cs: the adsorption and the intercalation. Due to the very different chemical environment, their $3d_{5/2}$ electrons are at different BEs. Having this

fact in mind, it is clear that the two different positions observed in Fig. 7.3a and b are from the two different types of Cs. Following this idea, I fit the Cs $3d_{5/2}$ spectra with two components (red and blue peaks in Fig. 7.3a and b). The component at higher BE (red) is more intense when measured at grazing emission angle, and the low BE component (blue) is stronger at normal emission angle.

In Fig. 7.3c, I illustrate the PE process on the sample surface. The hBN layer (black) is sandwiched by Cs adsorption (red) and Cs intercalation (blue). The photoelectrons are activated by the incident photons from both types of Cs atoms. The photoelectrons from the intercalated Cs atoms have to travel through the hBN layer and the Cs adsorption to reach the analyzer. During this process, they could get scattered, attenuating the PE signal. At a grazing emission angle, due to the increased travel length, the scattering probability increases, thus enhanced attenuation. Qualitatively, the PE measurement at a grazing emission angle is more surface sensitive. Hence in the Cs $3d_{5/2}$ spectra, the high BE component (red) originates from Cs adsorption, while the low BE component (blue) Cs intercalation.

Considering the sandwiched position of the hBN sheet, I have a more quantitative method of determine the stacking relation. I use the N 1s signal intensities as a standard, and normalize the Cs $3d_{5/2}$ spectra to them (Fig. 7.3d). By comparing the normalized intensities at different emission angles, I can determine the stacking relation in respect to the hBN layer. The normalized intensity of the low BE component (924.95 eV) increases when moving from grazing to normal emission angle. This increased intensity indicates that this type of Cs atoms are below the hBN layer. The high BE component behaves quite the opposite. Hence this component comes from the Cs atoms on top. The stacking relation determined this way agrees with the qualitative method discussed in the last paragraph.

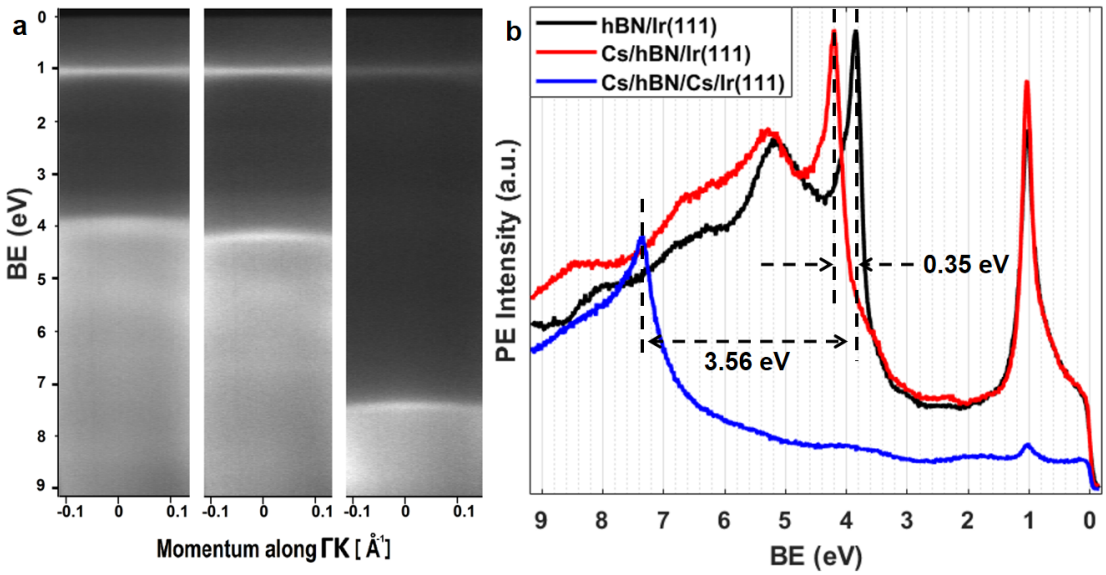

Figure 7.4: Comparison of ARPES measurement results among pristine hBN/Ir(111), $Cs_{honeycomb}$/hBN/Ir(111), and Cs/hBN/Cs/Ir(111). (a) ARPES mapping around the Γ-point. (b) PE intensity extracted from (a).

ARPES measurement is conducted on the ample Cs sample. Due to the low photon energy used (He I, 21.2 eV), a full range mapping including the top of the π-band at K point is not possible. From the detectable range, I observe a large shift of the hBN bands to higher BE. Fig. 7.4a displays the comparison around the Γ-point among the ARPES mappings on pristine hBN/Ir(111), $Cs_{honeycomb}$/hBN/Ir(111), and Cs/hBN/Cs/Ir(111) (left to right). The Ir band still stays at around 1 eV in BE after ample Cs incorporation. Fig. 7.4b extracts the intensity at the Γ-point as a function of the BE. Compared to the 0.35 eV shift induced by the honeycomb structured Cs adsorption (red), ample Cs incorporation shifts the top of the σ-bands by 3.56 eV.

The shift can be approximated with vacuum level alignment: as an estimate of the work function of Cs/hBN/Cs/Ir(111), I use the value for bulk Cs, which is an established approximation for the case of alkali metals on metal surfaces [90]. The difference between $\Phi_{Ir(111)}$ (5.76 eV, all work function values are taken from Ref. [91]) and Φ_{Cs} (2.14 eV) is 3.62 eV, which is indeed very similar to the 3.56 eV shift observed in the ARPES measurement (Fig. 7.4). A. Fedorov *et al.* reported their study of K intercalation on hBN/Au/Ni(111) [43]. The work function difference can be approximated as $\Delta\Phi = \Phi_{Au(111)} - \Phi_K = 5.31 - 2.30 = 3.01$ eV. This value is also close to the hBN band shift they reported (2.77 eV).

The rest of the band structure is not in the detection range. On the $Cs_{honeycomb}$/hBN/Ir(111) sample, I witness a rigid shift of the hBN bands. For the Cs/hBN/Cs/Ir(111) here, I also assume a rigid shift. The bottom of the π-band is then at 11.64 eV in BE. The top of the π-band is at 5.85 eV. The Fermi surface from Γ-point to K-point is fully detectable. No sign of the conduction bands is observed. The absence of the conduction bands under the Fermi energy indicates that the band gap of hBN must be larger than 5.85 eV.

Fig. 7.5 presents the XSW measurement data and analysis on the Cs/hBN/Cs/Ir(111) sample. The measured intensities at different photon energies are displayed in circles, while the lines are from the optimized fitting. The optimized parameters are from the listed in Tab. 7.1:

	P^H	f^H	n	h(Å)
adsorbed Cs	0.29	0.68	4	9.52
B 1s	0.93	0.68	2	6.50
N 1s	0.88	0.83	2	6.38
intercalated Cs	0.42	0.93	1	3.15
Cs/Ir(111)	0.59	0.52	1	3.52

Table 7.1: Optimized fitting parameters for XSW results on Cs/hBN/Cs/Ir(111) sample, and Cs/Ir(111). Errors: $\Delta P^H = \pm 0.01$, $\Delta f^H = \pm 0.04$, $\Delta h = \pm 0.02$ Å.

For comparison, I have also conducted XSW measurements on the sample where Cs is deposited on bare Ir(111). The same $\sqrt{3} \times \sqrt{3}$R30° superstructure is observed with LEED (not shown), indicating the similarity to the Cs intercalation in the Cs/hBN/Cs/Ir(111) sample. For Cs directly on bare Ir(111), the coherent fraction is relatively low (0.52), compared to the intercalated Cs in the Cs/hBN/Cs/Ir(111) sample (0.93). The adsorption height is also slightly higher. I assign these differences to the strict monolayer feature of the intercalated Cs atoms. Namely in the Cs/hBN/Cs/Ir(111)

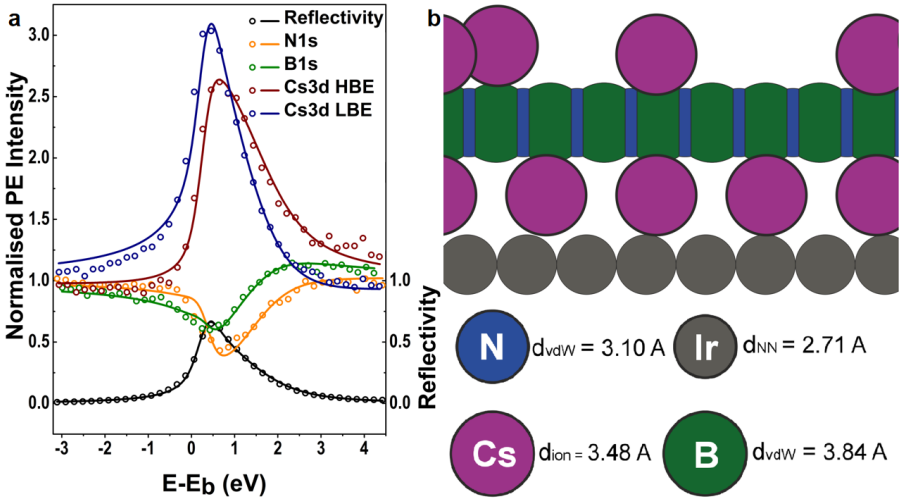

Figure 7.5: (a) XSW results for the two components of Cs $3d_{5/2}$ (red for adsorption, blue for intercalation), the N 1s (orange) and B 1s (green) in Cs/hBN/Cs/Ir(111). The measured intensity are presented in circles, and the lines are optimized fitting lines. (b) Relative position of adsorbed Cs, hBN, intercalated Cs, and the first layer of iridium atoms in Cs/hBN/Cs/Ir(111); the sphere sizes indicate the van der Waals radius, ionic radius or nn distance, and relative height extracted from XSW results.

sample, the hBN layer constrains all the intercalated Cs atoms to sit at some specific atomic registries in the Ir(111) surface. No extra Cs atoms exist below the hBN layer. While on bare Ir(111), besides the Cs atoms sitting at such atomic registries, which form the $(\sqrt{3} \times \sqrt{3})$ superstructure observed by LEED, additional Cs atoms cluster on top, increasing the average height and reducing the height distribution.

The height of each species are calculated from P^{H}. The comparison of these measured dimensions, Fig. 7.5b presents the stacking relation in the Cs/hBN/Cs/Ir(111) sample. The sizes of the spheres are the ionic, vdW radius of the elements, or the nn distance (for details, check Fig. 6.16 in the last chapter).

7.2 Ample K incorporation in hBN/Ir(111)

In this section, I change the alkali metal to K and explore the incorporation of ample K in hBN/Ir(111).

The XPS results are presented in Fig. 7.6. The position of the N 1s (B 1s) spectrum maximum is at 400.08 (191.87) eV in BE. Compared to the N 1s (B 1s) spectrum measured on pristine hBN/Ir(111), the shift in BE is 2.50 (1.95) eV. A brief summary of core level shift in hBN on the different samples discussed in this thesis is listed in Tab. 7.2.

Fig. 7.6c-e present the core levels of K. The K 2s and K 3p spectra appear to be two singlet, and K 2p a doublet. The intensity of the K 2s signal is quite low. The low signal to noise ratio renders unnecessary uncertainty in the further analysis. Thus I focus on the K 2p and K 3p spectra in the remaining part of the section.

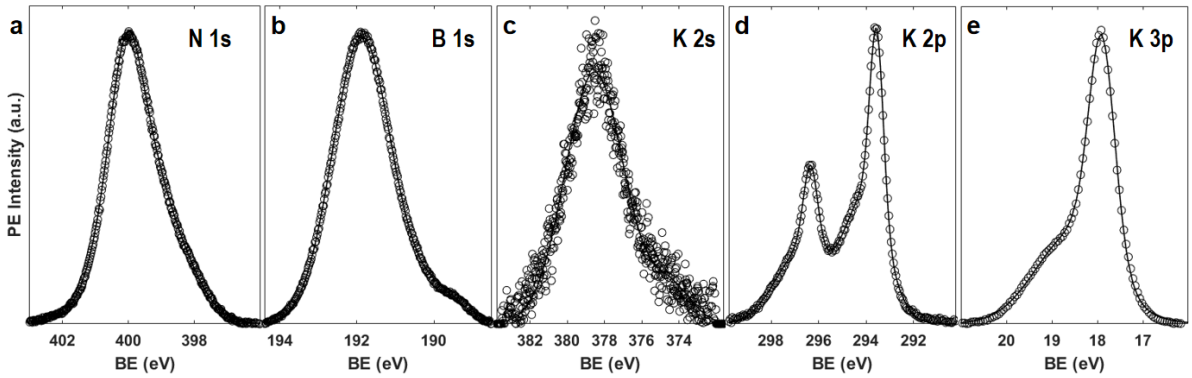

Figure 7.6

	N 1s	B 1s	ΔE_{N1s}	ΔE_{B1s}
pristine hBN/Ir(111)	397.58	189.92	-	-
$\mathrm{Cs_{honeycomb}}$/hBN/Ir(111)	397.73	190.02	0.15	0.10
Cs/hBN/Cs/Ir(111)	400.51	192.62	2.93	2.70
K/hBN/K/Ir(111)	400.08	191.87	2.50	1.95

Table 7.2: Positions of N 1s and B 1s core levels in BE measured on pristine hBN/Ir(111), and three alkali metal incorporated samples.

Fig. 7.7 present the K 2p and K 3p spectra measured at different emission angles. The change of the spectrum shape and the shift of the peak position is very similar to the Cs $3d_{5/2}$ spectra measured on the Cs/hBN/Cs/Ir(111) sample (Fig. 7.3a and b). Thus I decompose the K 3p spectrum to two components. For the K 2p spectra, both $2p_{1/2}$ and $2p_{3/2}$ signals are fitted with two components. The similar emission angle dependence of the two peaks indicates that the low BE components are from K intercalation, and the high BE components are from K adsorption.

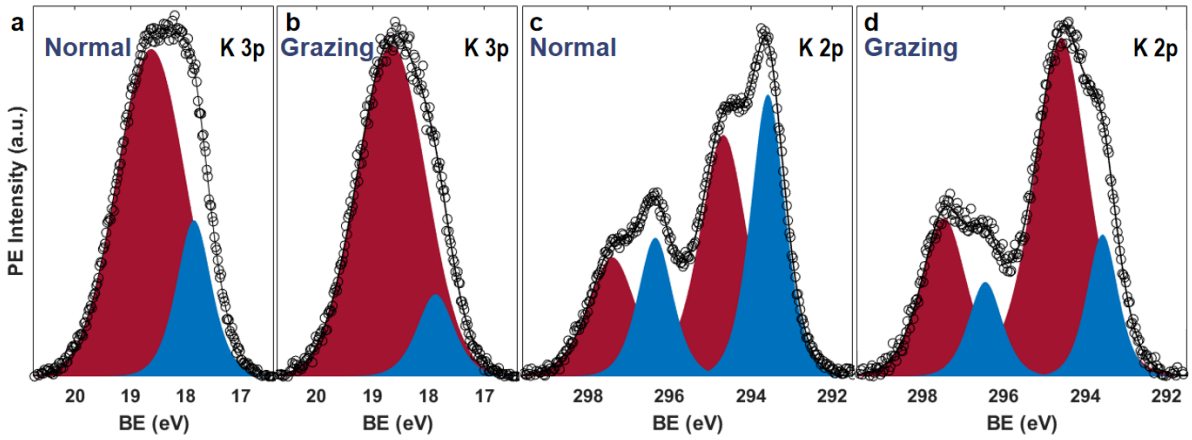

Figure 7.7: K 2p and K 3p spectra measured on K/hBN/K/Ir(111) sample at different emission angles. (a) and (c) measured at $\theta = 36°$, (b) and (d) measured at $\theta = 84°$.

One might notice the irregularity of the relative positions of the intercalation and adsorption components in BE. The intercalated alkali metal atoms are in direct contact of the TM substrate, they should lose more charge than the adsorbed alkali metal atoms, i.e. a higher oxidation state. Thus why is the intercalation signal at a lower BE than the adsorption? This apparent irregularity is also present in the Cs/hBN/Cs/Ir(111) spectra (Fig. 7.3).

The answer lies in the shift of all the electronic states induced by the static field on the sample surface, i.e. the gating effect. On the ample alkali metal incorporation samples, two layers of alkali metals sandwich the hBN layer. In the toy model of parallel plate capacitor (Fig. 7.5a, three contacts, the Ir(111) substrates, the Cs intercalation, and the Cs adsorption, are on different electric potential. The electric field between the alkali metal intercalation and the adsorption provide an extra shift to the core levels in the adsorbed alkali metal atoms than the intercalated ones, hence the higher BE of the adsorption signals.

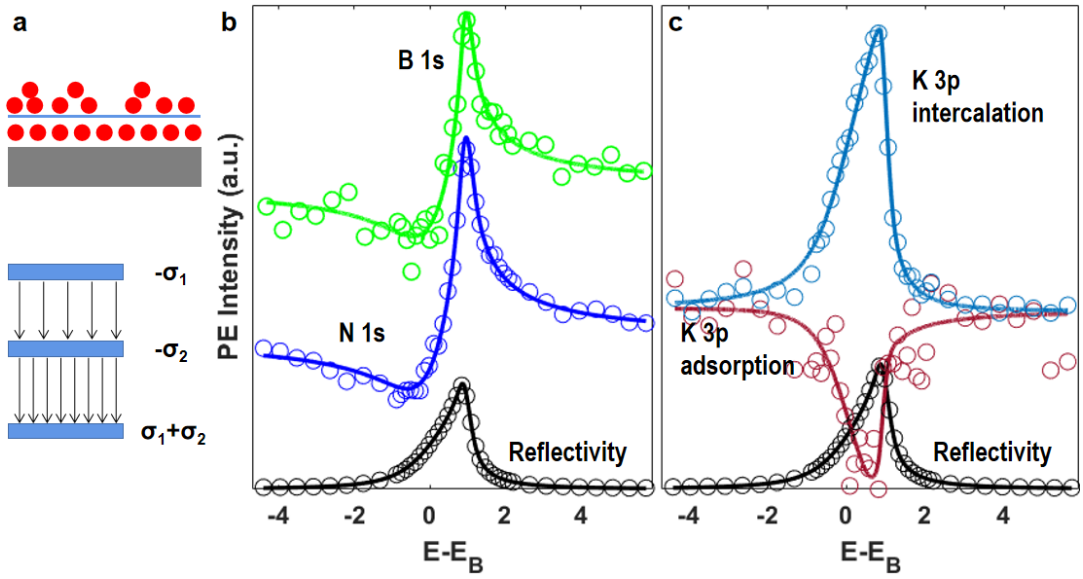

Figure 7.8

The hBN layer sits between the intercalation and the adsorption. Thus it feels the whole potential difference between the substrate and the intercalation, but only part of the potential difference between the adsorption and the intercalation:

$$\Delta V = [\sigma_2 h_{\text{intercalation}} + \sigma_1 (h_{\text{hBN}} - h_{\text{intercalation}})]/\epsilon_0.$$

Both charge densities are unknown parameters. It is not possible to calculate both densities, and thus the charge transfer of the two types of alkali metal atoms.

XSW measurements have also been conducted for N 1s, B 1s and K 3p, obtained on the K/hBN/K/Ir(111) sample. The modulated PE intensities are displayed by the circles in Fig. 7.8b and c. The optimized fittings are presented by the lines. The optimized parameters P^{H} and f^{H} for each elemental species are listed in Tab. 7.3. For comparison, I also prepare a sample where K is directly deposited on bare Ir(111), and characterize it with XSW.

	p^H	f^{H}	n	h(Å)
adsorbed K	0.86	0.98	3	8.56
B 1s	0.67	0.60	2	5.92
N 1s	0.68	0.60	2	5.94
intercalated K	0.31	0.47	1	2.90
K/Ir(111)	0.40	0.75	1	3.10

Table 7.3: Optimized fitting parameters for XSW results on K/hBN/K/Ir(111) sample. Errors: $\Delta P^{\mathrm{H}} = \pm 0.01$, $\Delta f^{\mathrm{H}} = \pm 0.04$, $\Delta h = \pm 0.02$ Å.

Comparing the K/Ir(111) sample and the intercalated K in K/hBN/K/Ir(111), I found that the height of the K intercalation is lower than the K atoms adsorbed on bare Ir(111). This lowered adsorption height is in agreement with the Cs incorporation (Tab. 7.1): the hBN layer presses the intercalated alkali metal atoms closer to the Ir(111) substrate. However, unlike the very high coherent fraction f^{H} in the Cs case, the intercalated K atoms are not very mono-dispersed in adsorption height. In the Cs incorporation case, LEED measurements reveal a $\sqrt{3} \times \sqrt{3}\mathrm{R}30^\circ$ superstructure of Cs on Ir(111). However, on the K/hBN/K/Ir(111) sample, besides the Ir(111) and hBN spots, no additional diffraction spots are observed in the LEED parttern. This absence of the superstructure supports the disordered structure of the intercalated K atoms in K/hBN/K/Ir(111) sample.

According to the XSW analysis, the height of the hBN layer is 5.93 Å. This height is lower than that in the ample Cs incorporation sample (6.44 Å, Tab. 7.1). This lowered height is expected since the size of K atoms are smaller than Cs atoms. Sequentially, the height of the adsorbed K atoms (8.56 Å) is also lower than the adsorbed Cs atoms (9.52 Å, Tab. 7.1).

Chapter 8

Summary and outlook

In this thesis, I present my study on the ultra-thin insulator, hBN. To start with, I study the epitaxial growth of hBN on two different TM substrates, Ir(111) and Ru(0001). LEED and STM measurements indicate that it is more challenging to prepare a well aligned hBN layer on Ru(0001) than on Ir(111). More demanding growth conditions (lower precursor pressure) is required for hBN/Ru(0001).

Due to the lattice mismatch between hBN and TM substrates, the two periodic atomic structures form a third periodic superstructure, i.e. the moiré pattern. The strength of the hBN-TM interaction is modulated within a moiré unit cell, leading to a corrugation geometry of the hBN layer: In the regions where the hBN-TM interaction is strong/weak, the hBN-TM distance is small/large. The XPS and XSW measurements reveal a weaker hBN-TM interaction and a flatter hBN geometry on Pt(111) than on Ir(111).

I briefly study the in-plane heterostructure between hBN and graphene. I grow hBN and graphene sequentially. LEED characterization reveals an enhanced alignment of graphene when sub-monolayer hBN is present on both Ir(111) and Ru(0001). The 2d-epitaxy between hBN and graphene provides additional drive for alignment to the TM substrate.

To study the hBN-TM interaction locally, I use DFT to calculate the adsorption of some small B/N containing molecules on TM surfaces. The adsorption of many molecules are tested on Ir(111). According to the adsorption heights, the best ones to simulate hBN in the valley regions is ammonia and borazine. The adsorption of ammonia on different TM substrates indicates the local atomic hBN-TM interaction strength is weak on Ni(111) and Pt(111), stronger on Ir(111), and even stronger on Ru(0001). The difference between Ir(111) and Ru(0001) is small. The adsorption energy is used as a measure for the interaction strength. After switching to borazine, the difference between Ir(111) and Ru(0001) enlarges. The dimensional mismatch plays a vital role.

I venture two possible directions for using small molecules to further simulate hBN locally: (i) It might be worthwhile to simulate hBN in the hill regions to fix the borazine molecule at the adsorption height the same as the hBN hills and includes vdW interaction into the calculation. (ii) The misaligned hBN domains might be simulated by misaligned adsorption of borazine molecules on TM substrates.

The moiré pattern of hBN/TM generates not only the corrugation geometry of hBN, but also a periodic modulation of the electronic properties. This periodic spatial modulation leads to site-

selective adsorption of adatoms. I study the adsorption of Cs/K on hBN/Ru(0001) and hBN/Ir(111). For hBN/Ru(0001), the preferred adsorption sites are the valley regions of the moiré unit cell. One valley region can accommodate multiple Cs/K adatoms. To simulate the occupation distribution, I carry out a MC simulation. The simulation reveals the vital role played by the interatomic repulsion between Cs/K atoms.

From the MC simulation, I extract the average charge of the adatoms. K (0.26 e_0) is more positively charged than Cs (0.22 e_0). This contradicts the smaller ionization energy of Cs than K. I lack a sound explanation for this contradiction at the moment. For future investigation, I venture three possible directions: (i) In the MC simulation, the infinite rectangular potential well used might be an oversimplification of the adsorption energy diagram of the alkali metal atoms. More gradual potential, *e.g.* quadratic potential, could be tested. (ii) A more sophisticated MC simulation including the inter-cell interaction of the alkali metals could be tested. (iii) Classical Coulomb energy is used to calculate for the energy levels $\epsilon(n)$. However, the small interatomic spacing probably already introduce some quantum effect to the interaction between alkali metals. A more sophisticated calculation, possibly with DFT, of the energy levels is required.

For hBN/Ir(111), the preferred adsorption sites are the hill regions of the moiré unit cells. Each hill region can only accommodate one Cs adatom. A room temperature, the Cs atoms form a hexagonal lattice, indicating the preference to one of the two hill regions in one moiré unit cell. Additional Cs deposition leads to an amorphous Cs structure and intercalation. At elevated temperature, a honeycomb structure of Cs is achieved. Both hill regions are occupied. XPS measurements reveal a small shift of the N/B 1s core levels and the hBN bands induced by the positively charged Cs adsorption and negatively charged Ir(111) substrate, i.e. the gating effect.

Further improvement for the elevated temperature deposition is possible in pursuit of a Cs honeycomb lattice with higher quality. The sample temperature could be more carefully adjusted. In my study, 20 °C steps are tested around 400 °C. Smaller testing steps might lead to higher degree of ordering. On the other hand, I have only studied the kinetic aspects of the adsorption, one could also try the dynamic approach, i.e. adjusting the Cs deposition rate, to improve the quality. Besides the honeycomb lattice, the double peak feature observed in the ARPES mapping after 2 minutes of Cs deposition (blue curves in Fig. 6.14d) suggests other ordered structures of Cs adsorption with lower concentration. The new ordered structures are worthwhile for further STM investigation.

For honeycomb structured Cs adsorption, I calculate the interatomic interaction. It turns out that the large spacing between the Cs atoms on our samples leads to very small overlap of the atomic orbitals. To pursue the "artificial graphene", a smaller Cs-Cs distance is needed. One possible approach is to deposit Cs on rotational domains of hBN on Ir(111), where the moiré periodicity is reduced. For example, the moiré periodicity on 30° rotational hBN domains on Ir(111) is only approximately 5 Å. According to my calculation (Fig. 6.20 in Sec. 6.3), the Cs-Cs spacing induced by such small moiré periodicity leads to dispersed band structure. The difficulty of following this idea lies in the epitaxial growth of extended rotational hBN domains on Ir(111).

In the adsorption scenario, the alkali metal density is low, thus providing little modification to the geometric and electronic structure of hBN. To pursue a stronger gating effect, I study the ample incorporation of Cs/K in hBN/Ir(111). In this scenario, Cs/K intercalates under hBN, as well as adsorbs on top of hBN. The intercalation lifts up the hBN layer and irons out the corrugation. Large shifts of the core levels and hBN bands are detected. On the Cs/hBN/Cs/Ir(111) sample, we observe a 3.56 eV shift at the top of the σ-bands. In the assumption of a rigid shift, the absence of the conduction bands under Fermi level sets a lower bond of 5.85 eV for the hBN band gap.

To solve the mystery of the hBN band gap, an even stronger gating effect is needed. Given that Cs is the non-radioactive alkali metal with the lowest ionization energy, I venture two possible directions: (i) Alkaline earth metals have two electrons in the outmost s orbitals. The charge transfered from them might be larger than alkali metals when incorporated in hBN/TM systems. (ii) The combination of two types of alkali metals might induce a stronger gating effect. Different alkali metal atoms have different sizes. It is possible for the smaller atoms to squeeze into the interstitial space of the large atoms. The resulting alloy can provide more charge transfer hence stronger gating effect.

Bibliography

[1] Kostya S Novoselov, Andre K Geim, Sergei V Morozov, D Jiang, Y Zhang, Sergey V Dubonos, Irina V Grigorieva, and Alexandr A Firsov. Electric field effect in atomically thin carbon films. *Science*, 306(5696):666–669, 2004.

[2] Monica Pozzo, Dario Alfe, Paolo Lacovig, Philip Hofmann, Silvano Lizzit, and Alessandro Baraldi. Thermal expansion of supported and freestanding graphene: lattice constant versus interatomic distance. *Physical Review Letters*, 106(13):135501, 2011.

[3] Farzaneh Mahvash, Etienne Paradis, Dominique Drouin, Thomas Szkopek, and Mohamed Siaj. Space-charge limited transport in large-area monolayer hexagonal boron nitride. *Nano Letters*, 15(4):2263–2268, 2015.

[4] Aleksey Falin, Qiran Cai, Elton JG Santos, Declan Scullion, Dong Qian, Rui Zhang, Zhi Yang, Shaoming Huang, Kenji Watanabe, Takashi Taniguchi, Matthew R. Barnett, Ying Chen, Rodney S. Ruoff, and Lu Hua Li. Mechanical properties of atomically thin boron nitride and the role of interlayer interactions. *Nature Communications*, 8(1):1–9, 2017.

[5] Alastair Macrae Howatson. *Engineering tables and data*. Springer Science & Business Media, 2012.

[6] John P Perdew, Kieron Burke, and Matthias Ernzerhof. Generalized gradient approximation made simple. *Physical Review Letters*, 77(18):3865, 1996.

[7] Xavier Gonze, J-M Beuken, R Caracas, F Detraux, M Fuchs, G-M Rignanese, Luc Sindic, Matthieu Verstraete, G Zerah, F Jollet, et al. First-principles computation of material properties: the abinit software project. *Computational Materials Science*, 25(3):478–492, 2002.

[8] Xavier Gonze, Bernard Amadon, Gabriel Antonius, Frédéric Arnardi, Lucas Baguet, Jean-Michel Beuken, Jordan Bieder, François Bottin, Johann Bouchet, Eric Bousquet, et al. The abinit project: Impact, environment and recent developments. *Computer Physics Communications*, 248:107042, 2020.

[9] H Şahin, S Cahangirov, M Topsakal, E Bekaroglu, E Akturk, R Tugrul Senger, and Salim Ciraci. Monolayer honeycomb structures of group-IV elements and III-V binary compounds: First-principles calculations. *Physical Review B*, 80(15):155453, 2009.

[10] Jian Zhou, Qian Wang, Qiang Sun, and Puru Jena. Electronic and magnetic properties of a BN sheet decorated with hydrogen and fluorine. *Physical Review B*, 81(8):085442, 2010.

[11] CE Ekuma, V Dobrosavljević, and D Gunlycke. First-principles-based method for electron localization: Application to monolayer hexagonal boron nitride. *Physical Review Letters*, 118(10):106404, 2017.

[12] M Topsakal, E Aktürk, and S Ciraci. First-principles study of two-and one-dimensional honeycomb structures of boron nitride. *Physical Review B*, 79(11):115442, 2009.

[13] Xavier Blase, Angel Rubio, Steven G Louie, and Marvin L Cohen. Quasiparticle band structure of bulk hexagonal boron nitride and related systems. *Physical Review B*, 51(11):6868, 1995.

[14] Jiangtao Wu, Baolin Wang, Yujie Wei, Ronggui Yang, and Mildred Dresselhaus. Mechanics and mechanically tunable band gap in single-layer hexagonal boron-nitride. *Material Research Letters*, 1(4):200–206, 2013.

[15] A Bhattacharya, S Bhattacharya, and GP Das. Band gap engineering by functionalization of BN sheet. *Physical Review B*, 85(3):035415, 2012.

[16] Mengxi Liu, Yuanchang Li, Pengcheng Chen, Jingyu Sun, Donglin Ma, Qiucheng Li, Teng Gao, Yabo Gao, Zhihai Cheng, Xiaohui Qiu, Ying Fang, Yanfeng Zhang, and Zhongfan Liu. Quasi-freestanding monolayer heterostructure of graphene and hexagonal boron nitride on Ir(111) with a zigzag boundary. *Nano Letters*, 14(11):6342–6347, 2014.

[17] Ki Kang Kim, Allen Hsu, Xiaoting Jia, Soo Min Kim, Yumeng Shi, Mario Hofmann, Daniel Nezich, Joaquin F Rodriguez-Nieva, Mildred Dresselhaus, Tomas Palacios, and Jing Kong. Synthesis of monolayer hexagonal boron nitride on Cu foil using chemical vapor deposition. *Nano Letters*, 12(1):161–166, 2011.

[18] Yang Gao, Wencai Ren, Teng Ma, Zhibo Liu, Yu Zhang, Wen-Bin Liu, Lai-Peng Ma, Xiuliang Ma, and Hui-Ming Cheng. Repeated and controlled growth of monolayer, bilayer and few-layer hexagonal boron nitride on Pt foils. *ACS Nano*, 7(6):5199–5206, 2013.

[19] Jaehyun Han, Jun-Young Lee, Heemin Kwon, and Jong-Souk Yeo. Synthesis of wafer-scale hexagonal boron nitride monolayers free of aminoborane nanoparticles by chemical vapor deposition. *Nanotechnology*, 25(14):145604, 2014.

[20] Yenny Hernandez, Valeria Nicolosi, Mustafa Lotya, Fiona M Blighe, Zhenyu Sun, Sukanta De, IT McGovern, Brendan Holland, Michele Byrne, Yurii K Gun'Ko, et al. High-yield production of graphene by liquid-phase exfoliation of graphite. *Nature Nanotechnology*, 3(9):563–568, 2008.

[21] Sungjin Park and Rodney S Ruoff. Chemical methods for the production of graphenes. *Nature Nanotechnology*, 4(4):217–224, 2009.

[22] Konstantin S Novoselov, VI Fal'ko, L Colombo, PR Gellert, MG Schwab, and K Kim. A roadmap for graphene. *Nature*, 490(7419):192–200, 2012.

[23] Fabian Schulz, Robert Drost, Sampsa K Hämäläinen, Thomas Demonchaux, Ari P Seitsonen, and Peter Liljeroth. Epitaxial hexagonal boron nitride on Ir(111): A work function template. *Physical Review B*, 89(23):235429, 2014.

[24] Simon Berner, Martina Corso, Roland Widmer, Oliver Gröning, Robert Laskowski, Peter Blaha, Karlheinz Schwarz, Andrii Goriachko, Herbert Over, Stefan Gsell, et al. Boron nitride nanomesh: Functionality from a corrugated monolayer. *Angewandte Chemie international edition*, 46(27):5115–5119, 2007.

[25] S Koch, M Langer, S Kawai, E Meyer, and Th Glatzel. Contrast inversion of the h-BN nanomesh investigated by nc-AFM and Kelvin probe force microscopy. *Journal of Physics: Condensed Matter*, 24(31):314212, 2012.

[26] Ferdinand H Farwick zum Hagen, Domenik M Zimmermann, Caio C Silva, Christoph Schlueter, Nicolae Atodiresei, Wouter Jolie, Antonio J Martínez-Galera, Daniela Dombrowski, Ulrike A Schröder, Moritz Will, et al. Structure and growth of hexagonal boron nitride on Ir(111). *ACS Nano*, 10(12):11012–11026, 2016.

[27] Marcella Iannuzzi, Fabien Tran, Roland Widmer, Thomas Dienel, Kevin Radican, Yun Ding, Jürg Hutter, and Oliver Gröning. Site-selective adsorption of phthalocyanine on h-BN/Rh(111) nanomesh. *Physical Chemistry Chemical Physics*, 16(24):12374–12384, 2014.

[28] Thomas Brugger, Sebastian Günther, Bin Wang, J Hugo Dil, Marie-Laure Bocquet, Jürg Osterwalder, Joost Wintterlin, and Thomas Greber. Comparison of electronic structure and template function of single-layer graphene and a hexagonal boron nitride nanomesh on Ru(0001). *Physical Review B*, 79(4):045407, 2009.

[29] Thomas Brugger, Haifeng Ma, Marcella Iannuzzi, Simon Berner, Adolf Winkler, Jürg Hutter, Jürg Osterwalder, and Thomas Greber. Nanotexture switching of single-layer hexagonal boron nitride on rhodium by intercalation of hydrogen atoms. *Angewandte Chemie International Edition*, 49(35):6120–6124, 2010.

[30] Marin Petrović. Sequential lithium deposition on hexagonal boron nitride monolayer on Ir(111): Identifying intercalation and adsorption. *Surface Science*, 706:121786, 2021.

[31] A Goriachko, YB He, and H Over. Complex growth of nanoAu on BN nanomeshes supported by Ru(0001). *The Journal of Physical Chemistry C*, 112(22):8147–8152, 2008.

[32] Bin Wang and Marie-Laure Bocquet. Monolayer graphene and h-bn on metal substrates as versatile templates for metallic nanoclusters. *The Journal of Physical Chemistry Letters*, 2(18):2341–2345, 2011.

[33] FD Natterer, F Patthey, and H Brune. Quantifying residual hydrogen adsorption in low-temperature STMs. *Surface Science*, 615:80–87, 2013.

[34] Jian Zhang, Violetta Sessi, Christian Heinrich Michaelis, Iván Brihuega, Jan Honolka, Klaus Kern, Ralph Skomski, Xumin Chen, Geoffrey Rojas, and Axel Enders. Ordered layers of Co clusters on BN template layers. *Physical Review B*, 78(16):165430, 2008.

[35] Fabian Donat Natterer, François Patthey, and Harald Brune. Ring state for single transition metal atoms on boron nitride on Rh(111). *Physical Review Letters*, 109(6):066101, 2012.

[36] Roland Widmer, Daniele Passerone, Thomas Mattle, Hermann Sachdev, and Oliver Gröning. Probing the selectivity of a nanostructured surface by xenon adsorption. *Nanoscale*, 2(4):502–508, 2010.

[37] Moritz Will, Nicolae Atodiresei, Vasile Caciuc, Philipp Valerius, Charlotte Herbig, and Thomas Michely. A monolayer of hexagonal boron nitride on Ir(111) as a template for cluster superlattices. *ACS Nano*, 12(7):6871–6880, 2018.

[38] Liwei Liu, Thomas Dienel, Roland Widmer, and Oliver Gröning. Interplay between energy-level position and charging effect of manganese phthalocyanines on an atomically thin insulator. *ACS Nano*, 9(10):10125–10132, 2015.

[39] Hans Peter Koch, Robert Laskowski, Peter Blaha, and Karlheinz Schwarz. Adsorption of small gold clusters on the h-BN/Rh(111) nanomesh. *Physical Review B*, 86(15):155404, 2012.

[40] Matthew C Patterson, Bradley F Habenicht, Richard L Kurtz, Li Liu, Ye Xu, and Phillip T Sprunger. Formation and stability of dense arrays of Au nanoclusters on hexagonal boron nitride/Rh(111). *Physical Review B*, 89(20):205423, 2014.

[41] William C McKee, Matthew C Patterson, Jordan R Frick, Phillip T Sprunger, and Ye Xu. Adsorption of transition metal adatoms on h-BN/Rh(111): Implications for nanocluster self-assembly. *Catalysis Today*, 280:220–231, 2017.

[42] Caio C Silva, Jiaqi Cai, Wouter Jolie, Daniela Dombrowski, Ferdinand H Farwick zum Hagen, Antonio J Martínez-Galera, Christoph Schlueter, Tien-Lin Lee, and Carsten Busse. Lifting epitaxial graphene by intercalation of alkali metals. *The Journal of Physical Chemistry C*, 123(22):13712–13719, 2019.

[43] A Fedorov, CS Praveen, NI Verbitskiy, D Haberer, D Usachov, DV Vyalikh, A Nefedov, C Wöll, L Petaccia, S Piccinin, et al. Efficient gating of epitaxial boron nitride monolayers by substrate functionalization. *Physical Review B*, 92(12):125440, 2015.

[44] Yoshimi Horio. Low-energy electron diffraction. In *Compendium of Surface and Interface Analysis*, pages 349–353. Springer, 2018.

[45] Samir Lounis. Theory of Scanning Tunneling Microscopy. *Arxiv preprint*, page 38, 2014.

[46] C Julian Chen. *Introduction to scanning tunneling microscopy*. Oxford University Press, 2008.

[47] Roland Wiesendanger. *Scanning probe microscopy and spectroscopy: methods and applications*. Cambridge University Press, 1994.

[48] Wikimedia Commons. Mechanism of how density of states influence V-A spectra of tunnel junction, 2008.

[49] Heinrich Hertz. Ueber einen Einfluss des ultravioletten Lichtes auf die electrische Entladung. *Annalen der Physik*, 267(8):983–1000, 1887.

[50] Wilhelm Hallwachs. Ueber den Einfluss des Lichtes auf electrostatisch geladene Körper. *Annalen der Physik*, 269(2):301–312, 1888.

[51] Kai Siegbahn. ESCA: atomic, molecular and solid state structure studies by means of electron spectroscopy; pres. to the royal society of sciences of uppsala, dec. 3rd, 1965. *Nova Acta Regiae Societatis Scientiarum Upsaliensis*, 1967.

[52] Hans P Bonzel and Ch Kleint. On the history of photoemission. *Progress in Surface Science*, 49(2):107–153, 1995.

[53] Fabrizio Orlando, Rosanna Larciprete, Paolo Lacovig, Ilan Boscarato, Alessandro Baraldi, and Silvano Lizzit. Epitaxial growth of hexagonal boron nitride on Ir(111). *The Journal of Physical Chemistry C*, 116(1):157–164, 2012.

[54] E Ćavar, Rasmus Westerström, Anders Mikkelsen, Edvin Lundgren, AS Vinogradov, May Ling Ng, AB Preobrajenski, AA Zakharov, and Nils Mårtensson. A single h-BN layer on Pt(111). *Surface Science*, 602(9):1722–1726, 2008.

[55] AB Preobrajenski, AS Vinogradov, May Ling Ng, E Ćavar, Rasmus Westerström, Anders Mikkelsen, Edvin Lundgren, and Nils Mårtensson. Influence of chemical interaction at the lattice-mismatched h-BN/Rh(111) and h-BN/Pt(111) interfaces on the overlayer morphology. *Physical Review B*, 75(24):245412, 2007.

[56] Johann Coraux, Martin Engler, Carsten Busse, Dirk Wall, Niemma Buckanie, Frank-J Meyer zu Heringdorf, Raoul van Gastel, Bene Poelsema, Thomas Michely, et al. Growth of graphene on Ir(111). *New Journal of Physics*, 11(2):023006, 2009.

[57] MT Paffett, RJ Simonson, P Papin, and RT Paine. Borazine adsorption and decomposition at Pt(111) and Ru(001) surfaces. *Surface Science*, 232(3):286–296, 1990.

[58] RJ Simonson and M Trenary. An infrared study of the adsorption of borazine, $(BHNH)_3$, on the Pt(111) surface. *Journal of Electron Spectroscopy and Related Phenomena*, 54:717–728, 1990.

[59] Ivan A Vartanyants and Jörg Zegenhagen. Photoelectric scattering from an X-ray interference field. *Solid State Communications*, 113(6):299–320, 1999.

[60] M Gao, Y Pan, L Huang, H Hu, LZ Zhang, HM Guo, SX Du, and H-J Gao. Epitaxial growth and structural property of graphene on Pt(111). *Applied Physics Letters*, 98(3):033101, 2011.

[61] Christine Brülke, Timo Heepenstrick, Niklas Humberg, Ina Krieger, Moritz Sokolowski, Simon Weiß, Frank Stefan Tautz, and Serguei Soubatch. Long vertical distance bonding of the hexagonal boron nitride monolayer on the Cu(111) surface. *The Journal of Physical Chemistry C*, 121(43):23964–23973, 2017.

[62] Robert Laskowski, Peter Blaha, Thomas Gallauner, and Karlheinz Schwarz. Single-layer model of the hexagonal boron nitride nanomesh on the Rh(111) surface. *Physical Review Letters*, 98(10):106802, 2007.

[63] Andrii Goriachko, Yunbin He, Marcus Knapp, Herbert Over, Martina Corso, Thomas Brugger, Simon Berner, Juerg Osterwalder, and Thomas Greber. Self-assembly of a hexagonal boron nitride nanomesh on Ru(0001). *Langmuir*, 23(6):2928–2931, 2007.

[64] Peter Sutter, Jayeeta Lahiri, Peter Albrecht, and Eli Sutter. Chemical vapor deposition and etching of high-quality monolayer hexagonal boron nitride films. *ACS Nano*, 5(9):7303–7309, 2011.

[65] D Martoccia, T Brugger, M Björck, CM Schlepütz, SA Pauli, T Greber, BD Patterson, and PR Willmott. h-BN/Ru(0001) nanomesh: A 14-on-13 superstructure with 3.5 nm periodicity. *Surface Science*, 604(5-6):L16–L19, 2010.

[66] Walter Kohn and Lu Jeu Sham. Self-consistent equations including exchange and correlation effects. *Physical Review*, 140(4A):A1133, 1965.

[67] Wuying Huang, Chun Cheng, and Eryin Feng. Adsorption and decomposition of NH_3 on Ir(111): A density functional theory study. *Surface Science*, 616:29–35, 2013.

[68] William P Krekelberg, Jeff Greeley, and Manos Mavrikakis. Atomic and molecular adsorption on Ir(111). *The Journal of Physical Chemistry B*, 108(3):987–994, 2004.

[69] Yasuo Gamou, Masayuki Terai, Ayato Nagashima, Chuhei Oshima, et al. Atomic structural analysis of a monolayer epitaxial film of hexagonal boron nitride/Ni(111) studied by LEED intensity analysis (interfaces by various techniques). *Science reports of the Research Institutes, Tohoku University. Ser. A, Physics, chemistry and metallurgy*, 44(2):211–214, 1997.

[70] W Auwärter, TJ Kreutz, T Greber, and J Osterwalder. XPD and STM investigation of hexagonal boron nitride on Ni(111). *Surface Science*, 429(1-3):229–236, 1999.

[71] Matthias Muntwiler, Willi Auwärter, Felix Baumberger, Moritz Hoesch, Thomas Greber, and Jürg Osterwalder. Determining adsorbate structures from substrate emission X-ray photoelectron diffraction. *Surface Science*, 472(1-2):125–132, 2001.

[72] Manabu Ohtomo, Yasushi Yamauchi, Xia Sun, Alex A Kuzubov, Natalia S Mikhaleva, Pavel V Avramov, Shiro Entani, Yoshihiro Matsumoto, Hiroshi Naramoto, and Seiji Sakai. Direct observation of site-selective hydrogenation and spin-polarization in hydrogenated hexagonal boron nitride on Ni(111). *Nanoscale*, 9(6):2369–2375, 2017.

[73] Alex Kutana, Andrii Goriachko, Zhili Hu, Hermann Sachdev, Herbert Over, and Boris I Yakobson. Buckling patterns of graphene–boron nitride alloy on Ru(0001). *Advanced Materials Interfaces*, 2(18):1500322, 2015.

[74] Qiang Zhang, Yuxuan Chen, Chendong Zhang, Chi-Ruei Pan, Mei-Yin Chou, Changgan Zeng, and Chih-Kang Shih. Bandgap renormalization and work function tuning in MoSe2/hBN/Ru(0001) heterostructures. *Nature Communications*, 7(1):1–7, 2016.

[75] D Usachov, A Fedorov, O Vilkov, VK Adamchuk, LV Yashina, L Bondarenko, AA Saranin, A Grüneis, and DV Vyalikh. Experimental and computational insight into the properties of the lattice-mismatched structures: Monolayers of h-BN and graphene on Ir(111). *Physical Review B*, 86(15):155151, 2012.

[76] Yang Yang, Qiang Fu, Haobo Li, Mingming Wei, Jianping Xiao, Wei Wei, and Xinhe Bao. Creating a nanospace under an h-BN cover for adlayer growth on Nickel(111). *ACS Nano*, 9(12):11589–11598, 2015.

[77] Peter Jacobson, Tobias Herden, Matthias Muenks, Gennadii Laskin, Oleg Brovko, Valeri Stepanyuk, Markus Ternes, and Klaus Kern. Quantum engineering of spin and anisotropy in magnetic molecular junctions. *Nature Communications*, 6(1):1–6, 2015.

[78] May Ling Ng, AB Preobrajenski, AS Vinogradov, and Nils Mårtensson. Formation and temperature evolution of Au nanoparticles supported on the h-BN nanomesh. *Surface Science*, 602(6):1250–1255, 2008.

[79] Heshmat Noei, Dirk Franz, Marcus Creutzburg, Patrick Müller, Konstantin Krausert, Elin Grånäs, Robert Taube, Florian Mittendorfer, and Andreas Stierle. Monitoring the interaction of CO with graphene supported Ir clusters by vibrational spectroscopy and density functional theory calculations. *The Journal of Physical Chemistry C*, 122(8):4281–4289, 2018.

[80] David R Lide. *CRC handbook of chemistry and physics*, volume 85. CRC press, 2004.

[81] Stefan Schumacher, Tim O Wehling, Predrag Lazic, Sven Runte, Daniel F Förster, Carsten Busse, Marin Petrovic, Marko Kralj, Stefan Blügel, Nicolae Atodiresei, et al. The backside of graphene: manipulating adsorption by intercalation. *Nano Letters*, 13(11):5013–5019, 2013.

[82] Ignacio Horcas, Rs Fernández, JM Gómez-Rodriguez, J Colchero, J Gómez-Herrero, and AM Baro. WSXM: a software for scanning probe microscopy and a tool for nanotechnology. *Review of Scientific Instruments*, 78(1):013705, 2007.

[83] John W Arblaster. Crystallographic properties of iridium. *Platinum Metals Review*, 54(2):93–102, 2010.

[84] Manjeera Mantina, Adam C Chamberlin, Rosendo Valero, Christopher J Cramer, and Donald G Truhlar. Consistent van der waals radii for the whole main group. *The Journal of Physical Chemistry A*, 113(19):5806–5812, 2009.

[85] Alexander Frank Wells. *Structural inorganic chemistry*. Oxford university press, 2012.

[86] Marin Petrović, Predrag Lazić, Sven Runte, Thomas Michely, Carsten Busse, and Marko Kralj. Moiré-regulated self-assembly of cesium adatoms on epitaxial graphene. *Physical Review B*, 96(8):085428, 2017.

[87] Marco Gibertini, Achintya Singha, Vittorio Pellegrini, Marco Polini, Giovanni Vignale, Aron Pinczuk, Loren N Pfeiffer, and Ken W West. Engineering artificial graphene in a two-dimensional electron gas. *Physical Review B*, 79(24):241406, 2009.

[88] Kenjiro K Gomes, Warren Mar, Wonhee Ko, Francisco Guinea, and Hari C Manoharan. Designer dirac fermions and topological phases in molecular graphene. *Nature*, 483(7389):306–310, 2012.

[89] Marin Petrović, I Šrut Rakić, Sven Runte, Carsten Busse, JT Sadowski, Predrag Lazić, Ivo Pletikosić, Z-H Pan, Milorad Milun, Petar Pervan, et al. The mechanism of caesium intercalation of graphene. *Nature Communications*, 4(1):1–8, 2013.

[90] ND Lang and W Kohn. Theory of metal surfaces: work function. *Physical Review B*, 3(4):1215, 1971.

[91] Herbert B Michaelson. The work function of the elements and its periodicity. *Journal of Applied Physics*, 48(11):4729–4733, 1977.

Acknowledgment

This thesis brings an end to my Ph.D. study. During the last five years, I encountered some quite unexpected difficulties in life. The severe infection after liver surgery at the beginning of 2019 hospitalized me for months. During this period, the demise of Ziwen, my dearest friend, drowned me with sorrow and agony. The two movements of the research group and laboratories, as well as the Covid 19 pandemic added unforeseen obstacles to my research.

In the process of overcoming all the difficulties, I have received too many helps and assistance. At the end of this thesis, I would like to express my gratitude to a multitude of people:

- Prof. Dr. **Carsten Busse** for giving the opportunity to conduct my research in his group as well as the guidance he provides along the whole way. His expertise and professionalism sets a wonderful example for me. I am grateful for his mentorship, encouragement and witty conversations.

- Prof. Dr. **Moritz Sokolowski** for co-refereeing this thesis.

- Dr. **Wudi Wang**, Dr. **Robin Ohman**, Dr. **Xinru Li**, and **Paulus Aleksa** for the proof-reading of this thesis. Their suggestions and critiques they provided are most helpful.

- All the AG Busse members in both Münster and Siegen. It is a privilege to study and work alongside these smart and nice colleagues. The discussions with them enlightens a lot of ideas for me. Special thanks to **Paulus Aleksa** and **Dennis Rybakowski** for the technical support in the laboratory.

- Dr. **Tien-Lin Lee**, Dr. **David Duncan**, Dr. **Pardeep Kumar Thakur**, Dr. **Christoph Schlueter** and **Dave McCue** for the intellectual and technical support during our four beam-times.

- Prof. Dr. **Marko Kralj** and Dr. **Marin Petrovic**, from Institut za fiziku, Zagreb, for the intellectual and technical support during my ARPES measurements in Zagreb.

- Dr. **Nicolae Atodiresei** who provided density functional theory calculations on Cs adsorption on hBN/Ir(111).

- **Jan Stein** from the high performance cluster team in University of Siegen for the implementing the DFT code.

- All my family and friends for the love and support not only for the last five years, but also for my whole life.
- Finally, I dedicate this thesis to my dearest friend, **Ziwen Wang**, who passed away. He inspired me to be a better researcher and a better person.

List of Publications

- **Jiaqi Cai**, Wouter Jolie, Caio C Silva, Marin Petrović, Christoph Schlueter, Thomas Michely, Marko Kralj, Tien-Lin Lee, Carsten Busse. Modifying the geometric and electronic structure of hexagonal boron nitride on Ir(111) by Cs adsorption and intercalation. *Physical Review B*, 98(19):195443, 2018.

- Caio C Silva, Marcella Iannuzzi, David A Duncan, Paul TP Ryan, Katherine T Clarke, Johannes T Küchle, **Jiaqi Cai**, Wouter Jolie, Christoph Schlueter, Tien-Lin Lee, Carsten Busse. Valleys and Hills of Graphene on Ru(0001). *The Journal of Physical Chemistry C*, 122(32): 18554-18561, 2018.

- Caio C Silva, **Jiaqi Cai**, Wouter Jolie, Daniela Dombrowski, Ferdinand H Farwick zum Hagen, Antonio J Martínez-Galera, Christoph Schlueter, Tien-Lin Lee, and Carsten Busse. Lifting epitaxial graphene by intercalation of alkali metals. *The Journal of Physical Chemistry C*, 123(22):13712–13719, 2019.

Conference contributions:

- The European Workshop on Epitaxial Graphene and 2D Materials, contributed poster entitled *Determination of graphene-hBN lateral interface structure on Ir(111)*, Salamanca (2018).

- Jahrestagung der DPG und DPG-Frühjahrstagung, contributed talk entitled *Structure of pristine and hBN-embedded graphene quantum dots on Ir(111)*, Dresden (2017).

- Chinese Physical Society Fall Meeting, contributed poster entitled *Cs adsorption and intercalation on hBN/Ir(111)*, Beijing (2016).

- The European Workshop on Epitaxial Graphene and 2D Materials, contributed talk entitled *Monolayer hBN/Ir(111) functionalization by Cs adsorption and intercalation*, Bergisch Gladbach (2016).

- Jahrestagung der DPG und DPG-Frühjahrstagung, contributed poster entitled *Monolayer epitaxial hexagonal boron nitride on Ir(111) functionalization by caesium adsorption and intercalation*, Regensburg (2016).